University of Alberta

THREE-DIMENSIONAL NUMERICAL SIMULATIONS OF BUBBLY FLOWS

by

Claudia Gratiela Caia

A thesis submitted to the Faculty of Graduate Studies and Research
in partial fulfillment of the requirements for the degree of
Doctor of Philosophy

in

Applied Mathematics

Department of Mathematical and Statistical Sciences
Edmonton, Alberta
Spring, 2005

Library and Archives Canada

Published Heritage Branch

395 Wellington Street
Ottawa ON K1A 0N4
Canada

Bibliothèque et Archives Canada

Direction du Patrimoine de l'édition

395, rue Wellington
Ottawa ON K1A 0N4
Canada

0-494-08211-9

Your file *Votre référence*
ISBN:
Our file *Notre reference*
ISBN:

NOTICE:
The author has granted a non-exclusive license allowing Library and Archives Canada to reproduce, publish, archive, preserve, conserve, communicate to the public by telecommunication or on the Internet, loan, distribute and sell theses worldwide, for commercial or non-commercial purposes, in microform, paper, electronic and/or any other formats.

The author retains copyright ownership and moral rights in this thesis. Neither the thesis nor substantial extracts from it may be printed or otherwise reproduced without the author's permission.

AVIS:
L'auteur a accordé une licence non exclusive permettant à la Bibliothèque et Archives Canada de reproduire, publier, archiver, sauvegarder, conserver, transmettre au public par télécommunication ou par l'Internet, prêter, distribuer et vendre des thèses partout dans le monde, à des fins commerciales ou autres, sur support microforme, papier, électronique et/ou autres formats.

L'auteur conserve la propriété du droit d'auteur et des droits moraux qui protège cette thèse. Ni la thèse ni des extraits substantiels de celle-ci ne doivent être imprimés ou autrement reproduits sans son autorisation.

In compliance with the Canadian Privacy Act some supporting forms may have been removed from this thesis.

While these forms may be included in the document page count, their removal does not represent any loss of content from the thesis.

Conformément à la loi canadienne sur la protection de la vie privée, quelques formulaires secondaires ont été enlevés de cette thèse.

Bien que ces formulaires aient inclus dans la pagination, il n'y aura aucun contenu manquant.

Canada

University of Alberta

Library Release Form

Name of Author: Claudia Gratiela Caia

Title of Thesis: Three-dimensional numerical simulations of bubbly flows

Degree: Doctor of Philosophy

Year This Degree Granted: 2005

Permission is hereby granted to the University of Alberta Library to reproduce single copies of this thesis and to lend or sell such copies for private, scholarly, or scientific research purposes only.

The author reserves all other publication and other rights in association with the copyright in the thesis, and except as herein before provided, neither the thesis nor any substantial portion thereof may be printed or otherwise reproduced in any material form whatever without the author's prior written permission.

Department of Mathematical and Statistical Sciences
University of Alberta
Edmonton, Alberta
Canada, T6G 2G1

Date:

To Ovidiu

ABSTRACT

In this thesis, we validated a three-dimensional finite element solver for bubbly flows. The solver performs the following steps: first, the convective steps are split and resolved by the method of characteristics. Then we compute predictions of the velocity fields by projecting the pressure on the previous time level. Next, we update the pressure by combining the continuity equations for the two phases. Finally we update the velocities. The space discretization is done by the use of a stabilized version of the finite element method based on a two-level hierarchical decomposition of the domain. The method introduces two more terms to our classical Galerkin formulation: the stabilization term and the shock capturing term. The numerical scheme is tested on a series of problems. Two challenging problems that were solved using the above solver were the sedimentation problem and problem where the convection terms dominated. Detailed comparisons with different types of experiments are provided throughout the thesis. The choice of the inter-phase coefficients is a hard topic. For the one-dimensional case,we perform a nonlinear analysis of the problem and correct one of the coefficients. For the three-dimensional case, few different coefficients are tested numerically. More numerical tests are necessary to fully understand this topic. The question of simulating the transition to turbulence in 2D and 3D using a laminar model is also addressed. Positive results were obtained.

ACKNOWLEDGEMENT

I would like to thank my supervisor Dr. Peter Minev for his help and insight provided throughout the research. By facing me with such a practical engineering problem, he gave me the opportunity to acquire computing and mathematical modelling skills that are essential for being a good applied mathematician. I would also like to thank Dr. Kumar Nandakumar, whose engineering perspective helped me gain a better understanding of my research. I also wish to thank Dr. Yanping Lin, Dr. Kumar Nandakumar, Dr. Henry van Roessel, Dr. Walter Allegretto and Dr. Camilo Rindt for accepting to be members of my Ph.D. examination committee. Many thanks to Dr. Minev, Dr. Lin, Dr. Nandakumar, Dr. Ross Ethier, Dr. Abel Cadenillas and Dr. Legare for generously offering me letters of reference for different occasions and to Dr. Bryant Moodie and Dr. Wieslaw Krawcewicz for being willing to offer me letters of reference.

This work is supported by the Natural Sciences and Engineering Research Council of Canada. A part of the numerical simulations were performed on the Western Canada Research Grid, a grid-enabled computing infrastructure across BC and Alberta. Many thanks to Dr. Tony Chang for dedicating part of his time exchanging ideas related to my research topic and to Dr. Carolina Diaz-Goano for providing the original computer code designed for solving the Navier-Stokes equations.

I would especially like to thank Dr. Fraser Forbes for giving me the opportunity to work as a researcher in the area of multiobjective optimization in the Chemical Engineering Department of the University of Alberta during the last year of my Ph.D. Working for Dr. Forbes has helped me accumulate valuable knowledge and experience while allowing me to support myself and finalize my thesis.

Most of all, I would like to thank Ovidiu, my love and my best friend at the same time, for being with me during rainy days, for caring, listening and giving me hope. My world wouldn't look so beautiful if he weren't a part of it.

Table of Contents

List of Figures

1 Introduction 1

2 Literature review 5

2.1 Flow regimes in bubble columns 5

2.2 Experimental studies 7

2.3 Mathematical modelling 15

2.3.1 Direct Methods 15

2.3.2 Averaged models 22

2.3.3 Stabilization methods 29

3 Ensemble averaged model 31

3.1 Governing Equations 33

3.2 Drag force formulation 34

3.3 Added-mass force formulation 36

3.4 Lift force formulation 38

3.5 Wall force formulation 39

3.6 Pressure and shear stress terms 39

4 Numerical scheme 42

4.1 General description of the numerical scheme 42

4.2 Details about the implementation of the numerical scheme 51

5 A void fraction wave propagation problem 64

5.1 Non-linear analysis: modified bulk modulus of elasticity 64

5.2 Validation of the new expression for the bulk modulus of elasticity 73

6 Model validation **80**

6.1 Sedimentation problem 81

6.2 Circulation flow in a viscous fluid. Comparison with Durst's case 86

6.3 Coherent structures in a two-dimensional bubble column 93

6.4 Three-dimensional simulations in a cylindrical bubble column 112

7 Conclusions and Future Directions **133**

Bibliography **135**

List of Figures

2.1 Operating regimes of 3-D bubble columns 7
2.2 Operating regimes of 2-D bubble columns 7

4.1 Tetrahedral element in local coordinate system, with axes (ξ,η,ζ) 49
4.2 Tetrahedral element in local coordinate system, with axes (ξ,η,ζ) where a detailed subgriding is included 63

5.1 Velocity profile of a fixed point in time.$\Phi_0 = 0.1$(with stabilization) 65
5.2 Velocity profile of a fixed point in time.$\Phi_0 = 0.1$(no stabilization) 65
5.3 The velocity profile in the z direction at the final time.$\Phi_0 = 0.1$ (with stabilization) 66
5.4 The velocity profile in the z direction at the final time(x and y are fixed) $\Phi_0 = 0.1$ (no stabilization) 66
5.5 The void fraction profile in the z direction at the final time (x and y are fixed) $\Phi_0 = 0.1$ (with stabilization) 66
5.6 The void fraction profile in the z direction at the final time(x and y are fixed) $\Phi_0 = 0.1$ (no stabilization) 66
5.7 Velocity of a fixed point in time $\Phi_0 = 0.15$(random perturbation) (with stabilization) 67
5.8 The velocity profile of a fixed point in time $\Phi_0 = 0.175$ 67
5.9 The velocity profile in the z direction at the final time(x and y are fixed).$\Phi_0 =$ 0.175. (Case:with stabilization)(random perturbation) 67
5.10 The velocity profile in the z direction at the final time(x and y are fixed).$\Phi_0 =$ 0.15.(drag coefficient given by (3.10)) (Case:with stabilization)(random perturbation) 67
5.11 The void fraction profile in the z direction at the final time(x and y are fixed).$\Phi_0 = 0.175$.(Case:with stabilization)(random perturbation) 68

5.12 The velocity profile of a fixed point in time$\Phi_0 = 0.15$(Zuber's drag)(random perturbation) 69
5.13 The void fraction profile in the z direction at the final time$\Phi_0 = 0.15$(Zuber's drag coefficient)(with stabilization)(random perturbation) 69
5.14 The velocity profile in the z direction at the final time(x and y are fixed).$\Phi_0 =$ 0.15. (Case:with stabilization)(random perturbation) 69
5.15 The void fraction profile in the z direction at the final time(x and y are fixed).$\Phi_0 = 0.15$.(Case:with stabilization)(random perturbation) 69
5.16 The void fraction profile in the z direction at t=0,2.5,5.25,8.0 from bottom to top when the period T=2.176 (x and y are fixed) $\Phi_0 = 0.06$ 74
5.17 The void fraction profile in the z direction at t=0,1.25,2.5,4.0 from bottom to top when the period T=4.352 (x and y are fixed) $\Phi_0 = 0.06$ 74
5.18 The evolution of sinusoidal finite-amplitude concentration disturbances in time for x=0.87,2.04,3.22,4.47 from bottom to top shifted in order to be presented by Lammers *et al.* (1996) [117] on a single picture T=2.176 $\Phi_0 = 0.06$ (Reprinted with the permission of Cambridge University Press) 75
5.19 The evolution of sinusoidal finite-amplitude concentration disturbances in time for x=0.87,2.04,3.22,4.47 from bottom to top shifted in order to be presented by Lammers *et al.* (1996) [117] on a single picture T=4.352 $\lambda = 0.0$ $\Phi_0 = 0.06$ (Reprinted with the permission of Cambridge University Press) 75
5.20 The void fraction profile in the z direction at z=0.87,2.04 when the period T=2.176 $\Phi_0 = 0.06$ 78
5.21 The void fraction profile in the z direction at z=0.87,2.04 when the period T=4.352 $\Phi_0 = 0.06$ 79
5.22 The void fraction profile in the z direction at z=0.87,2.04 when the period T=4.352 $\Phi_0 = 0.06$ when the growth factor term was included in the model . . 79

6.1 The void fraction profile after 50 iterations (x axis: vertical direction, y axis: Φ) 83
6.2 The void fraction profile after 1000 iterations (t = 1) (x axis: vertical direction, y axis: Φ) 83
6.3 The void fraction profile after 1500 iterations (t = 1.5) (x axis: vertical direction, y axis: Φ) 84
6.4 The void fraction profile after 2000 (t = 2.0) iterations (x axis: vertical direction, y axis: Φ) 84

6.5 The void fraction profile prescribed by Coquel [44] "Reprinted from [44], Copyright (2005), with permission from Elsevier" 85
6.6 Axial (center-line) development of bubble velocity for two liquid heights "Reprinted from Durst *et al.* (1984) [61], Copyright (2005), with permission from Elsevier" 87
6.7 Axial (center-line) development of gas velocity for liquid height = 9.8 cm . . . 88
6.8 Profiles of the liquid axial velocity at successive axial stations (lower half of the cylinder) "Reprinted from Durst *et al.* (1984) [61], Copyright (2005), with permission from Elsevier" 89
6.9 Profiles of the liquid axial velocity at successive axial stations (upper half of the cylinder) "Reprinted from Durst *et al.* (1984) [61], Copyright (2005), with permission from Elsevier" 90
6.10 Profiles of the liquid radial velocity at successive axial stations (lower half of the column)"Reprinted from Durst *et al.* (1984) [61], Copyright (2005), with permission from Elsevier" 91
6.11 Profiles of the liquid radial velocity at successive axial stations (upper half of the column) "Reprinted from Durst *et al.* (1984) [61], Copyright (2005), with permission from Elsevier" 91
6.12 The Euclidean norm of two consecutive velocities in time 92
6.13 Liquid velocity vector field after the flow reaches the steady state. 92
6.14 Bubble images of the locally aerated flat column, with increasing aspect ratio measured experimentally. Steady state flow at H/D = 1 (a). Oscillating flow behaviour at H/D = 2 (b) and H/D =3 (c) "Reprinted from Borchers *et al.* (1999) [21], Copyright (2005), with permission from Elsevier" 97
6.15 Liquid velocity field (steady state) (H/D=1). 98
6.16 Liquid velocity field at 2 different times (H/D=2) 99
6.17 Liquid velocity field at 2 different times (H/D=3) 100
6.18 Liquid velocity field at 2 different times (H/D=2) (fine grid) 101
6.19 Gas hold-up at 2 different times (H/D=2) (fine grid) 102
6.20 Gas hold-up (H/D=2) 103
6.21 Time series of the horizontal liquid velocity to the left and of the vertical liquid velocity to the right at point C 104
6.22 Time series of horizontal liquid velocity to the left and the phase-portrait/trajectory of the liquid velocity to the right at point B 105

6.23 Time series of vertical velocities (a/b), raw data (grey curves) and FFT-filtered data (black curves). Trajectories of two-dimensional FFT-filtered velocities (c/d) "Reprinted from Borchers *et al.* (1999) [21], Copyright (2005), with permission from Elsevier" 106
6.24 Time series of vertical liquid velocity to the left and the phase-portrait/trajectory of the two-dimensional liquid velocity to the right at point C (finer grid) . . . 107
6.25 Time series of vertical liquid velocity to the left and the phase-portrait/trajectory of the two-dimensional liquid velocity to the right at point B (finer grid) . . . 107
6.26 Time series of the vertical liquid velocity at point C (different drag). 108
6.27 Time series of the vertical liquid velocity at point C (left: T=280) (right: T=80 Tdim=200s) 109
6.28 Time series of the horizontal liquid velocity at point C (left: T=280) (right: T=80 Tdim=200s) 110
6.29 Time series of the vertical liquid velocity at point B (left: T=420) (right: T=200) 110
6.30 Time series of the horizontal liquid velocity at point B (left: T=420) and the phase-portrait/trajectory to the right 111
6.31 Time series of the vertical liquid velocity at point C 111
6.32 Snapshot of gas hold-up profile: $\Phi_v = 1$ l/min, $r_s = 2$ cm 114
6.33 Liquid velocity field (x=D/2: vertical central plane cross-section): $\Phi_v = 1$ l/min, $r_s = 2$ cm 115
6.34 Snapshot of gas hold-up profile: $\Phi_v = 2$ l/min, $r_s = 2$ cm 116
6.35 Snapshot of gas hold-up profile (different angle): $\Phi_v = 2$ l/min, $r_s = 2$ cm . . . 117
6.36 Snapshot of gas hold-up profile (slice x = D/2): $\Phi_v = 2$ l/min, $r_s = 2$ cm . . . 118
6.37 Snapshot of gas hold-up profile (slice y = D/2): $\Phi_v = 2$ l/min, $r_s = 2$ cm . . . 119
6.38 Liquid velocity field (x=D/2: vertical central plane cross-section): $\Phi_v = 2$ l/min, $r_s = 2$ cm 120
6.39 Liquid velocity field (y=D/2: vertical central plane cross-section): $\Phi_v = 2$ l/min, $r_s = 2$ cm 121
6.40 Liquid velocity field (XZ plane: y=0.25) $\Phi_v = 2$ l/min, $r_s = 2$ cm 122
6.41 Liquid velocity field (XZ plane: y=0.75) $\Phi_v = 2$ l/min, $r_s = 2$ cm 123
6.42 Snapshot of gas hold-up profile: $\Phi_v = 4$ l/min, $r_s = 4$ cm 124
6.43 Snapshot of gas hold-up profile (different angle): $\Phi_v = 4$ l/min, $r_s = 4$ cm . . . 125
6.44 Snapshot of gas hold-up profile (slice x = D/2): $\Phi_v = 4$ l/min, $r_s = 4$ cm . . . 126

6.45 Snapshot of gas hold-up profile (slice y = D/2): $\Phi_v = 4$ l/min, $r_s = 4$ cm . . . 127
6.46 Liquid velocity field (x=D/2: vertical central plane cross-section): $\Phi_v = 4$ l/min, $r_s = 4$ cm . . . 128
6.47 Liquid velocity field (YZ plane: x=0.75) $\Phi_v = 4$ l/min, $r_s = 4$ cm . . . 129
6.48 Liquid velocity field (y=D/2: vertical central plane cross-section): $\Phi_v = 4$ l/min, $r_s = 4$ cm . . . 130
6.49 Liquid velocity field (XZ plane: y=0.35) $\Phi_v = 4$ l/min, $r_s = 4$ cm . . . 131
6.50 Liquid velocity field (XZ plane: y=0.75) $\Phi_v = 4$ l/min, $r_s = 4$ cm . . . 132

Chapter 1

Introduction

Multiphase flows occur in many engineering and natural systems: boiling systems, such as nuclear power plants and distillation equipment; liquid fuel combustion processes; chemical and food processing; lubrication systems; biological systems; gas and oil extraction and transport etc.

The starting point for the derivation of multiphase flow models is usually the system of the Navier-Stokes equations, which is the mathematical model of a single phase flow and whose justification is very solid. The most important feature of multiphase flow systems is the presence of interfaces separating the phases and across which the fluid properties are essentially discontinuous. The natural approach towards modelling two-phase flows would then be the solving of the system of Navier-Stokes equations for each phase. The coupling between the phases would be considered through the boundary conditions. This approach is known in the literature as the direct approach (see Esmaeeli and Tryggvason [66], Bunner and Tryggvason [26]). The advantage of this method is its high accuracy. However, at present, the direct approach has been successfully used only for a relatively low number of particles/bubbles dispersed in the liquid phase. When the dispersed phase represents a high percentage of the whole mixture, to track the trajectories of thousands of particles that in addition start interacting results in a multi-boundary problem with positions of the interphases being unknown. The resolution required to solve the local flow field equations accurately makes the task virtually impossible, computationally. Because of this major drawback, a different approach has been adopted. The finer details of the flow are suppressed and the macroscopic features are retained through averaging. There exist different types of averaging: time, space or statistical, all yielding a set of differential equations for which the number of unknowns is higher than the number of equations. The interpenetrating continuum assumption is the main hypothesis in

all these models. This means that throughout the domain both phases coexist. Therefore, at each discrete point in the computational domain different quantities must be computed: the velocities of both phases, their pressures and the volume fractions equal to the fractions of the volume occupied by those phases locally. Various mathematical models have been derived, some with just one momentum equation for the mixture, others with a momentum equation for each phase. To be able to close the system of equations yielded by averaging, it is necessary to add the so-called 'closure laws' that model the "inter-phase transfer" terms, in other words the terms that account for the transfer of mass, momentum or energy between the phases. These closure laws are highly phenomenological in nature, i.e. they depend on the problem that is modelled. For instance, in the case of fluidized beds, the neglect of the added-mass force is a valid assumption; however, in the case of bubbly flows this term plays an essential role because it is proportional to the liquid density that is much higher than the gas density; in a pressurized system such as the primary circuit of a nuclear reactor, both the liquid and vapor phases will flow at comparable velocities, so it can be assumed with a good approximation that they are equal; however, through a static column the bubbles will rise at a much higher velocity than the liquid; in a disperse flow, when bubbles are relatively small and of spherical shape and not much bubble-bubble interaction is present the drag force will be totally different than for the case of a bubble-driven flow when a high volume fraction is occupied by the gas phase, bubbles are highly deformable and bubble coalescence and breakup have to be accounted for.

Most of the averaged models existing in the literature are one-dimensional. Park *et al.* [139], however, derived a three-dimensional model. It can be easily seen that additional terms are present in a three-dimensional model. The modelling is further complicated by the range of different flow regimes. The different constitutive equations are always formulated with specific flow regimes in mind. In order to proceed any further, we must have a criteria for analyzing the different correlations of the inter-phase transfer terms.

Minev *et al.* [130] compared different multiphase flow models relevant to bubbly flows available in the literature by performing one-dimensional linear and nonlinear analysis. The first observation was that all the equal pressure models are not realistic. Therefore, explicitly or implicitly, which means by adding a term that contains the void fraction gradient, we have to account for the different pressures of the two phases. The linear analysis of the various possible models showed that only two models out of the models considered in their study, namely those formulated by Biesheuvel *et al.* [18] and Stuhmiller [176] provided reasonable neutral stability curves and critical values for the void fraction. However, the nonlinear analysis of the two models produces a nonlinear equation whose solution is unstable in the long run. There is

experimental evidence for the existence of stable void fraction waves. This study revealed that neither of the multiphase flow models considered produces realistic results. In one of the next chapters we show how we can fix this problem, at least for the case of an unidirectional flow. Of course, this theoretical study is one-dimensional and any extension to the three-dimensional case must be validated by means of extensive numerical simulations.

Even though most of the existing models were derived under the assumption of small departure from uniformity and for void fraction and gas velocities characteristic for the laminar regime, if the transition to turbulence is to be captured, then special care must be taken into account since the turbulence production is the result of continuous instability. Thus, stabilization algorithms must be added to the numerical scheme. Of course, for Reynolds number corresponding to the turbulent regime, no numerically stabilized scheme can accurately compensate for the instability inherent to turbulence. In that case, the molecular diffusive effects become small compared to the turbulent mixing and this phenomenon requires extra diffusion into the equations, which introduces additional unknown turbulent variables and new transport equations for them.

The stabilization algorithm implemented in our code is based on a hierarchical two-level decomposition of the approximation space as proposed by Guermond (1999) [79]. This scheme suggests two more terms to be added to the classical Galerkin formulation: one stabilization term and one shock-capturing term.

In the next chapters after a critical review of the literature (see chapter 2), we introduce the mathematical model (chapter 3) and the numerical scheme (chapter 4). In chapter 5 we perform a linear analysis of the system of partial differential equations used as starting point and we modify the expression of the bulk modulus of elasticity so that the experimentally measured effective diffusivity to be taken into consideration (see Lammers and Biesheuvel [118]). In chapter 6, we validate the numerical scheme using one benchmark problem, the sedimentation of two phases with similar but different densities, a wave propagation problem in a cylinder and a circulation flow in a viscous fluid, offering comparison between our numerically computed velocity and void fraction profiles at different measuring stations in the cylinder and the experimental and numerical profiles obtained by other authors. In the second part of chapter 6 we would like to answer the question: is it possible, with the use of a laminar model to capture the transient behavior of the flow towards turbulence, which is a vortical flow regime in 2D and the spiral-flow regime in 3D? The vortical flow regime in 2D is characterized by the appearance of many smaller vortices that persist for a certain transitional period of time before the flow becomes steady and only two big circulation cells are formed. The understanding of

the nature of these dynamic "coherent structures" is very important since they are probably responsible for a large fraction of the transport of the conserved properties such as species, mass, momentum and energy and they are an important component of every turbulent flow. For the 2D case we compare our results with some experimental data. In the last part of chapter 6 we perform some simulations in a cylindrical three-dimensional bubble column. There are very few experimental papers that treat this case and they predict a vortical-spiral flow regime to be the three-dimensional equivalent of the vortical flow regime noticed in the two-dimensional case. The transition of the flow regimes and the flow structure in the vortical-spiral flow region are found by Chen *et al.*[36] to be analogous to the Taylor stability postulation and its resulted turbulent vortices structure for the flow between two concentric rotating cylinders.

Chapter 2

Literature review

2.1 Flow regimes in bubble columns

The main factor that characterizes the flow regime in a bubble column is the superficial gas velocity. In a two-dimensional bubble column (the third-dimension is negligible) the dispersed bubble flow regime exists up to a superficial gas velocity of 9 mm -1 cm/s in an air-water system according to the measurements of T.-J. Lin *et al.* [122]. If the liquid is more viscous, this threshold will be different. For a three-dimensional cylindrical bubble column Wallis [195] states that laminar flow occurs for superficial gas velocities lower than 4 cm/s. Note that the observed transient velocity in the 2D column is lower than that of a 3D column. As J.-W. Tzeng *et al.* [189] remarks, this is probably due to the less degree of freedom in the bubble movement in a 2D column.

The homogeneous flow regime is characterized by small bubbles (diameter is in the range 1-10 mm) of uniform bubble size with a relatively uniform distribution in the column and a rather flat liquid velocity profile. The diameter of the column doesn't play an essential role in this case, but the sparger design does. If the gas is injected through the middle of the column only, circulation can occur. However, in general, the bubbles move upward in bubble streams but no coalescence or clustering occur.

If the superficial gas velocity is increased then the flow enters a transition regime for columns with diameters larger than 20 cm. If the experiment is performed at laboratory scale where small-diameter columns are used (D < 15 cm) then the flow may very quickly enter the slug flow regime due to the intensive coalescence and break-up of the bubbles that gives rise to large, slug shape bubbles.

L.-S. Fan and his co-workers have brought remarkable contributions in understanding the

way the 2D and 3D columns work. For the first time, they showed that before the column reaches the turbulent regime, a coalesced bubble regime characterized by two flow conditions (4 and 3-region flow) with coherent flow structures exists. (T.-J. Lin *et al.* [121], R.C. Chen *et al.* [36]).

T.-J. Lin *et al.* [121] performed 2D experiments. They claim that the 4-region flow condition exists for gas velocities between 1 and 3 cm/s. The region close to the sidewalls is characterized by a downflow liquid movement with a scarce distribution of the gas phase. When the superficial gas velocity is about 1 cm/s the bubbles start to migrate from the near wall region and generate small vortices. This represents the vortical flow region. If the superficial velocity is further increased, the bubbles start coalescing, forming the fast bubble flow region that moves in a wave-like manner. The core of the cylinder represents the central plume region. The bubbles are small is size and they move upward a laminar way. If the column diameter is less than 20 cm the central plume region and the fast bubble flow region collide. The result is a 3-region flow. The same phenomenon happens in larger columns if the superficial gas velocity is around 3 cm/s. The new central bubble stream moves in a wave-like manner. A similar behavior was described by Tzeng *et al.* [188]. R.C. Chen *et al.* [36] performed similar studies in a 3D column and the equivalent three flow regimes were identified: the dispersed bubble flow, the vortical-spiral flow and the turbulent flow. The vortical-spiral flow regime is characterized by superficial gas velocities in the range 2.1 - 4.2 cm/s. In this regime, the liquid is carried up by the central stream that spirals up in the core region of the cylinder and falls in a vortical and spiral way in the region between the central bubble stream and the column wall.

T.-J. Lin *et al.* (1996) (see Fig. 2.2 from [121], Copyright © 2005 and American Institute of Chemical Engineers; Reprinted with the permission of John Wiley Sons, Inc.) provide a chart for the operating regimes of 2-D bubble columns that is similar to the classical regime classification of Shah *et al.* (1982)(see Fig. 2.1 from [165], Copyright © 2005 and American Institute of Chemical Engineers; Reprinted with the permission of John Wiley Sons, Inc.) for 3-D bubble columns.

The turbulent flow regime is characterized by superficial gas velocities larger than 5 cm/s. The gas volume fraction is usually above 30 %. The distributor plate plays no roll in the flow behavior. Variations of the bubble diameters are big and the circulation is vigorous.

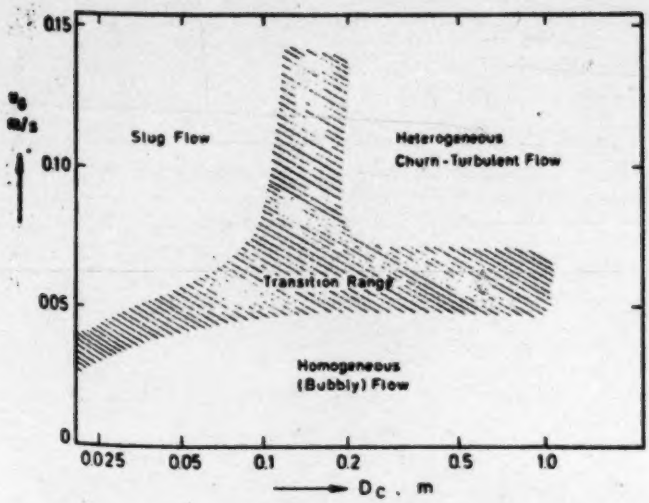

Figure 2.1: Operating regimes of 3-D bubble columns

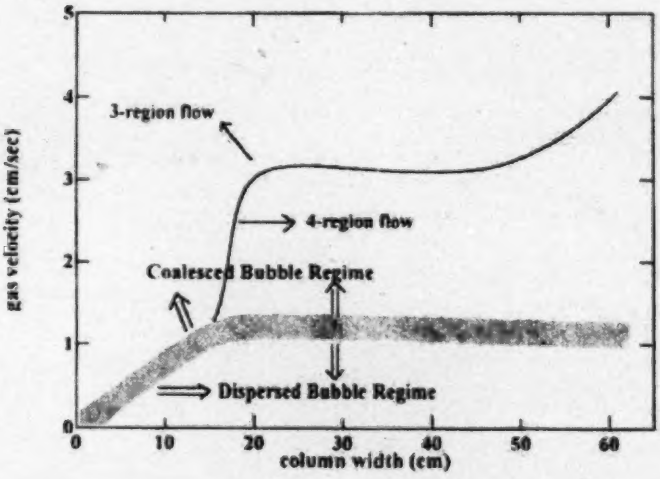

Figure 2.2: Operating regimes of 2-D bubble columns

2.2 Experimental studies

Computational fluid dynamics (CFD) became increasingly popular due to the fast development of the computers. Lots of bubble columns and bubble column reactors have been designed and numerically simulated. However, since we have only tried to simulate the flow development

in a vertical bubble column in which the bubbles are injected through the bottom and escape from it at the upper surface, we restrict our literature review to this case.

In the last fifty years many papers and commercial software appeared. In order to test their performance, comparison with experimental data is essential. Even though there are experimental data available, few authors present a very detailed description, which makes the comparison difficult. For instance, the type of sparger plays an essential role in creating the flow structure. Most of the time, the gas is supplied in such a way to create small bubbles and distribute them uniformly at the inlet to maximize the mass transfer. Zehner *et al.* [208] classifies them into "static" and "dynamic" gas spargers. Among the static spargers, they mention the dip tube, the perforated plates, the perforated ring spargers and the porous plates. The dynamic spargers (the jet nozzle, the jet nozzle with momentum-transfer tube, the ejector jet nozzle, the ejector, the Venture tube and the momentum-transfer tubes) use the power of a liquid jet to disperse gas in a zone of high energy-dissipation rate. More details on this topic can be found in Zehner *et al.* [208] and their references. Most of the static spargers produce a uniform aeration, while the dynamic spargers produce a partial, central aeration of the inlet. That is the reason some authors treat the case of constant volume fraction at the inlet while others consider a step function at the inlet. Another important factor when trying to compare the simulations with the experiments is the bubble size, that is directly linked to the drag force. In the homogeneous regime, the bubble diameter is within the range 1-8 mm. For the heterogeneous flow regime, characterized by high breakup and coalescence of the bubbles, no measurement method can accurately determine the bubble size. Moreover, most of the Eulerian models do not account for this phenomenon. Instead, they compute the so-called Sauter diameter that is a mean bubble diameter and they incorporate this into their drag coefficient.

The experimental techniques advanced over time drastically. At the beginning Hills [86] and other authors used the Pitot tube. Later on, the experiments were performed by means of (HFA) (hot-film anemometry) and (LDA) (laser-Droppler anemometry). The next type of experiments used (CARPT) (computer automated radioactive particle tracking) and (CT) (computer tomography) methods. All these methods were good, but not advanced enough to capture the instantaneous flow fields. All the above techniques and other tomographic techniques were too slow to capture the real-time image of highly fluctuating flows, so they represent time-averaged measurements. The breakthrough came with (PIV)(particle image velocimetry) technique and (ECT) (electrical capacitance tomography). (ECT) systems can capture up to 100 image frames per second, comparing to the X-ray computer tomography

(CT) of only one image for 2 s.

The remaining part of this sub-chapter will analyze the most important experimental papers, starting from the classical Pitot tube experimental paper up to papers based on (PIV) and (ECT) techniques.

One representative example of the early experimental work on quantitative measurements of axial velocity distribution was that of Hills [86]. The measurements of the time-averaged axial velocity profiles were conducted using a point Pitot tube. He measured both the mean and the fluctuating velocities of the liquid circulation. A conductivity method was incorporated fore measuring gas holdup distribution.

When testing liquid velocities predicted by theory against experimental data, specific and detailed information about the system of study is needed in order to completely define the hydrodynamics. It is for this reason that the data of Hills [86] are often chosen as a benchmark to test liquid velocity predicted profiles. Hills described the sparger specifics, water conditions and the radial voidage profile, omitted in many other papers. His column had an internal diameter of 138 mm and a height of 1370 mm. Three different sieve plates were used as the gas distributors and three different results were obtained. The most used test case was for the second arrangement, which consisted in 61 holes with a diameter of 0.4 mm, one central and the rest uniformly spaced on three circles. The gas flow rate at the distributor was varied between 19 mm/s up to 169 mm/s. Circulation up one side and down the other, noted in two-dimensional columns was not stable in their column. They present the results of the hold-up and frequency measurements as function of the radial position with the superficial gas velocity as a parameter. Local voidage and liquid velocity were measured at a position 600 mm above the sieve plate. The profiles for plates B are moderately flat at gas rates below 30 mm/s, but at higher gas rates there is an increasingly sharp central maximum in both hold-up and frequency. The transitional gas rate, of about 30 mm/s, corresponds to the point where the experimental mean hold-up breaks away from the curve for uniform bubbling. A very long sampling time results were obtained by averaging two successive periods of 500 seconds. Even though this paper presents very detailed measurements of both void fraction and liquid velocity, it only gives long-time averaged results. No instantaneous profiles are measured. The cases presented here are either in the homogeneous regime (u_{0G} = 19mm/s) or in the churn regime ($u_{0G} \geq$ 38mm/s) with the focus on the churn regime. The transition regime is not well captured. Also, the diameter of his column is much smaller than the diameter of any industrial column. He only has one measuring height for his columns.

Because of the detailed information presented by Hills [86] many authors tried to validate

their models by choosing his sets of data as comparison. Among them there are: L.F. Burns and R.G.Rice [28], H. Liu *et al.* [123], R.G. Rice and N.W. Geary [152], N.W. Geary and R.G. Rice [73], S.B. Kumar *et al.* [113].

Hills [86] used tap water in his experiments. Rietema [156] and Rietema *et al.* [157] provided high-viscosity data. They even estimated the size of the bubbles in their experiments. R.G. Rice and N.W. Geary [152] validated their model using this set of data, too.

After Hills's remarkable contribution, many other experimental papers were published that were also able to reproduce only the overall averaged flow field that consists in two gross circulation cells or the so-called "golf-stream" pattern. They were based either on hot-film anemometry (HFA) (Walter and Blanch *et al.* [197] , Franz *et al.* [71], Menzel *et al.* [128], Torvik and Svendsen *et al.* [186], Grienberger and Hofmann [77]) or on laser-Droppler anemometry (LDA) (Becker *et al.* (1994) [16], Franz *et al.* (1984) [71], Iguchi *et al.* [94], Groen *et al.* [78], Mudde *et al.* [132], Deshpande and Joshi *et al.* [51]).

Since some of these papers were used by many authors for validation of their numerical schemes even though they only reproduce the time/space average behavior of a bubble column, we shall present the most famous experiments.

One set of large-column experiments has been provided by Kojima *et al.* [109]. They used three different superficial velocities at the inlet: 2.2 cm/s, 3.6 cm/s and 4.4 cm/s. The diameter of his column was 5.5 m. N.G. Geary and R.G. Rice [73] also used their experiments for validation.

L.F. Burns [27] and L.F.Burns and R.G. Rice [28] used Pavlov tube and (HFA)/steel-clad probe for the liquid phase and conductance probe technique for the voidage measurement. They performed experiments under conditions of lowered surface tension, using a small amount of surfactant, and proved that uniform circulation can exist even in the bubbly-flow regime. The advantage of using surfactant is that it transforms the bubble into a more spherical shape by reducing its size and making the bubble more rigid. This reduces the risk of coalescence. The column used in their experiments has a 13.97 cm diameter. They used three different gas superficial velocities: 1.25, 1.74 and 2.25 cm/s.

Yao *et al.* [205] also used (HFA) in their experiments. Their column inner diameter is 0.29 m and the smallest superficial gas velocity used was 0.04 m/s. Nottenkamper *et al.* [136] measured the liquid velocity by a fly-wheel anemometer and the gas hold-up by an optical probe. They used a bubble column of 0.45 m diameter and $u_{0G} \geq 0.053$ m/s.

Menzel *et al.* [128] (HFA) performed experiments in bubble columns and airlift loop reactors in both homogeneous and heterogeneous flow regime. They made three different types of

experiments using water (D = 150 mm, H = 2575 mm), 0.22 % aqueous propanol solution (non-coalescing system) (D = 600 mm, H = 3455 mm) and 80 wt% glycerol solution (D = 600 mm, H = 5440 mm) as the liquid phase. Even though they don't specify the type of sparger they used or at least the type of aeration (partial or total aeration), their totally flat profiles obtained in the homogeneous regime (u_{0G} =1.2 and 2.4 cm/s) might be an indication that they used total aeration. The profile with water as the liquid phase and superficial gas velocity of 4.8 cm/s lies in the transition regime. They obtained parabolic profiles in the heterogeneous regime. In addition to the radial profiles of the local gas holdup and mean axial liquid velocity they also show the radial profiles of turbulent kinematic viscosity, ν_t. Also an empirical correlation for the prediction of the turbulence intensities has been developed. Svendsen *et al.* [182] (five-point electro-conductivity probe) used this set of experiments to validate their model. However, they concluded that a drag that takes into account the bubble coalescence should be used if improved agreement is to be achieved.

Yu and Kim [207] (optical fibres probes) performed experiments in a 0.254 m inner diameter and 2.5 m high bubble column. They analyzed cocurrent gas-liquid flow. The liquid were supplied at the inlet but the gas was supplied through 8 6 mm inner diameter horizontal perforated pipes (78 holes 1 mm diameter) evenly positioned at different heights in the column. They can be seen as mass source terms. Their sieve plate had 645 evenly spaced 3 mm in diameter holes for water. The measuring point was 0.475 m above the distributor. They performed many experiments where the gas superficial velocity range was 1-14 cm/s and the liquid superficial velocity range was 0-10 cm/s. The flow regime changed from bubbly to churn turbulent in the gas velocity range 4-6 cm/s when appreciable bubble coalescence has been observed from the variation in the bubble chord length distribution. They obtained flatter radial profiles for the gas phase hold up than those obtained by Ueyama and Miyauchi [190], for instance, because the wall effects were less pronounced in their larger column and the bubbles formed from the present distributor were smaller than those generated from a single nozzle. They also noticed that average gas void fraction increases with increasing gas velocity but it decreases slightly with an increase in liquid velocity because bubbles are broken up by small-scale liquid eddies that provide more intense turbulence in the column (Walter and Blanch, [197]).

Grienberger and Hofmann [77] (HFA) performed experiments in 0.29 m diameter and 4.5 m height bubble column using deionized water as the liquid phase. No sparger specification was made. The measuring station was 3.5 m above the inlet.They performed two experiments using a superficial liquid velocity of 1 cm/s and two gas superficial velocities of 2 cm/s and 8

cm/s.

Even though all the above papers were able to capture the long time behavior of bubble columns, at both lab scale and industrial scale, the visual observations of the flow in bubble columns indicated the existence of multiple circulation cells in the axial direction. The first researchers that actually built a mathematical model able to predict multiple circulation cells were Joshi and Sharma [106]. The model is far from being realistic, in the sense that assumes that the columns are symmetric with respect to the central axis of the cylinder and it assigns the same clockwise rotation to cells above each other that is physically impossible, but it is a big step forward.

J.J.J. Chen *et al.* [34] performed experiments in two different 2-D columns. The first column had a working section of 760 mm × 50 mm and 1.5 m in height with a gas distributor made from a 45 mm diameter tube. The second column was 175 mm × 15 mm and 1.8 m high. It had a distribution chamber with a wire gauze acting as a bubbler. The gas superficial velocity was 35 mm/s. Many experiments had been performed by varying the height of the liquid into the columns. When $H/D < 1$, the pattern was the so-called "gulf-stream" or vortex pair. When $H/D > 1$ the pattern was that of staggered vortices and this result is consistent with the well known Karman vortex street. Von Karman showed that two infinite parallel rows of vortices cannot be stable if placed according to the multiple circulation cell suggested by Joshi and Sharma [106].

Franz *et al.* [71] used both (HFA) and (LDA) to measure local time profiles of fluid velocities in axial, radial and tangential direction as well as turbulence intensities. Even though these methods are not advanced enough to capture the instantaneous velocities, they are among the first authors that recognized visually the so-called phenomena of the bubble hose, defined as a zone of high bubble number density moving helically in a bubble column. They show that the assumption of axisymmetric flow and regular flow structures, like torus vortices, that are present in many of models existent in the literature is not valid. Based on their measurements, the flow should be divided into three zones: swarm/homogeneous turbulence in the center part of the column, an almost bubble-free zone near the walls and between these tow zones, a vortex street zone with high velocity gradient where free anisotropic turbulence occurs.

Durst *et al.*[61] (LDA) measured an axisymmetric, recirculating flow induced by a bubble steam injected through a central nozzle distributer. The diameter of the column was 100 mm and two height to diameter ratios of 0.98, 2.78 respectively, were used. They used caster oil as the liquid phase and the liquid velocities obtained corresponded to a creeping flow. Since this case was axisymmetric (we saw that this is not necessary the case in other simulations) Celik

and Wang [32] developed a simplified model and used these experiments for validation.

An essentially 2D column was used by S. Becker *et al.* [16] (LDA). Their team also tried to model the observed flow using a dynamic model. The results are presented in Part I of the same paper by A.Sokolichin and G.Eigenberger [170]. They considered three different situations: a partially aerated bubble column, a fully aerated bubble column and an airlift loop reactor. We are only interested in the first two cases. The column had a rectangular cross-section (500 mm × 80 mm) and a 2000 mm height. The gas was injected through one to five individually regulated frets: each of 40 μm pores and 40 mm disc diameter. For the uniformly aerated bubble column the simulations show that above a minimum value of the superficial gas velocity of about 2 cm/s an unsteady flow structure develops where a sequence of vortices is created near the gas distributor. They are not stationary but they move upwards at alternating sides of the wall. Long time averaged results present the classical result of two big circulation cells.

Fischer *et al.* [70] (LDA) performed experiments in a cylinder of 0.1 m diameter and 0.88 m height using an ion-exchanged water/air system and two different types of perforated plates: a partial aerated and a fully aerated disperser. Their finding were similar to those of Franz*et al.* [71]. This transitional regime from laminar to turbulence can be seen as a generalization of the conclusions of Tzeng *et al.* [189] who performed experiments in a 2D column.

The development of more advanced instrumentation techniques made possible the capturing of local and global flow patterns including time averaged axial and radial velocity profiles, local void fraction profiles and even of the turbulent parameters. Two very famous techniques are the computer automated radioactive particle tracking (CARPT) (Devanathan *et al.* [53], Yang *et al.* [204]) and the computer tomography (CT) (Kumar *et al.* [112, 113, 114]).

Kumar *et al.* [112] ((CARPT) and (CT)) were interested in prescribing the mixing length scale necessary for the scale-up of liquid hydrodynamics in bubble column. Since they are only interested in the time/space-averaged profiles they performed experiments in five different column sizes. The ratio of height to diameter was always greater than five. The superficial velocity was ranged from 0.05 to 0.12 m/s. They used five perforated plates for which the open area varied between 0.05 and 0.1 % of the total plate area. They developed a one-dimensional mathematical model and they compared it with their set of experimental data and also with Hills [86], Yao *et al.* [205] and Nottenkamper *et al.* [136]. This attempt to unify a wide range of data is remarkable. However, their goal and our intensions are quite different.

Devanathan *et al.* [53] used (CARPT) that is a Lagrangian-tracking method. Their column has a 0.292 m inner diameter and 0.584 m height. The superficial air velocity was 0.105

m/s. They only present the time-averaged results, i.e. the classical liquid circulation or gulf streaming. Therefore, this paper is useful only if we are interested in the steady-state behavior of the flow.

The recent development of measuring techniques is impressive. After many years, there are now experimental techniques capable of measuring the instantaneous full-field profiles. Among them we shall mention the non-intrusive particle image velocimetry (PIV) and the electrical capacitance tomography (ECT) methods. (PIV) is now widely used (R.C. Chen *et al.* [36], Chen and Fan [35], Reese *et al.* [148], Reese and Fan [149], Mudde *et al.* [132], Lin *et al.* [122]. (ECT) was adopted by Warsito and Fan [202], Reinecke and Mewes [150], Dyakowski *et al.* [62].

The non-intrusive PIV technique has the ability to quantify the instantaneous flow field, as well as the time-averaged flow patterns in selected planes of the column. It can also assess the coupling effects of the flow field that may be lost when using a point measurement technique.

The same vortical-spiral flow regime reported by Franz *et al.* [71] and Fischer *et al.* [70] in three-dimensional columns was obtained experimentally by R.C. Chen *et al.* [36] (PIV). This method seems so far among the most suitable for capturing instantaneous full-field results. We think their result is a 3D extension of the staggered vortices obtained by J.J.J. Chen *et al.* [34] in 2D columns. Their column has a 10.2 inner diameter and 1.2 m height. The superficial gas velocity is varied over a wide range to capture the vortical-spiral flow regime. The authors assume that this flow regime is analogous to the turbulent Taylor vortices structure.

Mudde *et al.* [132] (PIV) used a two-dimensional column of 48.2 cm in width, 160 cm in height and 1.27 cm in depth. Two movable partitions allow the width to be varied from 11.2 cm to the full width. This paper is remarkable in the sense that the authors came up not only with instantaneous gas and liquid velocity profiles, Reynolds stress profiles and averaged profiles but also they perform a rigorous time-series analysis of the flow field that made possible to separate the contribution of the vortical structures from the high-frequency fluctuations in the normal stresses. The eddy viscosity is estimated around 5×10^{-4} m^2/s. Pan *et al.* [138] chose these experiments for validation of their numerical scheme.

Dudukovic and Fan's teams joined their efforts and came up with a comparative study between (CARPT), (CT) and (PIV) in J. Chen et al. [33]. They used the same configuration of the bubble column and the same operating conditions for all three independent experiments. With all these efforts, they still obtained quite different normal stresses and axial velocities. The conclusion of their paper favored the PIV method. However, the CARPT technique works also well if we are more interested in the ensemble averaged quantities and the long-time

behavior.

Measurement of real-time flow structures in a bubble column were done using (ECT) by Warsito and Fan [202]. Despite its incredible high speed (100 image frames per second), one of its critical problems is the relatively low accuracy of the reconstructed image using available reconstruction algorithm (see Huang et al.[90], Xie et al.[203]). The authors of this paper overcame this drawback by using a reconstruction algorithm based on a modified Hopfield dynamic neural network optimization technique.

Rensen and Roig [151] performed experiments (optical fiber probes and video camera measurements) of two-dimensional bubble plumes confined in a tank. The study revealed that the bubble plume presented an unsteady oscillatory movement no matter what the gas flow rate. At low gas flow rates, the movement of the plume was periodical and progressive. The confinement determined the frequency of the oscillation. At higher flow rates, despite the strong inter-phase interaction, a dominant frequency remains that characterizes the motion of the plume.

2.3 Mathematical modelling

There exist two approaches in the literature when it comes to the mathematical modelling of multiphase flows: the direct approach and the averaged approach.

In the direct approach the local flow variables (velocity fields, densities, pressures) are computed. No simplifying assumptions are made. These methods yield accurate results but are only suitable when dealing with a small amount of bubbles. When many bubbles must be modelled (like in real experiments), simplifying assumptions, which result in loss of information, are usually done. Averaged instead of local quantities are computed (averaged velocity fields, densities, pressures, volume fractions). The "inter-penetrating continuum" hypothesis is the main assumption in the averaged models, which means that in all the grid points of our discrete domain both phases coexists and different continuity and momentum equations for each phase, coupled through interphase transfer terms, must be solved.

2.3.1 Direct Methods

Depending on how the numerical grid is chosen, fixed, moving with the gas phase or a combination of the two, the direct methods can be categorized as: Eulerian, Lagrangian or Eulerian-Lagrangian.

Lagrangian approach

The Lagrangian approach is mainly used in free surface problems. Bubbles are classical examples of hydrodynamic objects with free surfaces whose transient behavior and stability are of interest in many fields: chemical technology, biotechnology, capillarity etc. However, this approach has reduce applicability when many bubbles are involved. It has only been used to model the case of one or two bubbles moving through the liquid.

A general finite element method scheme based on the Lagrangian approach is considered by Connor and Brebbia [43]. In the Lagrangian approach the finite elements move with the liquid and after a time period they naturally become too distorted or stretched. Because of this, a mesh redefinition must be done from time to time. Bach and Villadsen [8] uses this approach to simulate a wave motion in a vertical film.

Shopov *et al.* [167] designed a numerical method based on the Lagrangian approach to model the transient behavior of deformable fluid particles-bubbles, drops and multiple drops. Among the numerical test cases considered are the motion of a bubble due to buoyancy in an unbounded viscous liquid at relatively high Reynolds and Eötvös numbers, interaction of a bubble with a rigid wall and motion of two bubbles towards a rigid wall.

Idelsohn *et al.* [93] presented a particle method for the solution of the incompressible inviscid fluid flow equation using a Lagrangian formulation. Instead of permanently updating the positions of the points, like in the finite element and finite difference based methods, they model the moving interfaces with the help of the meshless methods. However, the only test case considered is the collapse of a water column. They haven't try to apply their method to bubbly flows.

Eulerian-Lagrangian approach

The idea behind any Eulerian-Lagrangian method is the same: while the computational domain is fixed, the bubbles/particles' trajectories are followed in time. Afterwards, the new locations of the particles are projected back onto the fixed grid and using an interpolation procedure the unknowns are advanced to the new time-level.

The numerical treatment of convection-diffusion partial differential equations, where the convection dominates, presents serious difficulties. There are many numerical methods that deal with this method but most of them are Eulerian in nature. The classical Eulerian-Lagrangian methods are the characteristic methods (see Douglas and Russell [55], Pironneau [144], Varoglu and Finn [194]). Traditional forward tracking or moving mesh methods advance the grids following the characteristics and greatly reduce temporal errors. However, they often

severely distort the evolving grids and greatly complicate the solution procedures. The modified method of characteristics (MMOC) (Douglas and Russell [55]) tracks the characteristics backward from a fixed grid at the current time step and, hence, avoids the grid distortion problems present in forward tracking methods. Even though the (MMOC) symmetrizes and stabilizes the convection-diffusion PDEs, its major drawbacks are: it fails to conserve mass and has difficulties in treating general boundary conditions. A variant of the (MMOC), called the "Modified Method of Characteristics with Adjusted Advection" (MMOCAA), has been applied to a number of problems associated with petroleum reservoir analyses and the transport of nuclear contaminants in porous media; this method conserves mass globally (in space) at all time levels and retains all of the computational advantages of the slightly simpler (MMOC). However, it does not necessarily preserve mass locally in space, and there are a number of very important physical problems for which local conservation is essential. The Eulerian-Lagrangian localized adjoint method (ELLAM), does provide, under many circumstances, the desired local conservation in an Eulerian-Lagrangian setting, but only at a computational cost that is several times that of the (MMOC) or (MMOCAA). (ELLAM) was originally designed by Celia *et al.* [31] and Herrera *et al.* [84] for solving one-dimensional constant-coefficient convection-diffusion PDEs. Wang *et al.*[198] used this method in combination with the mixed finite element method (MFEM) to solve a variety of two-dimensional miscible displacement problems of one compressible fluid by another in porous media. (ELLAM) has been successfully applied to linear transport problems of various types.

Douglas *et al.* [54] introduced a new family of locally conservative Eulerian-Lagrangian methods (LCELM) that retains the computational efficiency of the (MMOC) and (MMOCAA) techniques. Moreover, the (LCELM) shows a faster convergence rate of the approximate solution than the (MMOCAA), which is in turn much faster than the (MMOC).

There are very few applications of the above methods to the case of two-phase flows.

A more difficult problem is the solution of multiphase transport processes. This leads to nonlinear advection which greatly complicates the tracking part of the algorithm. Usually some sort of linearization has been used, but this is not dictated by any physical processes and may put restrictions on the timesteps. The tracking algorithm is a major part of any Eulerian-Lagrangian type method. This part consists of tracing flow lines form certain integration points through a fixed spacial grid. Usually the velocity field is calculated as part of the model and the calculation of streamlines may then be done efficiently by ode-solvers like Runge-Kutta methods, which do not depend on any particular representation of the velocity field and are easier to implement. Ask *et al.* [7] uses front-tracking as a fast hyperbolic solver to

advect the solution along the local streamlines. This method, which was used for solving the saturation equation for two-phase flows, may be viewed as an operator splitting method or as an Eulerian-Lagrangian backtracking procedure or as a modified method of characteristics.

An Eulerian-Lagrangian model used to simulate two-phase/particulate flows was developed by Apte *et al.* [4].

Zhou *et al.* [211] developed an improved Eulerian-Lagrangian algorithm that it is claimed to be faster than any previous algorithm, simpler and applicable to any coordinate system. This is an especially important consideration, because they are currently trying to apply this algorithm to the two-phase flow case involving the use of resource-intensive anisotropy-resolving turbulence and dispersion models based on second-moment closure. Comparison of their algorithm with Chen's particle tracking algorithm (see Chen [37]) has been provided.

Sülli [177] combined the Galerkin finite element procedure with a discretization of the Lagrangian material derivative along the characteristics for the Navier-Stokes problem. His method is called the Lagrange-Galerkin method. Achdou and Guermond [1] derived a modification of the above method called a projection/Lagrange-Galerkin method, which differs from Sülli's method in the sense that the convection-diffusion and the incompressibility are dealt with in two different substeps.

Eulerian approach

In the context of bubbly flows, the Eulerian approach consists of solving the Navier-Stokes equations, which govern the fluid motion both inside and outside the bubbles. Since the two fluids have different properties (velocities, pressures, densities, viscosities) the problem of tracking and reconstructing of the interphases was dealt with in different ways yielding various approaches: Lagrangian tracking schemes, interphase/front tracking schemes, level set approach, volume-tracking methods.

The Lagrangian tracking method treats the gas-liquid mixture as a pseudo-continuous phase with variable density. Therefore, each bubble or each group of bubbles of the same radius is followed while moving through the liquid phase. Once its position is determined, the velocity can be readily found and also the momentum equation for each bubble can be written. This method is relatively expensive computationally, in the sense that it is difficult to follow a number of bubbles large enough to be of any practical interest.

Delnoij *et al.* [50] tried to simulate the two-dimensional flow in the flat, partially aerated bubble column of Becker *et al.* [16] in the frame of the Lagrangiang tracking model. They neglected turbulence effects and obtained a quasi-periodic dynamic solution with an undulating

bubble swarm. The stable lower part of the bubble swarm, which is always leaning against the wall in the experiment was not correctly reproduced in the simulation. Also the period of the oscillation was not in agreement with the experiments. This disagreement may be caused by the two-dimensional nature of their model. A direct bubble-bubble interaction model resembling Hoomans' collision model (see Hoomans *et al.* [89]) has also been incorporated. The same team of researchers has also investigated the effect of column to diameter ratio on the overall liquid circulation pattern. They found that the transition from the gulf stream type of liquid circulation to the highly dynamic multiple vortices pattern was somewhere between two and four. This is contrary to the experimentally transition aspect ratio of one described by Chen *et al.* [34]. Delnoij *et al.* [49] investigated the effect of the aspect ratio even further, this time covering the range from 1 to 11.4. The same transition as above was found.

Lapin and Lubbert *et al.* [119] tried to simulate the dynamic behavior of a two-dimensional column of 1.5 m height and 1 m width. They studied the flow driven by a bubble plume, a column gassed at its entire bottom and a cylindrical column. They used the Lagrangian tracking model, but, because the dimensions of their column were quite large, following individual bubbles would have been too expensive. Instead, they considered that bubbles travelled in clusters only and they traced their gross motion. Their model was simplified by assuming a constant slip velocity and no momentum transfer between the phases. The trajectory of the bubble plume is qualitatively similar to the experiments, but no quantitative comparison is shown. For the full bottom aeration case, after 2 s the flow starts to develop instabilities that develop in the next seconds and lead to fingering in the bubble front. The highly irregular motion becomes more orderly in time. The flow is still not stationary after a long time. Sometimes the velocity pattern consisted in two circulation cells, other times in three cells. Interestingly, the two cells circulate in the same sense.

Devanathan *et al.* [52] performed experiments using CARPT and compared them with their numerical predictions. Even though PIV is a more powerful measurement technique, they preferred CARPT since the three-dimensional path of a representative particle, the central quantity of the Lagrangian representation of the flow, cannot easily be obtained with PIV, for instance, on the scale of the entire column. Such a path information can be obtained with CARPT. The flow of a fully aerated bubble column seems chaotic, but it does contain local flow structures of different sizes, the largest being of the size of the column diameter. It is quite difficult to make a quantitative comparison between this chaotic flow and the experiments. The most meaningful measure considered was the mean distance travelled by a particle within a given time interval. The agreement was reasonable. The conclusion of the paper was that

even at low superficial velocities the flow in bubble column reactors is transient and chaotic.

In the volume-tracking scheme a fractional volume is defined that indicates the fraction of a mesh cell that is filled with fluid of a particular type.

Rider and Kothe [155] wrote an impressive overview of the most popular volume-tracking methods, presented from a geometric point of view. Rudman [160] however, preferred an algebraic approach.

In the volume-tracking methods, an advection equation must be solved in such a way that the interface remains sharp. This required the development of very good algorithms. Regular advection-techniques smear the interface over three or four mesh cells quite rapidly. Therefore, the different volume tracking methods must deal with three important aspects: reliable interface reconstruction algorithms (constrain: local volume conservation), accurate computation of the interface normal and the time integration of the volume advection equation. There exist three different approximation techniques when it comes to the interface reconstruction: piecewise constant approximations (Noh and Woodward [135]) (SLIC algorithm - simple line interphase calculation), piecewise constant, stair-stepped (Hirt and Nichols [87]- volume of fluid (VOF) method , Chorin [38], Barr and Ashurst [9]) and piecewise linear (DeBar [47], Youngs [206], Pilliod and Puckett [143]). The last method is the most accurate one but it is computationally more expensive. When computing the interface normal, at first the one-dimensional operator split differences were used. Later people switched to multidimensional operators. The time integration was first performed by means of operator split methods. Pilliod and Puckett [143] utilized a multidimensional algorithms. Recently, due to increasing computation power more refined methods were developed but they were based on the above methods. Such improvements were reported by Mosso [131], Kothe [111], Ashgriz and Poo [6].

Lin *et al.* [122] , as we already discussed in the experimental part of the introduction, used an almost two-dimensional bubble column in their experiments to simulate the so-called 4-region flow, which characterizes the transitional regime towards turbulence. They used the (VOF) to simulate the above experiment. The computational results indicate the unsteady nature of the flow due to the coupling effects of the pressure, liquid velocity and bubble motion. They obtained good agreement with the experiments.

Ginzburg and Wittum [74] created a two-phase 2D model that combines the (VOF) method with implicit staggered finite discretization of the Navier-Stokes equation. However, the capability of their method is tested on the case of a single bubble rise only.

Unverdi and Tryggvason [191] developed a front tracking scheme in which the Lagrangian interphase, represented as an interphase grid, is used to reconstruct a representation of the

density field on a Eulerian mesh with the help of smooth indicator functions. The method is more complicated than the volume tracking methods and requires re-meshing of the interphase if it becomes distorted. Galaktionov *et al.* [72] used this method in the case of strongly deformable geometries.

Esmaeeli *et al.* [64, 65] also used a front tracking method. Jackobsen *et al.* [99] thinks that this is the most promising method when dealing with bubble-driven flows.

Esmaeeli and Tryggvason [66, 67] used a technique that is a hybrid between front capturing and front tracking. They simulated the case of 16 bubbles rising in a doubly periodic box. The initial condition was a slightly perturbed regular array. They also performed fully three-dimensional simulations of four and eight bubbles in a periodic cell. In both cases the bubbles are unstable. The break-up and the bubble-bubble interactions take place by 'drafting, kissing and tumbling'.

Bunner and Tryggvason [26] used a front tracking/finite difference method that allows a fully deformable interphase. They followed the evolution of 91 nearly spherical bubbles that were initially arranged in a regular array that was slightly perturbed. When they start to rise, due to wake-bubble interactions, the array becomes unstable. However, after a while, even though the interaction between the bubbles continue, the average rise velocity becomes essentially steady. This is contrary to the results obtained by Esmaeeli and Tryggvason [67].

Sussman *et al.* [181] presents a level set approach for incompressible two-phase flows. They use the same incompressible Navier-Stokes equations as in the case of interphase tracking schemes. This method introduces a smooth level set function ϕ to represent the free surface. $\phi > 0$ means that only liquid is present in that region, $\phi < 0$ means that only gas is present, therefore $\phi = 0$ describes the free surface. Normally the level set function is maintained as the signed distance to the free surface. This method provides an easy way for computing the normal and the mean curvature of the interphase. More details about this method can be found in Sussman *et al.* [178], Sussman *et al.* [180], Osher and Sethian [137]. Despite its simplicity, this method does not guarantee volume conservation.

Sussman and Puckett [179] combined the level set method with the (VOF) method into a new approach (CLSVOF) - a coupled level set and volume of fluid method that proved to be superior to the previous methods. They only simulated the evolution of one rising bubble in water and the non-axisymmetric merging of two viscous gas bubbles.

All the above methods are still of very limited applicability for real two-phase flow situations. The realistic computations are still not possible because they are beyond the capabilities of the modern computers.

2.3.2 Averaged models

Because of the reduce applicability of the direct methods, many averaging techniques and averaged models have been developed (Anderson and Jackson [2], Drew and Segel [60], Ishii [95]). Averaging is a technique that yields computable two-phase flow models. Instead of considering local instant transfer of interfaces, a collective contribution of interfaces is taken into account in the macroscopic two-phase flow formulation through various constitutive relations.Since in all these models, the numerical grid is fixed, they all are of Eulerian type.

If a distinction among the various averaging models is to be done, then the appropriate criterium would be the averaging procedure used to derive them.

There are two different approaches when deriving the constitutive equations of two-phase flows: the volume averaging and the ensemble averaging.

The volume averaging technique assumes that the two phases are two superimposed continua. Local (space or time) averaged quantities for both phases are introduced. Space or time averaging are then performed yielding continuity and momentum equations for each phase. Some closure relations are also required.

Ishii [95] made a remarkable contribution deriving a general multiphase flow model based on time averaging. Stuhmiller [176] and Antal *et al.* [3] adopted this model for their simulations. All the turbulent models are time-averaging models, too. The extra terms that appear in those derivations appear not because of a different averaging technique, but because of the contribution of fluctuating components of the unknown variables.

Nigmatulin [134] derived a volume averaged model based on the concept of cell averaging.

Delhaye [48] used a space/time averaging technique for one-dimensional two-phase flows and Drew and Lahey [59] developed a three-dimensional two-fluid model using a combination of space and time averaging.

The ensemble-averaging technique is the most fundamentally rigorous form of averaging since the ensemble is a set of flows that can occur at a specified position and time. Therefore, the ensemble-averaging includes all the phasic interactions without specifying the time and length scale. Drew [56], Lahey and Drew [116], Batchelor [11], Biesheuvel and van Winjgaarden [19], Batchelor [14], Biesheuvel and Gorissen [18], Jones and Prosperetti [104], Zhang and Prosperetti [209, 210], Wallis [196], Marchioro *et al.*[126, 127], Wang and Prosperetti [201] used the ensemble averaging technique to derive one-dimensional models.

Arnold [5], Park *el al.*[139] derived multidimensional two-fluid models using ensemble-averaging techniques. Other three-dimensional models derived through averaging belong to Bestion and Barré [17], Bouré [23].

There are two fundamentally different formulations of the macroscopic field equations for two-phase flow systems, namely the two-fluid model and the mixture model. Examples of mixture models are the homogeneous model (the velocities of the two phases are assumed equal) and the drift-flux model and they are adequate to describe dispersed flow regime (see Stewart and Wendroff [175]). To derive a two-fluid model, it is necessary to use ensemble averaging over the individual phases rather then over the entire mixture. Mixture models were derived by Batchelor [11, 12, 13], Biesheuvel and Gorissen [18], to name a few. Whenever detailed information about the flow dynamics is required, the two-fluid models are desirable. Two-fluid models were derived by Biesheuvel and Spoelstra [20], Zhang and Prosperetti [209, 210] etc. Depending of the assumptions used to derive the averaged models, different forms of the above mentioned models can be distinguished: the equal pressure model, the two-fluid two pressure model, the isentropic flow model, the homogeneous equilibrium model, the slip model, the drift flux model etc.

Although these two approaches seem to be very different, they both result in a similar set of equations. The differences appear in the modelling of the interaction terms and in the different forms of the convective terms. A detail analysis of each of the interphase-transfer terms will be provide in the next chapter, so we omit the form of these terms here.

Literature review based on the averaged approach

Park *el al.*[139] used their three-dimensional two-fluid model to study a one-dimensinal non-linear void wave propagation. The continuous phase interfacial pressure difference and the void fraction gradient term in the non-drag force are found to be crucial in determining the behavior of non-linear two-phase bubbly flows.

Antal *et al.* [3] developed a steady-state two-fluid model for laminar bubbly flow and tried to predict the phase distribution in a circular pipe. For fully developed laminar bubbly flows the lateral lift-force and the wall force are found to control the void fraction profile, which presented a local peaking of the void fraction near the wall.

Lammers and Biesheuvel [118] showed that the Batchelor's equations, derived for the case of fluidized beds and used to study the propagation of planar concentration disturbances, can also be applied to bubbly flows. They analyzed the behavior of long, finite-amplitude void fraction waves and concluded that it was governed by Burgers' equation, modified by a source term that accounts for bubble growth. The observed void fraction wave profiles of expansion shock waves and periodic waves could be used to measure the diffusivity of concentration waves. For low void fraction waves the main contribution to the diffusivity term comes from the bulk

elasticity of the bubbles, but for larger void fraction the main role is played by the added-mass term.

León-Becerril and Liné [121] performed a theoretical stability analysis of a bubble column using as starting point the one-dimensional equations of Biesheuvel and Gorissen [18] and Pauchon and Banerjee [141]. Analyzing the differences between the two models, they come up with a unified model able to predict a threshold of the instability close to experiments.

Pan *et al.* [138] , as we have already mentioned in the literature review of the experimental studies, chose the experiments of Mudde *et al.* [132] (PIV) for validation of their numerical scheme. They used the ensemble-averaged system of equations derived by Zhang and Prosperetti [210] and the only turbulent term considered was the bubble-induced turbulence stress. They used a package CFDLIB developed by the Los Alamos National Laboratory (Kashiva and Rauenzahn, [107]). The space is discretized by means of the finite volume method. They also compared their results with Lin *et al.* [122] and they obtained good agreement. This paper shows that, even without a complicated turbulent model, even more, by using a two-dimensional code (the experiments are always three-dimensional, even if the third dimension is negligible) it is possible to get good agreement with the simulations by staying as close as possible of the experimental framework. The dynamic characteristics of the macroscopic coherent structures are well reproduced.

Celik and Wang [32] also used an averaged model to simulate void fraction, gas and liquid profiles similar to the experiments performed by Durst *et al.* [61] and Rietema and Ottengraf [157] in a cylindrical bubble column in the homogeneous regime where the liquids used had higher viscosities than the water. The classical pattern of two large, symmetric cells was obtained.

Coquel *et al.*[44] used an averaged model and an upwind scheme with an original splitting technique to simulate a one-dimensional sedimentation problem, the water faucet problem and a shock tube problem. The efficiency of their numerical technique is highlighted.

L.F. Burns and R.G.Rice [28] used the averaged model derived by Ishii [95] to simulate the liquid circulation profiles that occur in bubble columns where small amounts of surfactant added to the liquid lower the surface tension. They show that uniform circulation can exist even in the bubbly-flow regime.

For high Reynolds numbers, the turbulence models, derived through time averaging, must be used instead. There exist two types of simulations: steady-state and dynamic simulations. Experiments showed that in some cases a dynamic solution is obtained that oscillates with a certain frequency and only after a very long time, the classical steady-state solution is reached.

Schwarz and Turner [165], Ranade [146], Svendsen *et al.* [182], Torvik and Svendsen [186] are among the researchers that performed steady state simulations.

Ranade [146] performed numerical simulations using a SIMPLE algorithm available with the TPFLOW and a power law scheme. Their model was the classical $k-\epsilon$ model. To obtain a circulating flow, an uneven distribution of inlet gas had to be used. This was caused by their steady-state assumption. If a dynamic model would have been used together with a fine enough grid, than the circulation could have been obtained even with a homogeneous aeration at the inlet. Ranade [147] extended his model to include a radially dependent slip velocity and an inward-directed lateral force depending on the slip. He presented exhaustive comparison with experimental data and very good agreement.(see Hills [86], Menzel *et al.*[128], Grienberger and Hofmann [77])

Svendsen *et al.*[182] used the SIMLEC algorithm and the hybrid scheme together with the steady-state $k-\epsilon$ model. The authors compare their results with Menzel *et al.*[128] and conclude that bubble coalescence and breakage must be included in the model if better agreement is to be obtained.

Grevskott *et al.* [76] used the SIMPLE/IPSA algorithm, the upwind scheme and the $k-\epsilon$ model. They extended the CFD model to be able to predict the bubble size distribution. They were actually able to find a correlation between the bubble diameter, the kinetic energy and the dissipation rate.

Thakre *et al.* [183] used the SIMPLE algorithm and the power law scheme. The model was the steady-state $k-\epsilon$ model. They performed experiments in a laboratory scale bubble column to be able to estimate the drift-flux constants. These were used to parameterize the drag. The authors established complete mass and energy balances and obtained a very good match with lots of experimental data over a broad range. Even if this paper considers only the steady-state case, we think their procedure shows a simple and accurate enough procedure for scale up bubble columns.

Becker *et al.*[16], Sokolickin and Eigenberger [170], Pan *et al.*[138] are few examples of good papers where dynamic simulations were performed.

Mudde and Simonin [133] tried to validate their numerical scheme and the mathematical model by comparing their simulations' results with the experiments by Becker *et al.* [16]. Even though this test-case is only of theoretical interest, it is really able to tell if the model can capture the oscillatory movement of a bubble plume that was created by gas injection through a circular sparger, which was located 10 cm to the left of the column center. Since the column was almost flat (the third dimension was small compared to the other two dimensions), they used

the ASTRID code (finite volume method for space discretization, method of characteristics with third-order interpolation for the advective terms and a pressure correction step) and a $k-\epsilon$ and also a low Reynolds $k-\epsilon$ model to simulate both the two-dimensional and the three-dimensional case. Because the experimental setting was close to a two-dimensional column, they first assumed symmetry in the third direction and treated the column as two-dimensional. However, the simulations revealed why that was not a valid simplification. The bubble plume after a very short transition, located itself steadily at the left wall of the vessel. This gave rise to one big circulation cell for the liquid gas. This steady-state solution is contrary to the experimental findings of Becker *et al.* [16]. The same conclusion was reached by Sokolichin and Eigenberger [171] when simulating the two-dimensional case. Therefore, the turbulent viscosity present in the two dimensional $k-\epsilon$ model is too high and produces a-physical results. However, when Mudde and Simonin [133] considered as their domain exactly the flat parallelepiped from the experiments and imposed non-slip boundary conditions the simulations did not reach a steady-state anymore but, after 60 s the flow started to oscillate with a period of 4.44 s, an amplitude of 6.3 cm/s and a mean velocity of 33.4 cm/s. This oscillation is an improvement compared to the two-dimensional case but a quantitative comparison with the experiments revealed that both the amplitude and the oscillation period are smaller than the experimental valued reported by Becker *et al.* [16]. After this negative result, the authors included an added-mass term in their model and the improvement was substantial. The oscillation period increased to 34 s and the amplitude of the oscillations increased, too. These results were in good agreement with the experiments. The period of the oscillations in the experiment was 41 s. For this case, since the superficial gas velocity was only 0.66 mm/s the oscillatory behavior is much longer compared to the cases where the superficial gas velocity at the inlet is higher. This is the reason the steady-state behavior was not measured in this experiment. Becker *et al.* [16] and Sokolichin and Eigenberger [170] tried to simulate this case using a laminar two-dimensional Euler-Euler model based on the SIMPLER algorithm. The finite volume method was used for space discretization. To simplify the numerical calculations, the authors neglected the inertial and the added mass force in the gas momentum, transforming it into a slip relation. The flow simulation based on the laminar model and a coarse spacial grid (18×25 points) gave a stationary result. Increasing the spacial resolution to 36×50 points leads to a transient solution and the oscillatory movement of the plume with a period of 40 s. This shows that even when a dynamic model is used, a grid sufficiently fine must be used in order to capture the dynamic features of the system. The same authors also tried to repeat their simulations using a two-dimensional $k-\epsilon$ turbulent model. The reason they failed to

capture the dynamic behavior with this model was already revealed by Mudde and Simonin [133]. The same authors (Becker *et al.* [16] and Sokolichin and Eigenberger [170]) compared, at a qualitative level only, their simulations with the experimental case of the fully-aerated flat bubble column. They used the same rectangular column as above just that now the column had five individually regulated frits, which give a fairly homogeneous distribution of the gas at the inlet. The simulations show that above a minimum value of 2 cm/s of the superficial gas velocity, an unsteady flow structure develops where a sequence of vortices is created near the distributor. The vortices have a mean diameter corresponding to the column diameter. This unsteady behavior can only be captured with a dynamic solver. The steady state simulations of empty bubble columns converge only if a rather coarse space grid is used. That is why the authors that performed steady-state simulations used grids with a resolution of not more than 20×20 grid points.

Sokolichin *et al.* [172] also used the experiment of Becker *et al.* [16] for validation. They used both the Eulerian and the Lagrangian approach. When the Eulerian model was used they showed that the UPWIND scheme is overly-diffusive, so the TVD (total variation diminution) scheme was preferred. Both TVD-version of the Eulerian approach and the Lagrangian approach produced results in good agreement with the experiments.

Sokolichin and Eigenberger [171] compared the results of the simulations produced by a two-dimensional laminar model, a two-dimensional $k-\epsilon$ model and the three-dimensional $k-\epsilon$ model. The test case was again the locally aerated flat bubble column of Becker *et al.* [16]. They concluded that the only reliable model was the three-dimensional $k-\epsilon$ model. Their findings are very similar to the conclusions of Mudde and Simonin [133]. They criticize the two-dimensional laminar model by arguing that an increasing grid refinement does not lead to a converging solution. They regard the good agreement between the simulations and the experiments reported by Becker *et al.* [16] as a pure coincidence. We think that three-dimensional laminar simulations must be performed before ruling out this model since the third dimension, even small, does play a role in the experiments. If the difference between the two-dimensional and three-dimensional model for the $k-\epsilon$ model was that big, that may be the case for the laminar model, too.

Borchers *et al.* [21] wrote the part II of the study by Sokolichin and Eigenberger [171]. They used the same flat, essentially two-dimensional bubble column but the aeration was central in their (LDA) experiments. In the simulations, the same $k-\epsilon$ model was used. Again, the gas-liquid mixture is represented by a continuity and a Reynolds averaged Navier-Stokes equation. The slip velocity was assumed to be constant, equal to 20 cm/s. It was found that at

aspect ratios of 2 and 3 the flow has a transient character with two staggered rows of vortices moving downwards periodically. Three vortices were observed for the aspect ratio of 2 and four vortices for the ratio of 3. Both quantitative and qualitative agreements with the experiments were obtained.

Pfleger and Becker [142] performed both (LDA) experiments in a three-dimensional cylinder and dynamic flow simulations. They used a $k-\epsilon$ model for the liquid phase. The impact of a bubble-induced turbulence term is also analyzed. Two types of gas distributors were employed: a perforated plate and a ring. The liquid was in batch mode. Different gas flow rates corresponding to the homogeneous flow regime were investigated. They used the CFX 4.3 commercial code for simulations based on a finite volume technique,TVD scheme and a SIMPLEC procedure. The agreement with the experiments was relatively good, but a compromise between grid coarseness and CPU time had to be made. The time-averaged flow structure is well predicted. The reproduction of the dynamic flow behavior on the reactor scale that is dominated by the irregular movement of the bubble plume is a step forward. Of course, further improvement in computers' power would allow more accurate comparisons.

Sanyal *et al.* [162] performed experiments in a cylindrical bubble column (CARPT and CT) under both bubbly and churn turbulent conditions and compared the numerical results produced by the algebraic slip mixture model (ASMM) and the two-fluid Euler-Euler model. Reasonable agreement for the time-averaged gas holdup and the axial liquid velocity profiles.

Jakobsen *et al.* [99], Joshi [105] and Jakobsen [98] have critically and thoroughly reviewed the literature regarding the steady-state turbulent models.

Jakobsen *et al.* [99] makes the important distinction between the dispersed flows and the bubble-driven flows. The dispersed flows are characterized by high liquid velocities, low gas fractions ($<$ 5 - 10 %), almost no bubble-bubble interaction, almost no circulation and peaking near wall (see Antal *et al.* [3]). This situation most frequently occurs in pipes. The bubble-driven flows, on the other hand, are characterized by relatively low gas flow rates (superficial velocity $\leq$ 3 -5 cm/s), generally high void fraction, recirculation, intense interaction between bubbles, often rapid bubble coalescence and large variation in bubble size. This distinction has to be taken into account when choosing the mathematical model. Most of the turbulent models were derived under the assumption of isotropy, which is not valid in many applications. Biesheuvel and Gorissen [18] assumed the flow to be dispersed when deriving their ensemble-averaged model. Batchelor [14] derived his model based on the assumption of small departure from uniformity and zero acceleration of the mixture. That is the reason we should proceed with caution.

2.3.3 Stabilization methods

Most of the numerical methods in the context of direct numerical simulations are of Eulerian type and are based on upstream weighting techniques. They can be regarded as stabilizations or regularizations of the discrete operator, in the sense that they all add a sort of extra diffusion in streamline direction. The disadvantage of these stabilization methods is that they introduce an extra parameter that still has to be determined. Such methods are: the optimal test function methods (see Barrett and Morton [10], Christie *et al.* [39]) that try to mimimize the spatial error and intoduce an upstream bias, different Galerkin and Petrov-Galerkin finite element methods (see Bouloutas and Celia [22], Barrett and Morton [10]), the streamline diffusion finite element method (see Hughes and Brooks [91], Johnson [101], Johnson *et al.* [103]) that adds diffusion only in the direction of streamlines with no cross-wind diffusion introduced, the continuous and discontinuous Galerkin finite element methods (Johnson *et al.* [102], Richter [153], Richter [154]), the monotone upstream-centered scheme for conservation laws (MUSCL) (Colella [42]). Wang *et al.* [199], using a Eulerian-Lagrangian type of method (ELLAM-MFEM) (see previous subchapter) showed that their scheme outperforms the above Eulerian methods in the context of one- and two-dimensional linear convection-dominated PDEs.

The Godunov methods (see Einfeldt [63], Dawson [46]), total variation diminishing methods (TVD) (see Daru and Tenaud [45]) and essentially non-oscillatory methods (ENO) (see Harten *et al.* [82], Shu and Osher [168], van Leer [192]) are examples of numerical schemes well suited for problems that deal with shock discontinuities as well as nonlinear hyperbolic conservation laws without excessive smearing or spurious oscillations.

Other examples of stabilized methods in the context of a finite element formulation are: streamline upwind Petrov-Galerkin (SUPG) (Brooks and Hughes [25]), Galerkin/least-square (GLS) (Hughes *et al.* [92]), Galerkin/gradient least-square, residual-free bubbles method (Brezzi *et al.* [24]), variational multiscale methods (see the subgrid viscosity method by Guermond [80], Hauke [83]).

The numerical methods and stabilization techniques that have been developed for the case of advection-diffusion equations can be generalized to the case of averaged models. However, the most utilized numerical techniques in the context of averaged multiphase flow models are the upwind methods. These methods vary from numerical schemes based on the method of characteristics (see Ferch [69], Romstedt [159]) to more elaborate shock-capturing schemes based on Godunov methods such as Riemann solvers (see Toro [185], Toumi [187], Sainsaulieu [161], Toumi [188], Romate [158], Coquel *et al.* [44], Cocchi *et al.* [41], Saurel and Abgrall [164], Göz *et al.* [75], Faille *et al.* [68]) or flux splitting techniques (Städtke *et al.* [174, 173],

Le Coq *et al.* [120]) or Lax-Wendroff type methods (see Tiselj and Petelin [184]) etc.

Chapter 3

Ensemble averaged model

The ensemble averaging technique is a statistical averaging over an ensemble of realizations of the dispersion. Then a probability density function of finding N bubbles at time t in n volume elements $\delta\mathbf{x}_1, \delta\mathbf{x}_2, ..., \delta\mathbf{x}_N, \delta\mathbf{v}_1, \delta\mathbf{v}_2, ..., \delta\mathbf{v}_N$ around the points $\mathbf{x}_1, \mathbf{x}_2, ..., \mathbf{x}_N, \mathbf{v}_1, \mathbf{v}_2, ..., \mathbf{v}_N$ of a 6 N dimensional phase space is introduced. Consequently, all the flow variables are averaged using the probability density function defined above. The averaged equations for the dispersed phase are obtained by directly ensemble averaging the equations of motion of particles where each particle is treated as a single entity.

The most rigorous form of averaging is the ensemble-averaging technique. However, the terms that arise from the ensemble averaging process must be expressed in terms of the basic two-phase flow variables to achieve closure. It is with these closure laws that the microscale information that was lost during the averaging process is reintroduced.

Stuhmiller [176] chose as his starting point the time-averaging model proposed by Ishii [95]. These formally exact set of equations describe a very wide class of possible two-phase flows. Making simplifying assumptions, Stuhmiller reduces them to a system for which closure depends only on the choice of the internal pressure. His model is one-dimensional. The properties of any final set of equations can be analyzed in terms of the assumptions made. That is the reason, when analyzing models, to first take a look to their assumptions. The first assumption made by Stuhmiller was the neglect of turbulent fluctuations. Secondly, no heat or mass transfer between phases was assumed. Both fluids were separately treated as incompressible. The viscous forces were neglected in the bulk phases (the effects of viscosity in the boundary layer developed around the bubbles is indirectly incorporated). The dispersed phase consists in many small, spherical bubbles with the same constant radius. The final assumption concerns the bulk pressure. The difference between the pressure of the dispersed

phase and that of the continuous phase is totally attributed to the surface tension. Antal *et al.* [3] does not make any simplifying assumption related to the bulk pressures and models the difference between the pressures in a rigorous way, ending up with a more complex set of equations.

Biesheuvel and Wijngaarden [19] derived a one-dimensional model for bubbly flows using an ensemble-averaging technique. Their approach averages the local momentum equations over the entire mixture and results in a momentum equation for it, as opposed to averaging over the separate phases. They assumed an unsteady and spatially inhomogeneous flow of gas bubbles in a slightly viscous incompressible liquid that leads to a large Reynolds number for the relative motion of a single bubble with respect to the bulk motion. Surface tension is supposed to be large enough to keep the bubbles approximately spherical. Since they neglect the velocity perturbations due to the wake and due to the boundary layer, their analysis is only valid for the case of pure liquids. In experiments most of the liquids are contaminated. The bubbles are assumed spherical but their radius may change. The momentum of the mixture is entirely due to the liquid, since the contribution of the gas in their model is neglected. They also assume that the suspension is so dilute that interactions are negligible. Their approximation is accurate in the first order of the void fraction.

Batchelor [14] adopted the same technique of averaging the local momentum equations over the entire mixture and ended up with a one-dimensional model for fluidized beds. He assumed a small departure from uniformity of the dispersion and zero acceleration of the mixture as a whole. Lammers and Biesheuvel [118] used these equations to study the instability of one-dimensional bubbly flows.

Biesheuvel and Gorissen [18] derived a one-dimensional equation for the mixture, assuming in the same way Batchelor did that the bubbly dispersion is uniform in the unperturbed state and it consists of equally sized spherical bubbles with small diameter such that the fluid around the bubbles can be assumed to be laminar. Wall effects are neglected. When turbulence effects become important the expressions of gas pressure and the effective diffusivities must be modified. To model non-uniform flows, they assume that the viscous drag depends on the local void fraction. The fluid impulse remains unaltered when the flow gets perturbed in their approximations. Their equations can be used to describe the effect of a small void fraction disturbance from uniformity as long as the mean volume flux of the dispersion remains constant. However, if the model is to be validated using experiments where the void fraction waves are caused by changes in the supply of one or both of the phases, the model must be modified to allow the mean volume flux to be a function of time.

Prosperetti and Jones [145], Jones and Prosperetti [104], Zhang and Properetti [209, 210], Marchioro *et al.* [125, 126, 127] derived one-dimensional models, but for the case of rigid particles. The phases are assumed to be individually incompressible. The ensemble averaging is carried over the individual phases rather than over the entire mixture. For the disperse phase they average the particle momentum equation directly. In this way, the disperse-phase momentum equation involves the gradient of the continuous rather than the disperse phase pressure. The extraordinary contribution of Prosperetti and his team is the fact that their equations are valid under a very broad range of flows, since they were derived in a general manner. However, when it comes to the closure of their models, only very restrictive cases are considered: the dilute limit, the linear limit. Marchioro *et al.* [125, 126, 127] derived closure relations for the disperse two-phase flow of solid spheres in a viscous fluid. A crucial aspect of their work is that it focuses on systems that are spatially non-uniform on average. Due to this feature, several new terms arise in the constitutive relations that would vanish for the uniform case. Some of these terms confer a non-Newtonian nature to the constitutive equations. A fundamental limitation of the method lies in the assumption of randomly arranged hard-spheres that is not correct for a flowing suspension.

Park *et al.* [139] developed a three-dimensional model for the adiabatic bubbly flows. It is not as general as the models derived by Prosperetti's team but it is three-dimensional. When deriving their model, the following assumptions were made: the fluids are inviscid, incompressible and have constant thermophysical properties; the dispersed phase can be treated as a dilute dispersion of spheres; the nonuniformity in the distribution of the dispersed phase is small.

3.1 Governing Equations

The most general framework the governing equations for two-phase flow can be cast into, at least for the one-dimensional case, is presented below. The equations used by different authors will be obtained as particular cases.

$$\frac{\partial(\epsilon_k \rho_k)}{\partial t} + \nabla \cdot (\epsilon_k \rho_k \mathbf{v}_k) = 0 \tag{3.1}$$

$$\frac{\partial(\epsilon_k \rho_k \mathbf{v}_k)}{\partial t} + \nabla \cdot (\epsilon_k \rho_k \mathbf{v}_k \mathbf{v}_k) = -\epsilon_k \nabla p_k + (p_{ki} - p_k)\nabla \epsilon_k \tag{3.2}$$

$$-\epsilon_k \rho_k \mathbf{g} + (M^i_{kd} + M^i_{kvm} + M^i_{kl} + M^i_{kw}) - \tau_{ki} \cdot \nabla \epsilon_k + \nabla \cdot [\epsilon_k (\tau_k + \tau_k^T)]$$

Here the subscript k denotes the phase ($k = G$ for the gas phase; $k = L$ for the liquid phase) and the subscript i stands for the value at the interphase between the two phases. The ensemble-averaged density, velocity, pressure, volume fraction, viscous shear and bubble-induced turbulence (also called longitudinal turbulent diffusion of momentum by Biesheuvel and Gorissen [18]) are given by ρ_k, $\mathbf{v}_k$, p_k, ϵ_k, τ_k and τ_k^T, respectively. The interfacial transfer of momentum contains: the classical drag force M_{kd}^i, the added-mass force M_{kvm}^i etc. The ensemble-averaged interfacial shear and pressure are denoted by τ_{ki} and p_{ki}.

3.2 Drag force formulation

The interfacial drag force, induced by pressure and viscous stress distribution around the bubbles in steady-state flow, is classically modelled as

$$M_{Gd}^i = -M_{Ld}^i = -A_i \frac{1}{2} \rho_L C_D |\mathbf{u}_r| \mathbf{u}_r \tag{3.3}$$

where A_i represents the projected interfacial area of the bubbles per unit volume and C_D is the drag coefficient. For spherical bubbles, the interfacial drag force becomes (see Park *et al.* [139]):

$$M_{Gd}^i = -M_{Ld}^i = -\frac{3}{8} \frac{C_D}{R_b} \rho_L \epsilon_G |\mathbf{u}_r| \mathbf{u}_r \tag{3.4}$$

Here $\mathbf{u}_r$ represents the slip (relative) velocity between the phases and R_b the radius of the bubble. In most of the models, the classical relative velocity defined in bubbly flows is

$$\mathbf{u}_r = \mathbf{u}_G - \mathbf{u}_L \tag{3.5}$$

However, the relative velocity defined by Simonin and Viollet [169], and later by Biesheuvel and Gorissen [18] is:

$$\mathbf{u}_r = \mathbf{u}_G - \mathbf{u}_L - \mathbf{u}_D, \tag{3.6}$$

where $\mathbf{u}_D$ is the drift velocity induced by the gas dispersion and it is modelled by

$$\mathbf{u}_D = -\frac{\delta_e}{\epsilon_G} \nabla \epsilon_G. \tag{3.7}$$

This unifying approach was done by León-Becerril and Liné [121]. However, one important observation must be done here. If comparison with experiments of Biesheuvel and Gorissen [18] is to be made, the equations must be either redefined with respect to a laboratory (reference) frame, or a transformation of the final results must be made. Therefore, consistency is extremely important.

In bubble columns, with no liquid flow rate, the diffusivity δ_e cannot be modelled by reference to turbulent shear flow in the liquid. However, the gas phase induces a "pseudo-turbulence" that was modelled by Batchelor [14] and Biesheuvel and Gorissen [18] as:

$$\delta_e(\epsilon_G) = R_b u_r \left(H(\epsilon_G)\right)^{1/2}. \tag{3.8}$$

According to Batchelor's definition,

$$H(\epsilon_G) = \frac{\epsilon_G}{\epsilon_{Gcp}}\left(1 - \frac{\epsilon_G}{\epsilon_{Gcp}}\right), \tag{3.9}$$

where ϵ_{Gcp} represents the void fraction corresponding to close packing. In the case of bubbly flows, $\epsilon_{Gcp} = 1$.

For undistorted spherical bubbles, the interfacial drag coefficient proposed by Ishii and Zuber [96] is:

$$C_D = 24\frac{(1 + 0.1Re_b^{0.75})}{Re_b}, \tag{3.10}$$

where Re_b is either the regular Reynolds number if the volume fraction is low or, for higher void fraction, the Reynolds number is based on the mixture viscosity:

$$Re_b = \frac{2\rho_L |v_r| R_b}{\mu_m}, \tag{3.11}$$

$$\mu_m = \mu_L (1 - \epsilon_G)^{-2.5\mu_m^*}, \tag{3.12}$$

$$\mu_m^* = \frac{\mu_G + 0.4\mu_L}{\mu_G + \mu_L}. \tag{3.13}$$

For distorted bubbles, Harmathy [81] proposed the following drag coefficient where σ stands for the surface tension:

$$C_D = \frac{4}{3} R_b \left[\frac{g(\rho_L - \rho_G)}{\sigma \epsilon_L}\right]^{\frac{1}{2}}. \tag{3.14}$$

The drag proposed by Ishii and Zuber [96] is valid in the viscous region ($0 \leq$ Re $\leq$ 500-1000). In the turbulent region the bubbles become distorted and the following correlation may be preferred:

$$C_D = \frac{2}{3} Eo^{\frac{1}{2}}, \tag{3.15}$$

where Eo is the Eotvos number defined as:

$$Eo = \frac{g\Delta\rho D_b^2}{\sigma}. \tag{3.16}$$

In the distorted particle regime, if the volume fraction is high than Ishii and Zuber propose a modification in the form of a multiplying factor to the drag. The factor is a function of void fraction:

$$E = \left(\frac{1 + 17.67 f(\epsilon_G)^{\frac{6}{7}}}{18.67 f(\epsilon_G)} \right)^2, \tag{3.17}$$

where

$$f(\epsilon_G) = \frac{\mu_1}{\mu_m} (1 - \epsilon_G)^{\frac{1}{2}}. \tag{3.18}$$

Even though the drag proposed by Ishii and Zuber is widely used, different authors chose different drag correlations. Biesheuvel and Gorissen [18], for instance, derived the following drag force:

$$M_d = \frac{9\mu_L}{R_b^2} \epsilon_G \mathbf{u}_r. \tag{3.19}$$

Clift *et al.* [40] suggest another form of the drag coefficient, which gives a good fit to numerical predictions of drag on spherical bubbles (for $Re \gg 2$) where v_∞ represents the terminal velocity:

$$C_D = 14.9 Re^{-0.78}, \quad \text{where} \quad Re = \frac{\rho_L R_b v_\infty}{\mu_L}.$$

Many other possible correlations exist in the literature. Joshi [105] reviews some of them, however they are mainly used by different authors in the turbulent regime where even a radial dependence is suggested.

3.3 Added-mass force formulation

The added-mass force accounts for the loss of momentum of an accelerating particle needed to accelerate the surrounding fluid in the opposite direction, so it is induced by pressure distribution around the bubbles in accelerated flow. Biesheuvel and Gorissen [18] suggested the following form of the virtual-mass (added-mass) force, if the mixture velocity is to be used as the reference velocity.

$$M^i_{Gvm} = -M^i_{Lvm} = \epsilon_G \rho_L \mu(\epsilon_G) \frac{D_{\mathbf{u}_G}(\mathbf{u}_G - \mathbf{u}_L)}{Dt}, \tag{3.20}$$

where

$$\mu(\epsilon_G) = \frac{1}{2} \frac{1 + 2\epsilon_G}{1 - \epsilon_G}, \tag{3.21}$$

$$\frac{D_{\mathbf{u}_G}(\mathbf{u}_G - \mathbf{u}_L)}{Dt} := \frac{\partial(\mathbf{u}_G - \mathbf{u}_L)}{\partial t} + \mathbf{u}_G \cdot \nabla(\mathbf{u}_G - \mathbf{u}_L). \tag{3.22}$$

Stuhmiller [176] was the first one to come up with the above formulation. Minev [130] performed a linear and a non-linear analysis of different models and concluded that the above form yields a system of differential equations that possesses real characteristics. However, similar studies suggest different added-mass formulations. Park *et al.* [139], for instance, derived a model that possesses real characteristics even though his added-mass formulation is:

$$M^i_{Gvm} = -M^i_{Lvm} = \frac{1}{2}\epsilon_G \rho_L \frac{D(\mathbf{u}_G - \mathbf{u}_L)}{Dt}, \tag{3.23}$$

where

$$\frac{D(\mathbf{u}_G - \mathbf{u}_L)}{Dt} := \frac{\partial \mathbf{u}_G}{\partial t} + \mathbf{u}_G \cdot \nabla \mathbf{u}_G - \frac{\partial \mathbf{u}_L}{\partial t} + \mathbf{u}_L \cdot \nabla \mathbf{u}_L. \tag{3.24}$$

The above form of the virtual-mass term was first proposed by Jackson [97]. He also proposed the following formulation:

$$\frac{D(\mathbf{u}_G - \mathbf{u}_L)}{Dt} := \frac{\partial(\mathbf{u}_G - \mathbf{u}_L)}{\partial t} + (\mathbf{u}_G - \mathbf{u}_L) \cdot \nabla(\mathbf{u}_G - \mathbf{u}_L), \tag{3.25}$$

Homsy *et al.* [88] came with a forth alternative formulation:

$$\frac{D(\mathbf{u}_G - \mathbf{u}_L)}{Dt} := \frac{\partial \mathbf{u}_G}{\partial t} + (\mathbf{u}_G - \mathbf{u}_L) \cdot \nabla \mathbf{u}_G - \frac{\partial \mathbf{u}_L}{\partial t} - (\mathbf{u}_G - \mathbf{u}_L) \cdot \nabla \mathbf{u}_L, \tag{3.26}$$

Jones and Prosperetti [104] adopted a form of the added mass term developed by Drew *et al.* [57] based on the objectivity principle of continuum mechanics. It has the form:

$$M^i_{Gvm} = C_M \epsilon_G \epsilon_L (\rho_G \epsilon_G + \rho_L \epsilon_L) \frac{D(\mathbf{u}_G - \mathbf{u}_L)}{Dt}, \tag{3.27}$$

where

$$\frac{D(\mathbf{u}_G - \mathbf{u}_L)}{Dt} := \frac{\partial(\mathbf{u}_G - \mathbf{u}_L)}{\partial t} + [(2-\lambda)\mathbf{u}_G + (\lambda - 1)\mathbf{u}_L] \cdot \nabla \mathbf{u}_L - [\lambda \mathbf{u}_L + (1-\lambda)\mathbf{u}_G] \cdot \nabla \mathbf{u}_G, \tag{3.28}$$

where C_M is a dimensionless parameter and $0 \leq \lambda \leq 2$. Performing a linear analysis of the equations, Jones and Prosperetti [104] derived a stability condition that was also drag dependent. For his expression of drag, the condition is satisfied by $C_M \geq 1$ for any λ in the range $(0, 2)$.

León-Becerril and Liné [121] used a more general expression for the virtual mass force

$$\begin{aligned} M^i_{Gvm} = (1-\epsilon_G)^{n+1} \Big[& \epsilon_G \rho_L \mu(\epsilon_G) \left(\frac{D_G \mathbf{u}_G}{Dt} - \frac{D_L \mathbf{u}_L}{Dt} \right) \\ & + C_{m1} \epsilon_G \rho_L (\mathbf{u}_G - \mathbf{u}_L) \cdot \nabla (\mathbf{u}_G - \mathbf{u}_L) + C_{m2} \rho_L (\mathbf{u}_G - \mathbf{u}_L)^2 \nabla \epsilon_G \Big]. \end{aligned} \tag{3.29}$$

In order to obtain the expression of added mass force of Biesheuvel and Gorissen [18], this time with the liquid velocity as the reference velocity,

$$M^i_{Gvm} = (1-\epsilon_G)\left(\frac{\partial}{\partial t}[\rho_L \epsilon_G \mu(\epsilon_G)(\mathbf{u}_G - \mathbf{u}_L)] + \nabla \cdot [\rho_L \epsilon_G \mu(\epsilon_G)\mathbf{u}_G(\mathbf{u}_G - \mathbf{u}_L)]\right), \tag{3.30}$$

the corresponding functions $C_{m1}(\epsilon_G)$ and $C_{m2}(\epsilon_G)$ are given by

$$\begin{aligned} C_{m1}(\epsilon_G) &= \epsilon_G(\mu - (1-\epsilon_G)\mu'), \\ C_{m2}(\epsilon_G) &= \epsilon_G(\mu + \epsilon_G\mu'), \\ n &= 0. \end{aligned} \tag{3.31}$$

The prime denotes the derivation with respect the void fraction.

If $C_{m1} = 0$, $C_{m2} = 0$ and $n = -1$ then the added mass proposed by Prosperetti and Jones [145], Pauchon and Barnerjee [140] and Lahey [115] is obtained.

In the added-mass term used by Biesheuvel and Gorissen [18], the added-mass coefficient $\mu(\epsilon_G)$ was suggested by Zuber. However, other forms are available in the literature. van Wijngaarden [193] used:

$$\mu(\epsilon_G) = \frac{1}{2}(1 + 2.78\epsilon_G). \tag{3.32}$$

Kok (1989) [110] adopted the form proposed by Jeffrey (1973) [100]:

$$\mu(\epsilon_G) = \frac{1}{2}(1 + 3.22\epsilon_G). \tag{3.33}$$

Biesheuvel and Spoelstra [20] analyzed the different added-mass coefficients available and showed that the difference between these dilute-limit results were due to the different assumptions implicitly made. They showed that any of them can be used for the case of dilute suspensions. For the non-dilute case, however, Zuber's coefficient should be used.

3.4 Lift force formulation

The lift-force on a bubble has been calculated by Drew and Lahey [58]. It is perpendicular to the rotation vector and to the velocity of the bubble. Its general form can be written as

$$M^i_{Gl} = -M^i_{Ll} = C_L \phi \rho_L (\mathbf{u}_G - \mathbf{u}_L) \times (\nabla \times \mathbf{u}_L). \tag{3.34}$$

C_L represents the lift coefficient and can be ranged from 0.01 to 0.5 (see Wang *et al.* [200]). Park *et al.* [139] obtained this force when deriving their three-dimensional ensemble-averaged model. The value of the lift coefficient in their case was 0.5. The lift force also appeared in the form of the equations derived by Zhang and Prosperetti [209].

3.5 Wall force formulation

When a rising bubble comes closely to the wall, the non-slip condition slows the drainage rate between the bubble and the wall which in turn increases the drainage rate on the opposite side. Thus a hydrodynamic force appears that acts to drive the bubble away from the wall. There is a lot of ambiguity concerning this force. That is the reason most authors omit it in their formulations. Antal *et al.* [3] derived the following expression using an approximate two-dimensional solution.

$$M^i_{Gw} = -M^i_{Lw} = \frac{\epsilon_G \rho_L |\mathbf{u}_{||}|^2}{R_b} \left[C_{W1} + C_{W2} \left(\frac{R_b}{y_0} \right) \right] \mathbf{n}_w, \tag{3.35}$$

where

$$\mathbf{u}_{||} = (\mathbf{u}_G - \mathbf{u}_L) - [\mathbf{n}_w \cdot (\mathbf{u}_G - \mathbf{u}_L)]\mathbf{n}_w \tag{3.36}$$

$$C_{W1} = -0.104 - 0.06 U_R, \tag{3.37}$$

$$C_{W2} = 0.147. \tag{3.38}$$

Here y_0 is the distance between the bubble and the wall, $\mathbf{n}_w$ is the unit outward normal vector on the surface of the wall and U_R is the relative velocity between the phases in the tangential direction.

3.6 Pressure and shear stress terms

The equal pressure models assume that the pressures of the two phases are equal. (see Drew *et al.* [57]). The drift flux model proposed by Biesheuvel and Gorissen [18] is also an equal pressure model. However, since the term containing the drift velocity is proportional to the gradient of the void fraction, the model implicitly introduces a difference between the two pressures. Simonin and Viollet [169], even though they used a drift flux model similar to the one of Biesheuvel and Gorissen [18], on top of the void fraction gradient, they explicitly assume different pressures for the two phases. This feauture of the model was included by León-Becerril and Liné [121] into their model.

In the two-pressure models, it can be assumed that the gas interphase pressure is very similar to the averaged pressure of the gas:

$$p_G - p_{Gi} = 0. \tag{3.39}$$

For the liquid phase, Antal *et al.* [3] and Park *et al.* [139] (Prosperetti and Jones [145] and Stuhmiller [176] used similar expressions) derived the following formula:

$$p_L - p_{Li} = c_p \, \rho_L \, \epsilon_L \, \mathbf{v}_r \cdot \mathbf{v}_r. \tag{3.40}$$

In both Antal and Park's cases, the derived value for c_p was 1/4. However, in practice, Park *et al.* [139] noticed that $c_p = 1/2$ works better.

For spherical bubbles, the most general form of the overall gas to liquid phase pressure difference, as presented by Ishii [95] and Antal *et al.* [3] is

$$(p_G - p_L)I = \frac{2\sigma}{R_b} I + (p_{Li} - p_L)I - \tau_{Li}. \tag{3.41}$$

In many cases, simplified versions of (3.41) can be used. For instance, the interfacial shear stress tensor of the liquid phase has been neglected by Park *et al.* [139] and Biesheuvel and van Wijngaarden [19] and the surface tension was neglected by Park *et al.* [139] and Zhang and Prosperetti [209]. If both simplifying assumptions are made, then combining (3.40) with (3.41) yields

$$(p_G - p_L)I = -c_p \, \rho_L \, \epsilon_L \, \mathbf{v}_r \cdot \mathbf{v}_r \, I. \tag{3.42}$$

However, if no simplifying assumptions are to be made, than the liquid interfacial shear stress tensor can be assumed equal to the total shear stress in the liquid at the surface of the bubble, i.e. $\tau_{Li} = \tau_L + \tau_L^T$, evaluated at the surface of the bubble. τ_L can be easily evaluated using a Newtonian shear law as Antal *et al.* [3] did. τ_L^T can be expressed according to Nigmatulin [134] (also see Simonin and Violler [169], Lahey [115]) as:

$$\tau_L^T = -\epsilon_G \rho_L \left[\frac{3}{20} |\mathbf{u}_G - \mathbf{u}_L|^2 I + \frac{1}{20} (\mathbf{u}_G - \mathbf{u}_L) \otimes (\mathbf{u}_G - \mathbf{u}_L) \right]. \tag{3.43}$$

The final form of the liquid interfacial shear stress tensor becomes (as in Antal *et al.* [3])

$$\tau_{Li} = \mu_L \nabla \mathbf{u}_L - \rho_L \left[\frac{3}{20} |\mathbf{u}_G - \mathbf{u}_L|^2 I + \frac{1}{20} (\mathbf{u}_G - \mathbf{u}_L) \otimes (\mathbf{u}_G - \mathbf{u}_L) \right]. \tag{3.44}$$

Combining (3.44) with (3.41) and (3.40) the jump condition for the pressure becomes

$$\begin{aligned} (p_G - p_L)I = \frac{2\sigma}{R_b} I - c_p \, \rho_L \, \epsilon_L \, |\mathbf{u}_G - \mathbf{u}_L|^2 I - \mu_L \nabla \mathbf{u}_L + \rho_L \frac{3}{20} |\mathbf{u}_G - \mathbf{u}_L|^2 I \\ + \rho_L \frac{1}{20} (\mathbf{u}_G - \mathbf{u}_L) \otimes (\mathbf{u}_G - \mathbf{u}_L). \end{aligned} \tag{3.45}$$

For the gas phase, Antal *et al.* [3] made the following assumptions:

$$\tau_G = \tau_G^T = \tau_{Gi} = 0. \tag{3.46}$$

Even though most papers modeled only τ_L and τ_L^T, Biesheuvel and Gorissen [18] made an attempt to model τ_G and τ_G^T (the viscous shear stress and the bubble-induced turbulent shear stress) for the gas phase. The term τ_G^T accounts for a "kinetic" contribution of an effective pressure related to the fluctuations of the velocities, $(\rho_G + \rho_L\mu(\epsilon_G))\overline{\Delta v^2}$. The variance of the fluctuating velocities of the bubbles is expressed after Batchelor [14]:

$$\overline{\Delta v^2} = H(\epsilon_G)|v_r|^2. \tag{3.47}$$

The longitudinal turbulent diffusion term becomes

$$\tau_G^T = H(\epsilon_G)(\rho_G + \rho_L\mu(\epsilon_G))|v_r|^2 I. \tag{3.48}$$

The viscous shear stress according to Biesheuvel and Gorissen [18] has the form

$$\tau_G = (\rho_G + \rho_L\mu(\epsilon_G))R_d v_r \nabla u_G. \tag{3.49}$$

Biesheuvel and Gorissen [18] omitted in their model any other shear stress tensor, therefore:

$$\tau_L = \tau_L^T = \tau_{Li} = \tau_{Gi} = 0. \tag{3.50}$$

León-Becerril and Liné [121] combined the models of Biesheuvel and Gorissen [18] and Simonin and Viollet [169], in the sense that the diffusion is modelled both in the gas and in the liquid phase. They used (3.43), (3.48) and they omitted the other shear stress tensors, which means that in their model

$$\tau_L = \tau_G = \tau_{Li} = \tau_{Gi} = 0. \tag{3.51}$$

Chapter 4

Numerical scheme

4.1 General description of the numerical scheme

The governing equations of any ensemble averaged two-phase flow model can be regarded as a generalization of the Navier-Stokes equations. Our scheme is an extension of the finite element projection/Lagrange-Galerkin method for the incompressible Navier-Stokes equations of Achdou and Guermond [1] and of the stabilization technique of Galerkin approximations of transport equations by sub-grid modelling of Guermond [79]. The second technique is proved to have stability and convergence properties that are similar to that of the streamline diffusion method. Regarding the first method, Achdou and Guermond [1] showed that, provided that the time step, δt is of $\mathcal{O}(h^{d/4})$, where h is the mesh-size and d is the space dimension ($2 \leq d \leq 3$), the proposed method yields for finite time T an error of $\mathcal{O}(h^{l+1} + \delta t)$ in the L^2 norm for the velocity and an error of $\mathcal{O}(h^l + \delta t)$ in the H^1 norm (or the L^2 norm for the pressure), where l is the polynomial degree of the approximate velocity.

Their numerical implementation reduces to the one- and two-dimensional Navier-Stokes equations. We implemented our scheme in three dimensions and for the case of ensemble averaged two-phase flows. The convergence of the scheme for our case has proved to be extremely difficult, therefore the interested reader is referred to the convergence results obtained by Achdou and Guermond [1] and by Guermond [79] .Remember that the above mentioned papers can give only a fair idea of what kind of expectations we may have from our numerical scheme.

Throughout the thesis, more then one form of the coefficients will be used. However, the major steps of the discretization scheme will remain the same. That is why we only present the discretization scheme for one set of parameters. If additional terms are used later, their

discretization follows the same idea. The set of equations for which we present in detail the numerical scheme is basically the one proposed by Stuhmiller [176]. This discretization scheme has already been published [1].

$$\frac{\partial \Phi}{\partial t} + \nabla \cdot (\Phi \mathbf{v}) = 0 \tag{4.1}$$

$$\frac{\partial (1-\Phi)}{\partial t} + \nabla \cdot ((1-\Phi)\mathbf{u}) = 0 \tag{4.2}$$

$$\Phi \rho_2 \frac{D_{\mathbf{v}}\mathbf{v}}{Dt} = -\Phi \nabla p - \xi(\Phi)\nabla\Phi - \beta(\Phi)(\mathbf{v}-\mathbf{u}) - \Phi\rho_2\mathbf{g} - \Phi\rho_1\mu(\Phi)\frac{D_{\mathbf{v}}(\mathbf{v}-\mathbf{u})}{Dt} + \nabla\cdot(\mu_d(\Phi)\nabla\mathbf{v}) \tag{4.3}$$

$$(1-\Phi)\rho_1 \frac{D_{\mathbf{u}}\mathbf{u}}{Dt} = -(1-\Phi)\nabla p + \xi(\Phi)\nabla\Phi + \beta(\Phi)(\mathbf{v}-\mathbf{u}) - (1-\Phi)\rho_1\mathbf{g} + \Phi\rho_1\mu(\Phi)\frac{D_{\mathbf{v}}(\mathbf{v}-\mathbf{u})}{Dt} \tag{4.4}$$

where $\mathbf{v}$ is the velocity of the dispersed phase, $\mathbf{u}$ is the velocity of the continuous phase, Φ is the volume fraction (gas volume concentration) of the dispersed phase and p stands for the pressure. ρ_1, ρ_2 represent the densities of the continuous and dispersed phase respectively. The bold notation is used for three-dimensional vectors.

In the above equations the material (total) derivatives $\frac{D_{\mathbf{v}}}{Dt}$ and $\frac{D_{\mathbf{u}}}{Dt}$ stand for:

$$\frac{D_{\mathbf{v}}\mathbf{w}}{Dt} := \frac{\partial \mathbf{w}}{\partial t} + \mathbf{v}\cdot\nabla\mathbf{w}$$

$$\frac{D_{\mathbf{u}}\mathbf{w}}{Dt} := \frac{\partial \mathbf{w}}{\partial t} + \mathbf{u}\cdot\nabla\mathbf{w}$$

The form of the coefficients proposed by Biesheuvel and Gorissen [18] (see also Minev *et al.* [130]) is used to illustrate the discretization technique. As we said above, any other coefficients can be used instead. We are only examining the numerical scheme here.

$$\mu(\Phi) = \frac{1}{2}\frac{1+2\Phi}{1-\Phi}$$

$$\beta(\Phi) = \frac{9\mu_c}{r_d^2}\Phi$$

$$\xi(\Phi) = \frac{9\mu_c}{r_d^2}\frac{\delta_e}{1-\Phi} + (1-\Phi)\frac{\partial p_e}{\partial \Phi}$$

$$\delta_e(\Phi) = r_d v_0(\Phi)(H(\Phi))^{\frac{1}{2}}$$

$$p_e(\Phi) = \Phi(\rho_2 + \rho_1\mu(\Phi))H(\Phi)v_0^2(\Phi)$$

[1] The numerical scheme has been published in [30]

$$\mu_d(\Phi) = \Phi(\rho_2 + \rho_1\mu(\Phi))r_d v_0(\Phi)H^{\frac{1}{2}}(\Phi)$$

$$v_0(\Phi) = v_\infty(1-\Phi)^2$$

$$H(\Phi) = \frac{\Phi}{\Phi_{cp}}\left(1 - \frac{\Phi}{\Phi_{cp}}\right)$$

$$v_\infty = \frac{(\rho_1 - \rho_2)gr_d^2}{9\mu_c}$$

where the void fraction of close packing is denoted by Φ_{cp}, the viscosity of the continuous phase by μ_c, the radius of a bubble (assumed to be spherical) by r_d, the velocity of a single bubble rising under the action of gravity in an infinite liquid by v_∞ and the mean velocity of rise of a uniform suspension in a stagnant liquid by $v_0(\Phi)$. We set $\Phi_{cp} = 1.0$, $\mu_c = 0.001$, $r_d = 0.0004$, $\rho_1 = 998$, $\rho_2 = 1.2$.

The first two equations represent the conservation of mass of each phase and implicitly assume that no mass transfer occurs between the phases. The second pair of equations is a statement of the momentum balance for each phase.

The above set of equations accepts a trivial solution representing a uniform dispersion:

$$\Phi = \Phi_0, \quad \mathbf{u} = (0,0,0), \quad \mathbf{v} = (0,0,v_*) = \frac{\Phi_0(1-\Phi_0)(\rho_1 - \rho_2)\mathbf{g}}{\beta(\Phi_0)} \tag{4.5}$$

$$\nabla p = -(\Phi_0\rho_2 + (1-\Phi_0)\rho_1)\mathbf{g}$$

For the numerical study, it is more convenient to use the dimensionless form of the equations. To perform the non-dimensionalization we choose the characteristic velocity to be v_* and the characteristic length to be $l(= 0.04)$. The dimensionless variables are:

$$\mathbf{x}' = \frac{\mathbf{x}}{l}, \quad t' = \frac{tv_*}{l}, \quad \mathbf{u}' = \frac{\mathbf{u}}{v_*}, \quad \mathbf{v}' = \frac{\mathbf{v}}{v_*}, \quad p' = \frac{p}{\rho_1 v_*^2}.$$

We also make use of the following notations:

$$\alpha = \frac{\rho_2}{\rho_1} \qquad \text{(density ratio)}$$

$$Fr = \frac{\rho_1}{\rho_1 - \rho_2}\frac{v_*^2}{gl} \qquad \text{(Froude number)}$$

Then, dropping the primes, the equations (4.1)-(4.4) become,

$$\frac{\partial\Phi}{\partial t} + \nabla\cdot(\Phi\mathbf{v}) = 0 \tag{4.6}$$

$$\frac{\partial(1-\Phi)}{\partial t} + \nabla\cdot((1-\Phi)\mathbf{u}) = 0 \tag{4.7}$$

$$
\begin{aligned}
\Phi\frac{D_{\mathbf{v}}\mathbf{v}}{Dt} &= -\frac{1}{\alpha}\Phi\nabla p - \left(\frac{1}{Fr}\frac{1}{\alpha}\frac{r_d}{l}(1-\Phi)H^{\frac{1}{2}}(\Phi)\right.\\
&\left.+\frac{\partial\{\Phi(1+\frac{1}{\alpha}\mu(\Phi))H(\Phi)(1-\Phi)^4\}}{\partial\Phi}\frac{(1-\Phi)}{(1-\Phi_0)^2}\right)\nabla\Phi\\
&-\frac{1}{Fr}\frac{1}{\alpha}(1-\Phi_0)\Phi(\mathbf{v}-\mathbf{u}) - \frac{1}{Fr}\frac{\Phi}{1-\alpha}(0,0,1) - \frac{1}{\alpha}\Phi\mu(\Phi)\frac{D_{\mathbf{v}}(\mathbf{v}-\mathbf{u})}{Dt}\\
&+\frac{r_d}{l}\nabla\cdot\left(\Phi(1+\frac{1}{\alpha}\mu(\Phi))\frac{(1-\Phi)^2}{1-\Phi_0}H^{\frac{1}{2}}(\Phi)\nabla\mathbf{v}\right)
\end{aligned}
\tag{4.8}
$$

$$
\begin{aligned}
(1-\Phi)\frac{D_{\mathbf{u}}\mathbf{u}}{Dt} &= -(1-\Phi)\nabla p + \left(\frac{1}{Fr}\frac{r_d}{l}(1-\Phi)H^{\frac{1}{2}}(\Phi)\right.\\
&\left.+\frac{\partial\{\Phi(\alpha+\mu(\Phi))H(\Phi)(1-\Phi)^4\}}{\partial\Phi}\frac{(1-\Phi)}{(1-\Phi_0)^2}\right)\nabla\Phi\\
&\frac{1}{Fr}(1-\Phi_0)\Phi(\mathbf{v}-\mathbf{u}) - \frac{1}{Fr}\frac{1-\Phi}{1-\alpha}(0,0,1) + \Phi\mu(\Phi)\frac{D_{\mathbf{v}}(\mathbf{v}-\mathbf{u})}{Dt}
\end{aligned}
\tag{4.9}
$$

The numerical scheme can be considered as a generalization of a projection method for the incompressible Navier-Stokes equations. Since this problem is convection dominated, the convection terms are split from the system and are solved by the method of characteristics.

Let us consider the governing equations (4.6), (4.7), (4.8) and (4.9). Provided that the velocities of the continuous and dispersed phases at time levels $n-1$ and n, i.e., $\mathbf{u}^{n-1}, \mathbf{u}^n, \mathbf{v}^{n-1}$ and $\mathbf{v}^n$, the void fraction at time levels $n-1$ and n (Φ^{n-1} and Φ^n) and the pressure at level n (p^n) are known, we can advance them to the level $n+1$ by performing the following steps involving an operator-splitting technique (see Maday *et al.* [124]).

(i) Advection sub-step

$$
\begin{aligned}
&\frac{\partial\tilde{\Phi}^{n-i}(s)}{\partial s} = -(\tilde{\mathbf{v}}^{n-i}(s)\cdot\nabla)\tilde{\Phi}^{n-i}(s), \quad 0\le s\le(i+1)\Delta t, \quad i=0,1\\
&\tilde{\Phi}^{n-i}(0) = \Phi^{n-i}
\end{aligned}
\tag{4.10}
$$

$$
\begin{aligned}
&\frac{\partial\tilde{\mathbf{u}}^{n-i}(s)}{\partial s} = -(\tilde{\mathbf{u}}^{n-i}(s)\cdot\nabla)\tilde{\mathbf{u}}^{n-i}(s), \quad 0\le s\le(i+1)\Delta t, \quad i=0,1\\
&\tilde{\mathbf{u}}^{n-i}(0) = \mathbf{u}^{n-i}
\end{aligned}
\tag{4.11}
$$

and

$$
\begin{aligned}
&\frac{\partial\tilde{\mathbf{v}}^{n-i}(s)}{\partial s} = -(\tilde{\mathbf{v}}^{n-i}(s)\cdot\nabla)\tilde{\mathbf{v}}^{n-i}(s), \quad 0\le s\le(i+1)\Delta t, \quad i=0,1\\
&\tilde{\mathbf{v}}^{n-i}(0) = \mathbf{v}^{n-i}
\end{aligned}
\tag{4.12}
$$

where $\tilde{\Phi}^{n-i}(i=0,1)$, $\tilde{\mathbf{u}}^{n-i}(i=0,1)$ and $\tilde{\mathbf{v}}^{n-i}(i=0,1)$ are the "advected" parts of the void fraction and of the velocity fields. These pure convective equations are solved by means of the method of characteristics, which can be described as follows.

Let us first introduce the characteristic curves $\mathbf{X}_{\mathbf{x}}^{n+1}$, as solutions of the following problems,

$$\frac{d\mathbf{X}_{\mathbf{x}}^{n+1}}{dt} = \mathbf{u}\Big(\mathbf{X}_{\mathbf{x}}^{n+1}(t), t\Big), \quad in \quad [t^{n-i}, t^{n+1})$$
$$\mathbf{X}_{\mathbf{x}}^{n+1}(t^{n+1}) = \mathbf{x},$$

where $\mathbf{u}(X_{\mathbf{x}}^{n+1}(t), t)$ is the velocity of the continuous phase and $\mathbf{x}$ is an arbitrary point within the solution domain where the characteristic terminates at time level t^{n+1}. We refer to the point $\mathbf{X}_{\mathbf{x}}^{n+1}(t^{n-i})$ as the foot of the corresponding characteristics. The convected velocity field is then given by:

$$\tilde{\mathbf{u}}^{n-i}(x) = \mathbf{u}^{n-i}(\mathbf{X}_{\mathbf{x}}^{n+1}(t^{n-i})), \quad i = 0, 1$$

In order to discretize this equation we use a first order Euler explicit scheme and the extrapolated velocity

$$\mathbf{u}_e^{n+1} = 2\mathbf{u}^n - \mathbf{u}^{n-1}$$

to obtain

$$\mathbf{X}_{\mathbf{x}}^{n+1}(t^{n-i}) = \mathbf{X}_{\mathbf{x}}^{n+1}(t^{n+1}) - (i+1)\ \Delta t\ \mathbf{u}_e^{n+1}, \quad i = 0, 1.$$

Once the feet of the characteristics $\mathbf{X}_{\mathbf{x}}^{n+1}(t^{n-i})$ are determined, the velocities are interpolated using the finite element interpolant at time t^{n-i} to obtain the velocity fields $\tilde{\mathbf{u}}^{n-i}(\mathbf{x})$, $i = 0, 1$. The convected velocity $\tilde{\mathbf{v}}^{n-i}(\mathbf{x})$ and the void fraction $\tilde{\Phi}^{n-i}$ are interpolated in the same fashion. A key step in the above algorithm is to locate the foot of the characteristics within the finite element grid. The element-searching algorithm is described in detail in Minev *et al.* [129].

Before discretizing (4.8) and (4.9) we first introduce the notations

$$\begin{aligned} f_1(\mathbf{u}, \mathbf{v}, \Phi) = &-\frac{1}{Fr}\frac{\Phi}{1-\alpha}(0,0,1) - \Big(\frac{1}{Fr}\frac{1}{\alpha}\frac{r_d}{l}(1-\Phi)H^{\frac{1}{2}}(\Phi) \\ &+ \frac{\partial\{\Phi(\alpha+\mu(\Phi))H(\Phi)(1-\Phi)^4\}}{\partial\Phi}\frac{(1-\Phi)}{\alpha(1-\Phi_0)^2}\Big)\nabla\Phi - \frac{1}{Fr}\frac{1}{\alpha}(1-\Phi_0)\Phi(\mathbf{v}-\mathbf{u}) \end{aligned} \tag{4.13}$$

and

$$\begin{aligned} f_2(u, v, \Phi) = &(\frac{1}{Fr}\frac{r_d}{l}(1-\Phi)H^{\frac{1}{2}}(\Phi) + \frac{\partial\{\Phi(\alpha+\mu(\Phi))H(\Phi)(1-\Phi)^4\}}{\partial\Phi}\frac{(1-\Phi)}{(1-\Phi_0)^2})\nabla\Phi \\ &+ \frac{1}{Fr}(1-\Phi_0)\Phi(\mathbf{v}-\mathbf{u}) - \frac{1}{Fr}\frac{1-\Phi}{1-\alpha}(0,0,1) \end{aligned} \tag{4.14}$$

Then, the convective terms are split from the momentum equations (4.8) and (4.9) to obtain the following (split) approximation of the original system

$$\begin{aligned} &\Phi^{n+1}\frac{3\mathbf{v}^{n+1} - 4\tilde{\mathbf{v}}^n + \tilde{\mathbf{v}}^{n-1}}{2\Delta t} = -\frac{1}{\alpha}\Phi^{n+1}\nabla p^{n+1} + f_1(\mathbf{u}^{n+1}, \mathbf{v}^{n+1}, \Phi^{n+1}) \\ &- \frac{1}{\alpha}\Phi^{n+1}\mu(\Phi^{n+1})\Big(\frac{3\mathbf{v}^{n+1} - 4\tilde{\mathbf{v}}^n + \tilde{\mathbf{v}}^{n-1}}{2\Delta t} - \frac{3\mathbf{u}^{n+1} - 4\tilde{\mathbf{u}}^n + \tilde{\mathbf{u}}^{n-1}}{2\Delta t}\Big) \\ &+ \frac{r_d}{l}\nabla\cdot((\Phi^{n+1}(1+\frac{1}{\alpha}\mu(\Phi^{n+1}))\frac{(1-\Phi^{n+1})^2}{1-\Phi_0}H^{\frac{1}{2}}(\Phi^{n+1}))\nabla\mathbf{v}^{n+1}) \end{aligned} \tag{4.15}$$

and

$$(1-\Phi^{n+1})\frac{3\mathbf{u}^{n+1}-4\tilde{\mathbf{u}}^{n}+\tilde{\mathbf{u}}^{n-1}}{2\Delta t}=-(1-\Phi^{n+1})\nabla p^{n+1}+f_2(\mathbf{u}^{n+1},\mathbf{v}^{n+1},\Phi^{n+1})+$$

$$\Phi^{n+1}\mu(\Phi^{n+1})\left(\frac{3\mathbf{v}^{n+1}-4\tilde{\mathbf{v}}^{n}+\tilde{\mathbf{v}}^{n-1}}{2\Delta t}-\frac{3\mathbf{u}^{n+1}-4\tilde{\mathbf{u}}^{n}+\tilde{\mathbf{u}}^{n-1}}{2\Delta t}\right) \tag{4.16}$$

In order to satisfy the mass conservation, the advected void fractions $\tilde{\Phi}^{n-i}(i=0,1)$ are corrected according to

$$\{3+2\Delta t[\nabla\cdot(2\mathbf{v}^{n}-\mathbf{v}^{n-1})]\}\Phi^{n+1}=4\tilde{\Phi}^{n}-\tilde{\Phi}^{n-1} \tag{4.17}$$

This equation is the time discrete form of (4.6), where a second order backward difference is used to discretize the time derivative, and $\mathbf{v}^{n+1}$ is extrapolated using the second order extrapolation $2\mathbf{v}^{n}-\mathbf{v}^{n-1}$. This is a fully explicit scheme for the void fraction, which, due to the method of characteristics has good stability properties.

(ii) Pressure and velocities prediction sub-step

(a) Pressure prediction

We use p^{n} as a predictor for p^{n+1}, i.e., $p_p^{n+1}=p^{n}$.

(b) Velocity prediction

As it is usually done in the incremental pressure correction schemes, the velocity predictions $\mathbf{u}_p^{n+1}$ and $\mathbf{v}_p^{n+1}$ are determined from the following set of momentum equations

$$\begin{aligned}\Phi^{n+1}\frac{3\mathbf{v}_p^{n+1}-4\tilde{\mathbf{v}}^{n}+\tilde{\mathbf{v}}^{n-1}}{2\Delta t}&=-\frac{1}{\alpha}\Phi^{n+1}\nabla p^{n}+f_1(\mathbf{u}_p^{n+1},\mathbf{v}_p^{n+1},\Phi^{n+1})\\&-\frac{1}{\alpha}\Phi^{n+1}\mu(\Phi^{n+1})\left(\frac{3\mathbf{v}_p^{n+1}-4\tilde{\mathbf{v}}^{n}+\tilde{\mathbf{v}}^{n-1}}{2\Delta t}-\frac{3\mathbf{u}_p^{n+1}-4\tilde{\mathbf{u}}^{n}+\tilde{\mathbf{u}}^{n-1}}{2\Delta t}\right)\\&+\frac{r_d}{l}\nabla\cdot\left(\Phi^{n+1}(1+\frac{1}{\alpha}\mu(\Phi^{n+1}))\frac{(1-\Phi^{n+1})^2}{1-\Phi_0}H^{\frac{1}{2}}(\Phi^{n+1}))\nabla\mathbf{v}_p^{n+1}\right)\end{aligned} \tag{4.18}$$

$$\begin{aligned}(1-\Phi^{n+1})\frac{3\mathbf{u}_p^{n+1}-4\tilde{\mathbf{u}}^{n}+\tilde{\mathbf{u}}^{n-1}}{2\Delta t}&=f_2(\mathbf{u}_p^{n+1},\mathbf{v}_p^{n+1},\Phi^{n+1})\\-(1-\Phi^{n+1})\nabla p^{n}+\Phi^{n+1}\mu(\Phi^{n+1})&\left(\frac{3\mathbf{v}_p^{n+1}-4\tilde{\mathbf{v}}^{n}+\tilde{\mathbf{v}}^{n-1}}{2\Delta t}-\frac{3\mathbf{u}_p^{n+1}-4\tilde{\mathbf{u}}^{n}+\tilde{\mathbf{u}}^{n-1}}{2\Delta t}\right)\end{aligned} \tag{4.19}$$

(iii) Pressure and velocities correction sub-step

(a) Pressure correction

Subtracting (4.18) from (4.15), (4.19) from (4.16), and neglecting the difference between

the two second order terms, we obtain

$$\Phi^{n+1}\frac{3}{2}\left(\frac{\mathbf{v}^{n+1}-\mathbf{v}_p^{n+1}}{\Delta t}\right) = -\frac{1}{\alpha}\Phi^{n+1}(\nabla p^{n+1}-\nabla p^n)$$
$$-\frac{1}{\alpha}\Phi^{n+1}\mu(\Phi^{n+1})\frac{3}{2}\left(\frac{\mathbf{v}^{n+1}-\mathbf{v}_p^{n+1}}{\Delta t}-\frac{\mathbf{u}^{n+1}-\mathbf{u}_p^{n+1}}{\Delta t}\right) \tag{4.20}$$
$$+f_1(\mathbf{u}^{n+1},\mathbf{v}^{n+1},\Phi^{n+1})-f_1(\mathbf{u}_p^{n+1},\mathbf{v}_p^{n+1},\Phi^{n+1})$$

$$(1-\Phi^{n+1})\frac{3}{2}\left(\frac{\mathbf{u}^{n+1}-\mathbf{u}_p^{n+1}}{\Delta t}\right) = -(1-\Phi^{n+1})(\nabla p^{n+1}-\nabla p^n)$$
$$+\Phi^{n+1}\mu(\Phi^{n+1})\frac{3}{2}\left(\frac{\mathbf{v}^{n+1}-\mathbf{v}_p^{n+1}}{\Delta t}-\frac{\mathbf{u}^{n+1}-\mathbf{u}_p^{n+1}}{\Delta t}\right) \tag{4.21}$$
$$+f_2(\mathbf{u}^{n+1},\mathbf{v}^{n+1},\Phi^{n+1})-f_2(\mathbf{u}_p^{n+1},\mathbf{v}_p^{n+1},\Phi^{n+1})$$

In order to close the system, we first combine both continuity equations and derive a continuity equation for the averaged velocity that will be used to correct the pressure

$$\nabla\cdot(\rho_2\Phi\mathbf{v}+\rho_1(1-\Phi)\mathbf{u}) = (\rho_1-\rho_2)\frac{\partial\Phi}{\partial t} \tag{4.22}$$

Summing up (4.20) and (4.21), taking the divergence of the resulting equation, and using the discrete form of (4.22) we obtain the correction equation for the pressure

$$\frac{3}{2}(\rho_1-\rho_2)\left(\frac{3\Phi^{n+1}-4\Phi^n+\Phi^{n-1}}{2\Delta t}\right) = -\Delta t\rho_1\nabla\cdot(\nabla p^{n+1}-\nabla p^n) \tag{4.23}$$
$$\frac{3}{2}\nabla\cdot(\Phi^{n+1}\rho_2\mathbf{v}_p^{n+1}+(1-\Phi^{n+1})\rho_1\mathbf{u}_p^{n+1})$$

Note that all the time derivatives in (4.22) are approximated by means of second order backward differences.

(b) Velocities correction

Finally, $\mathbf{u}^{n+1}$,$\mathbf{v}^{n+1}$ are obtained from (4.20) and (4.21).

The equations (4.18)-(4.21) and (4.23) are discretized by means of P_2-P_1 tetrahedral finite elements starting from the usual Galerkin formulations.

The original system (4.1)-(4.4) is clearly advection-dominated and the numerical results show that the method of characteristics (as implemented here) does not provide enough stability for the numerical algorithm. Therefore a stabilization mechanism is introduced, which is based on a hierarchical two-level decomposition of the approximation space as proposed by Guermond [79].

Let us consider two nested grids of sizes H and h, where $H = 2h$ (see Fig. 4.1), which generate corresponding finite element functional spaces denoted by $(\mathbf{X}_H)$ and $(\mathbf{X}_h)$. The basis

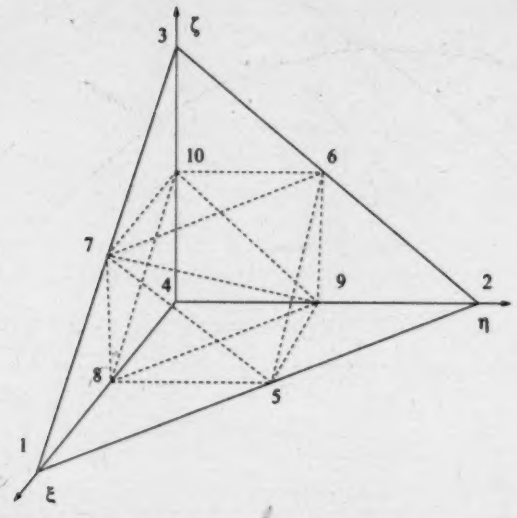

Figure 4.1: Tetrahedral element in local coordinate system, with axes (ξ,η,ζ)

for the difference space $\mathbf{X}_h^H$, based on the decomposition $\mathbf{X}_h = \mathbf{X}_H \oplus \mathbf{X}_h^H$, is given by:

$$(\varphi_h^H)_i = \begin{cases} \varphi_{h,i}\,, & \text{if } i \in \tau_h - \tau_H \\ \varphi_{h,i} - \varphi_{H,i}\,, & \text{if } i \in \tau_H \end{cases} \tag{4.24}$$

For an easy implementation, $\mathbf{X}_H$ is injected into $\mathbf{X}_h$, using the representation of the basis functions:

$$\varphi_H^k = \sum_{j=1}^{35} a_j^k \varphi_h^j \tag{4.25}$$

In order to find a_j^k, we solve the following systems

$$\langle \varphi_H^k, \varphi_h^i \rangle = \sum_{j=1}^{35} a_j^k \langle \varphi_h^j, \varphi_h^i \rangle \quad i,j = 1,...,35, \quad k = 1,...,10 \tag{4.26}$$

The weak formulations for any of (4.18)-(4.21) can be written as

$$\text{Find } \mathbf{u}_h \in \mathbf{X}_h \text{ s.t. } a(\mathbf{u}_h, \mathbf{v}_h) = (\mathbf{f}, \mathbf{v}_h), \quad \forall \mathbf{v}_h \in \mathbf{X}_h \tag{4.27}$$

with $a(\mathbf{u}_h, \mathbf{v}_h)$ being the bilinear form generated by the implicit terms and $(\mathbf{f}, \mathbf{v}_h)$ being the linear functional generated by the explicitly known terms. Then the stabilized problem is given by

$$\text{Find } \mathbf{u}_h \in \mathbf{X}_h \text{ s.t. } a(\mathbf{u}_h, \mathbf{v}_h) + b_h(\mathbf{u}_h^H, \mathbf{v}_h^H) = (\mathbf{f}, \mathbf{v}_h), \quad \forall \mathbf{v}_h \in \mathbf{X}_h \tag{4.28}$$

where the bilinear form $b_h(\mathbf{u}_h^H, \mathbf{v}_h^H) : \mathbf{X}_h^H \times \mathbf{X}_h^H \to \mathbf{R}$ is defined as:

$$b_h(\mathbf{u}_h^H, \mathbf{v}_h^H) = c_b \sum_{\mathbf{K}_h \in \tau_h} \text{meas}(\mathbf{K}_h)^{1/3} \int_{\mathbf{K}_h} (\nabla \mathbf{u}_h^H \cdot \nabla \mathbf{v}_h^H). \tag{4.29}$$

For more details see Guermond [79].

In many practical problems, the solution may happen to become close to singular at some points. This is a typical phenomenon for first-order non-linear hyperbolic equations that destabilizes the numerical scheme. The usual way to deal with it is to introduce a shock capturing mechanism (see Guermond [79]). In the stabilization technique, the shock capturing term c_h is

$$c_h(\mathbf{u}_h^H, \mathbf{v}_h, \mathbf{w}_h) = c_{sc} \sum_{\mathbf{K}_H \in \tau_H} \text{meas}(\mathbf{K}_H)^{1/3} \frac{||\nabla \mathbf{u}_h^H||_{0,\mathbf{K}_H}}{||\nabla \mathbf{u}_h||_{0,\mathbf{K}_H}} \int_{\mathbf{K}_H} (\nabla \mathbf{v}_h \cdot \nabla \mathbf{w}_h) \tag{4.30}$$

The modified problem reads

$$\text{Find } \mathbf{u}_h \in \mathbf{X}_h \text{ s.t. } a(\mathbf{u}_h, \mathbf{v}_h) + b_h(\mathbf{u}_h^H, \mathbf{v}_h^H) + c_h(\mathbf{u}_h^H, \mathbf{u}_h, \mathbf{v}_h) = (\mathbf{f}, \mathbf{v}_h), \quad \forall \mathbf{v}_h \in \mathbf{X}_h. \tag{4.31}$$

The idea behind this technique is similar to the functional decomposition usually done in the multi-grid methods.

As a conclusion, let us summarize the numerical scheme.

(i) First, the convective terms $\tilde{\Phi}^{n-i}$, $\tilde{\mathbf{v}}^{n-i}$ and $\tilde{\mathbf{u}}^{n-i}$, $n = 1, 2$, $i = 0, 1$, are split and resolved by the method of characteristics. We use a stabilized finite element method to discretize (4.17) with the implicit stabilization. This requires the solving of a linear system and may seem unnecessary at first glance. But the resulting linear system is well conditioned and does not pose a computational challenge and the implicitly stabilized problem has better stability properties. Of course, this step can also be performed fully explicitly.

(ii) Next, we compute predictions to $\mathbf{u}^{n+1}$ and $\mathbf{v}^{n+1}$, denoted by $\mathbf{u}_p^{n+1}$ and $\mathbf{v}_p^{n+1}$, from the equations (4.18) and (4.19), using p^n as a prediction for p^{n+1}.

(iii) Then, we update the pressure using (4.22), which is derived from combining the continuity equations for the two phases. The equation that yields the corrected pressure p^{n+1} is the discrete form of (4.23).

(iv) Finally, we use (4.20) and (4.21) to compute the velocity correctors $\mathbf{u}^{n+1}$ and $\mathbf{v}^{n+1}$. Our approach yields fully symmetric matrices for both velocity and pressure subproblems, which are solved by a conjugate gradient method.

4.2 Details about the implementation of the numerical scheme

We will show in detail how the finite element method and its sub-grid stabilized version were implemented on equation (4.17). The same method was applied for the discretization of the momentum equations (4.18), (4.19), (4.20), (4.21) and the pressure equation (4.23). Since, except for a more complicated writing, the method follows the same idea,we will present only the final matrix form for the other equations.

After splitting the convective part from the equation (4.6) and solving it using the method of characteristics, the part of the equation that is discretized and solved using the finite element method is:

$$\frac{\partial \Phi}{\partial t} + \Phi \nabla \cdot \mathbf{v} = 0 \tag{4.32}$$

Since we consider different initial and boundary conditions throughout the thesis, they are omitted here. However, in practice, their contributions are carefully considered.

Our domain Ω throughout the simulations is either a cylinder or a paralellipiped, therefore it is a convex and bounded set. Using the standard finite element method, we construct a triangulation for our domain, denoted by $\mathcal{T}_H$, composed of quasi-uniform affine simplices K_H (for the three-dimensional case the elements are tetrahedrons). We mentioned earlier that we use P2-P1 tetrahedrons. That means that we defined piecewise quadratic finite element spaces on $\mathcal{T}_H$ for the void fraction Φ and for the velocity fields $\mathbf{u}$ and $\mathbf{v}$ and we defined a piecewise linear finite element space on $\mathcal{T}_H$ for the pressure. The reason we use different order finite element spaces is to avoid spurious oscillations. We write this formally for the void fraction only.

$$X_H = \{\Phi_H \in H^1(\Omega); \quad \Phi_{H|K_H} \in P_1(K_H), \quad \forall K_H \in \mathcal{T}_H\} \tag{4.33}$$

The semi-discrete finite element formulation reads:

$$\text{Find } \mathbf{\Phi}_H(t) \in \mathbf{X}_H \text{ s.t. } (\frac{\partial \Phi_H}{\partial t}(t), w_H) + (\nabla \cdot \mathbf{v}_H \Phi_H(t), w_H) = 0, \quad \forall w_H \in \mathbf{X}_H \tag{4.34}$$

We construct an orthogonal basis $\{\phi_i\}_{i=1}^{i=N}$ on X_H where N stands for the number of total nodes such that:

$$\varphi_i(\mathbf{x}_j) = \delta_{ij} \quad \text{for i, j any of the vortices or mid-points of any tetrahedral element of the discrete domain.} \tag{4.35}$$

Therefore, $X_H = \text{span}\{\varphi_i\}_{i=1}^{i=N}$ and

$$\Phi_H(\mathbf{x}, t) = \sum_{i=1}^{N} \Phi_H(\mathbf{x}_i, t)\varphi_i(\mathbf{x}) = \sum_{i=1}^{N} \Phi_i(t)\varphi_i(\mathbf{x}) \tag{4.36}$$

Inserting the above representation (4.36) into (4.34) and replacing w_H by $\varphi_j(\mathbf{x})$, $j = \overline{1,N}$ we obtain:

$$\text{Find } \Phi_i(t) \text{ s.t.} \quad \forall j = \overline{1,N}$$

$$\sum_{i=1}^{N}\left(\int_\Omega \varphi_i(\mathbf{x})\varphi_j(\mathbf{x})d\mathbf{x}\right)\frac{\partial \Phi_i}{\partial t}(t) + \sum_{i=1}^{N}\left(\int_\Omega (\nabla \cdot \mathbf{v_H})\varphi_i(\mathbf{x})\varphi_j(\mathbf{x})d\mathbf{x}\right)\Phi_i(t) = 0 \tag{4.37}$$

If the fully discrete finite element case is considered,

$$\Phi_H^n(\mathbf{x}) = \sum_{i=1}^{N}\Phi_H(\mathbf{x}_i, t^n)\varphi_i(\mathbf{x}) = \sum_{i=1}^{N}\Phi_i^n\varphi_i(\mathbf{x}) \tag{4.38}$$

by inserting (4.38) into (4.17), by multiplying the whole equation by w_H and integrating over Ω and finally, by replacing w_H by $\varphi_j(\mathbf{x})$, $j = \overline{1,N}$ we obtain:

$$\sum_{i=1}^{N}\left(\int_\Omega \{3 + 2\Delta t[\nabla \cdot (2\mathbf{v}^n - \mathbf{v}^{n-1})]\}\varphi_i(\mathbf{x})\varphi_j(\mathbf{x})d\mathbf{x}\right)\Phi_i^{n+1} = \sum_{i=1}^{N}\left(\int_\Omega \varphi_i(\mathbf{x})\varphi_j(\mathbf{x})d\mathbf{x}\right)\left(4\tilde{\Phi}_i^n - \tilde{\Phi}_i^{n-1}\right) \tag{4.39}$$

or,

$$M_{vf}\Phi^{n+1} = M(4\tilde{\Phi}^n - \tilde{\Phi}^{n-1}) \tag{4.40}$$

where we made the following notations:

$$\begin{aligned}
(M_{vf})_{ij} &= \int_\Omega \{3 + 2\Delta t[\nabla \cdot (2\mathbf{v}^n - \mathbf{v}^{n-1})]\}\varphi_i(\mathbf{x})\varphi_j(\mathbf{x})d\mathbf{x} \\
M_{ij} &= \int_\Omega \varphi_i(\mathbf{x})\varphi_j(\mathbf{x})d\mathbf{x} \\
\Phi^{n+1} &= (\Phi_1^{n+1}, ..., \Phi_N^{n+1})^T \\
\mathbf{v}^m &= (\mathbf{v}_1^m, ..., \mathbf{v}_N^m)^T, \text{ where } m = n, n+1
\end{aligned} \tag{4.41}$$

In order to compute any of the above integrals, we create an affine mapping between the reference simplex (tetrahedron), denoted by $\hat{K}$ and any of the elements that compose the physical space K_H. It has the form: $T_{KH} : \hat{K} -> K_H$,

$$T_{K_H}(\xi, \eta, \zeta) = \sum_{j=1}^{10} x_{i,j}\varphi_j(\xi, \eta, \zeta) = x_i \tag{4.42}$$

where $(x_1, x_2, x_3) = (x, y, z)$ and $(\xi_1, \xi_2, \xi_3) = (\xi, \eta, \zeta)$. Notice that $\varphi_j(\xi, \eta, \zeta)$ is not the same with $\varphi_j(\mathbf{x})$ even though they are denoted the same way. The distinction is clear from the context. The elemental quadratic shape functions in local co-ordinates (ξ, η, ζ) are:

$$\varphi_1 = \xi(2\xi - 1) \tag{4.43}$$

$$\varphi_2 = \zeta(2\zeta - 1) \tag{4.44}$$

$$\varphi_3 = \eta(2\eta - 1) \tag{4.45}$$

$$\varphi_4 = (1 - (\xi + \eta + \zeta))(1 - 2(\xi + \eta + \zeta)) \tag{4.46}$$

$$\varphi_5 = 4\xi\zeta \tag{4.47}$$

$$\varphi_6 = 4\eta\zeta \tag{4.48}$$

$$\varphi_7 = 4\xi\eta \tag{4.49}$$

$$\varphi_8 = 4\xi(1 - (\xi + \eta + \zeta)) \tag{4.50}$$

$$\varphi_9 = 4\zeta(1 - (\xi + \eta + \zeta)) \tag{4.51}$$

$$\varphi_{10} = 4\eta(1 - (\xi + \eta + \zeta)) \tag{4.52}$$

The Jacobian matrix for the co-ordinate transformation $\frac{\partial(x,y,z)}{\partial(\xi,\eta,\zeta)}$, according to (4.42) is given by:

$$J_{i,j} = \frac{\partial x_j}{\partial \xi_i} = \sum_{k=1}^{10} x_{j,k} \frac{\partial \varphi_k}{\partial \xi_i} \tag{4.53}$$

The elemental pressure shape functions are the only ones that are first order polynomials in (ξ, η, ζ). They have the form:

$$\psi_1 = \xi \tag{4.54}$$

$$\psi_2 = \zeta \tag{4.55}$$

$$\psi_3 = \eta \tag{4.56}$$

$$\psi_4 = 1 - (\xi + \eta + \zeta) \tag{4.57}$$

Let us illustrate how the integral M_{vf} was computed. To do so, we construct a connectivity table that creates the correspondence between the local numbering and the global numbering. For instance, as we go through the elements of the domain, conTable[element][localnode]=globalnode where localnode=$\overline{1,10}$ since each tetrahedron has four vortices and six mid-points and globalnode=$\overline{1,N}$.

$$
\begin{aligned}
(M_{vf})_{ij} &= \int_{\Omega} \{3 + 2\Delta t[\nabla \cdot (2\mathbf{v}^n - \mathbf{v}^{n-1})]\}\varphi_i(\mathbf{x})\varphi_j(\mathbf{x})d\mathbf{x} \\
&= \sum_{K_H \in \mathcal{T}_H} \int_{K_H} \{3 + 2\Delta t[\nabla \cdot (2\mathbf{v}^n - \mathbf{v}^{n-1})]\}\varphi_i(\mathbf{x})\varphi_j(\mathbf{x})d\mathbf{x} \\
&= \sum_{K_H \in \mathcal{T}_H} \int_{\hat{K}} \{3 + 2\Delta t[\nabla \cdot (2\mathbf{v}^n - \mathbf{v}^{n-1})](\xi)\}\varphi_{i'}(\xi)\varphi_{j'}(\xi)\frac{d\mathbf{x}}{d\xi}d\xi \\
&= \sum_{K_H \in \mathcal{T}_H} \sum_{p=1}^{ngp} \{3 + 2\Delta t[\nabla \cdot (2\mathbf{v}^n - \mathbf{v}^{n-1})](\xi_p)\}\varphi_{i'}(\xi_p)\varphi_{j'}(\xi_p)|J(\xi_p)|w_p
\end{aligned}
\tag{4.58}
$$

i' and j' are the local nodes corresponding to the global nodes i and j of the element K_H (conTable[K_H][i']=i,conTable[K_H][j']=j). They are simply computed by inverting the connectivity table. ξ_p and w_p stand for the Gaussian integration points and Gaussian weighting factors. All the integrals are computed using at least 5th order Gaussian quadrature. In general, a n-th order Gaussian quadrature will exactly integrate a polynomial of degree 2n-1. The Gauss points and weights can be found in Keast [108]. The idea behind computing the integrals over the whole domain can be summarized easily like this: first we compute all the integrals locally and then we assemble them to the global matrix with the help of the connectivity table. In the above illustration:

$$
\frac{\partial v_1^n}{\partial x}(\xi_p) = \sum_{l=1}^{10} v_{1l}^n \frac{\partial \varphi_l}{\partial x}(\xi_p) = \sum_{l=1}^{10} v_{1l}^n \frac{\partial \varphi_l}{\partial \xi}(\xi_p)\frac{\partial \xi}{\partial x}(\xi_p) = \sum_{l=1}^{10} v_{1l}^n \frac{\partial \varphi_l}{\partial \xi}(\xi_p) J_{1,1}^{-1}(\xi_p)
\tag{4.59}
$$

where v_1^n stands for the x component of $\mathbf{v}^n$. In the above example the velocity was locally interpolated and $\frac{\partial \varphi_l}{\partial \xi}$ can be computed by taking the derivatives of the elemental quadratic shape functions (4.43)-(4.52).

So far, we presented the standard finite element procedure and its implementation. According to our empirical experience and to Guermond's findings (see [80]) the Galerkin technique is not optimal for approximating first order PDE's. The conclusion can be generalized even to the case of second order PDE's, when the magnitude of the second order differential operator is too small, meaning that the coercivity of the second order operator is not strong enough to guarantee the Galerkin technique to work well. Guermond ([80]) proposes a simple cure to this problem that consists of enlarging the space of the test functions. Basically, instead of building one finite element space X_H, he builds two finite element spaces, denoted with

X_H and X_h where $c_1 h \leq H \leq c_2 h$. In practice $h = \frac{H}{2}$. In other words, each macro-element (the tetrahedrons in which X_H was decomposed into) was divided into eight sub-elements (the tetrahedrons that were composing X_h).

$$X_H = \{\Phi_H \in H^1(\Omega); \quad \Phi_{H|K_H} \in P_1(K_H), \quad \forall K_H \in \mathcal{T}_H\} \tag{4.60}$$

$$X_h = \{\Phi_h \in H^1(\Omega); \quad \Phi_{h|K_h} \in P_1(K_h), \quad \forall K_h \in \mathcal{T}_h\} \tag{4.61}$$

Because the Galerkin formulation offered no a priori control on $u_h - u_H$, one simple way to do so is to to introduce a coercive bilinear form acting only on $u_h - u_H$ and small enough to spoil the consistency. It is based on the following decomposition:

$$\mathbf{X}_h = \mathbf{X}_H \oplus \mathbf{X}_h^H \tag{4.62}$$

where

$$X_h^H = \{\Phi_h^H \in H^1(\Omega);\ \Phi_{h|K_H}^H \in P,\ \forall K_H \in \mathcal{T}_H\} \tag{4.63}$$

with P being defined as the space of functions that are continuous on K_H, vanish at the vortices of K_H and are piecewise P_2 on each sub-tetrahedron of K_H. As mentioned earlier, the basis for the difference space X_h^H and the way it was implemented is given by (4.24), (4.25) and (4.26). After the computation of the matrices in (4.26) is carried over and the basis of the macro-tetrahedron is expressed in terms of the bases of the micro-tetrahedrons, the following expressions were obtained using MAPLE (the numbering is according to Fig. (4.2)).

$$\begin{aligned}\varphi_H^1 = \varphi_h^1 &+ \frac{3}{8}\varphi_h^{11} - \frac{1}{8}\varphi_h^{12} - \frac{1}{8}\varphi_h^{15} + \frac{3}{8}\varphi_h^{16} + \frac{3}{8}\varphi_h^{17} - \frac{1}{8}\varphi_h^{18} - \frac{1}{8}\varphi_h^{27} - \frac{1}{8}\varphi_h^{28} - \frac{1}{8}\varphi_h^{29} \\ &- \frac{1}{8}\varphi_h^{30} - \frac{1}{8}\varphi_h^{32} - \frac{1}{8}\varphi_h^{33} - \frac{1}{8}\varphi_h^{35}\end{aligned} \tag{4.64}$$

Since $(\varphi_h^H)_1 = \varphi_h^1 - \varphi_H^1$,

$$\begin{aligned}(\varphi_h^H)^1 = &-\frac{3}{8}\varphi_h^{11} + \frac{1}{8}\varphi_h^{12} + \frac{1}{8}\varphi_h^{15} - \frac{3}{8}\varphi_h^{16} - \frac{3}{8}\varphi_h^{17} + \frac{1}{8}\varphi_h^{18} + \frac{1}{8}\varphi_h^{27} + \frac{1}{8}\varphi_h^{28} + \frac{1}{8}\varphi_h^{29} \\ &+ \frac{1}{8}\varphi_h^{30} + \frac{1}{8}\varphi_h^{32} + \frac{1}{8}\varphi_h^{33} + \frac{1}{8}\varphi_h^{35}\end{aligned} \tag{4.65}$$

In the same way,

$$\begin{aligned}(\varphi_h^H)^2 = &\frac{1}{8}\varphi_h^{11} - \frac{3}{8}\varphi_h^{12} - \frac{3}{8}\varphi_h^{13} + \frac{1}{8}\varphi_h^{14} + \frac{3}{8}\varphi_h^{19} - \frac{1}{8}\varphi_h^{20} - \frac{1}{8}\varphi_h^{23} + \frac{1}{8}\varphi_h^{24} + \frac{1}{8}\varphi_h^{30} \\ &+ \frac{1}{8}\varphi_h^{31} + \frac{1}{8}\varphi_h^{33} + \frac{1}{8}\varphi_h^{34} + \frac{1}{8}\varphi_h^{35}\end{aligned} \tag{4.66}$$

$$(\varphi_h^H)^3 = \frac{1}{8}\varphi_h^{13} - \frac{3}{8}\varphi_h^{14} - \frac{3}{8}\varphi_h^{15} + \frac{1}{8}\varphi_h^{16} - \frac{3}{8}\varphi_h^{21} + \frac{1}{8}\varphi_h^{22} + \frac{1}{8}\varphi_h^{24} + \frac{1}{8}\varphi_h^{25} + \frac{1}{8}\varphi_h^{26} + \frac{1}{8}\varphi_h^{27} + \frac{1}{8}\varphi_h^{32} + \frac{1}{8}\varphi_h^{34} + \frac{1}{8}\varphi_h^{35} \tag{4.67}$$

$$(\varphi_h^H)^4 = \frac{1}{8}\varphi_h^{17} - \frac{3}{8}\varphi_h^{18} + \frac{1}{8}\varphi_h^{19} - \frac{3}{8}\varphi_h^{20} + \frac{1}{8}\varphi_h^{21} - \frac{3}{8}\varphi_h^{22} + \frac{1}{8}\varphi_h^{23} + \frac{1}{8}\varphi_h^{25} + \frac{1}{8}\varphi_h^{26} + \frac{1}{8}\varphi_h^{28} + \frac{1}{8}\varphi_h^{29} + \frac{1}{8}\varphi_h^{31} + \frac{1}{8}\varphi_h^{35} \tag{4.68}$$

$$(\varphi_h^H)^5 = -\frac{3}{4}\varphi_h^{11} - \frac{3}{4}\varphi_h^{12} - \frac{1}{2}\varphi_h^{23} - \frac{1}{2}\varphi_h^{24} - \frac{1}{2}\varphi_h^{27} - \frac{1}{2}\varphi_h^{28} - \frac{1}{4}\varphi_h^{30} - \frac{1}{4}\varphi_h^{33} - \frac{1}{4}\varphi_h^{35} \tag{4.69}$$

$$(\varphi_h^H)^6 = -\frac{3}{4}\varphi_h^{13} - \frac{3}{4}\varphi_h^{14} - \frac{1}{4}\varphi_h^{24} - \frac{1}{2}\varphi_h^{26} - \frac{1}{2}\varphi_h^{27} - \frac{1}{2}\varphi_h^{30} - \frac{1}{2}\varphi_h^{31} - \frac{1}{4}\varphi_h^{34} - \frac{1}{4}\varphi_h^{35} \tag{4.70}$$

$$(\varphi_h^H)^7 = -\frac{3}{4}\varphi_h^{15} - \frac{3}{4}\varphi_h^{16} - \frac{1}{2}\varphi_h^{24} - \frac{1}{2}\varphi_h^{25} - \frac{1}{4}\varphi_h^{27} - \frac{1}{2}\varphi_h^{29} - \frac{1}{2}\varphi_h^{30} - \frac{1}{4}\varphi_h^{32} - \frac{1}{4}\varphi_h^{35} \tag{4.71}$$

$$(\varphi_h^H)^8 = -\frac{3}{4}\varphi_h^{17} - \frac{3}{4}\varphi_h^{18} - \frac{1}{2}\varphi_h^{23} - \frac{1}{2}\varphi_h^{25} - \frac{1}{4}\varphi_h^{28} - \frac{1}{4}\varphi_h^{29} - \frac{1}{2}\varphi_h^{32} - \frac{1}{2}\varphi_h^{33} - \frac{1}{4}\varphi_h^{35} \tag{4.72}$$

$$(\varphi_h^H)^9 = -\frac{3}{4}\varphi_h^{19} - \frac{3}{4}\varphi_h^{20} - \frac{1}{4}\varphi_h^{23} - \frac{1}{2}\varphi_h^{26} - \frac{1}{2}\varphi_h^{28} - \frac{1}{4}\varphi_h^{31} - \frac{1}{2}\varphi_h^{33} - \frac{1}{2}\varphi_h^{34} - \frac{1}{4}\varphi_h^{35} \tag{4.73}$$

$$(\varphi_h^H)^{10} = -\frac{3}{4}\varphi_h^{21} - \frac{3}{4}\varphi_h^{22} - \frac{1}{4}\varphi_h^{25} - \frac{1}{4}\varphi_h^{26} - \frac{1}{2}\varphi_h^{29} - \frac{1}{2}\varphi_h^{31} - \frac{1}{2}\varphi_h^{32} - \frac{1}{2}\varphi_h^{34} - \frac{1}{4}\varphi_h^{35} \tag{4.74}$$

In order to implement the above idea in our C code, a local connectivity table that gives the correspondence between the numbering of the standard macro-element(35 nodes) and the numbering of each sub-tetrahedron (8 subtetrahedrons, each having 10 nodes) had to be created. For instance:

$$CT[1][1] = 1,\ CT[1][2] = 11,\ CT[1][3] = 5,\ CT[1][4] = 24,\ CT[1][5] = 7,$$

$$CT[1][6] = 16,\ CT[1][7] = 17,\ CT[1][8] = 23,\ CT[1][9] = 25,\ CT[1][10] = 8$$

where the first argument of CT represents one of the eight sub-tetrahedrons and the second argument represent the local numbering of each sub-tetrahedrons (vortices and mid-points). This correspondence is done according to Fig. 4.2. Also all the formulas (4.65)-(4.74) had to be localized/projected on every sub-element. For instance, if we take a look at φ_H^1 in (4.65) and we are interested on writing it only with respect to the first sub-element (with vortices 1, 5, 8 and 7) we see that, except for φ_h^{11}, φ_h^{16} and φ_h^{17}, all the other shape functions have no

contribution since their support is outside the sub-element. Therefore, (4.65) localized on the first sub-element has the form:

$$(\varphi_h^H)_1^1 = -\frac{3}{8}\varphi_h^{11} - \frac{3}{8}\varphi_h^{16} - \frac{3}{8}\varphi_h^{17} \tag{4.75}$$

or, in the sub-tetrahedrons local notations:

$$(\varphi_h^H)_1^1 = -\frac{3}{8}\varphi_h^{2} - \frac{3}{8}\varphi_h^{6} - \frac{3}{8}\varphi_h^{7} \tag{4.76}$$

In the same way any of (4.65)-(4.74) can be localized on each sub-tetrahedron. Therefore, the localized version of (4.25) becomes:

$$(\varphi_H^h)_{el}^k = \sum_{j=1}^{10} a_{j,el}^k \, \varphi_h^j \quad \text{for } k = 1..10, \ el = 1..8 \tag{4.77}$$

The semi-discrete sub-grid-stabilized version of the finite element formulation reads:

$$\begin{aligned} &\text{Find } \Phi_h(t) \in \mathbf{X}_h \text{ s.t. } (\frac{\partial \Phi_h}{\partial t}(t), w_h) + (\nabla \cdot \mathbf{v}_h \Phi_h(t), w_h) \\ &+ b_h(\Phi_h^H(t), w_h^H) + c_h(\Phi_h^H(t), \Phi_h(t), w_h) = 0, \quad \forall w_h \in \mathbf{X}_h \end{aligned} \tag{4.78}$$

$\{\varphi_i\}_{i=1}^N$ is a basis on X_h and $\{(\varphi_h^H)_i\}_{i=1}^N$ is a basis on X_h^H. Therefore,

$$\Phi_h(\mathbf{x}, t) = \sum_{i=1}^{N} \Phi_h(\mathbf{x}_i, t)\varphi_i(\mathbf{x}) = \sum_{i=1}^{N} \Phi_i(t)\varphi_i(\mathbf{x}) \tag{4.79}$$

$$\Phi_h^H(\mathbf{x}, t) = \sum_{i=1}^{N} \Phi_h(\mathbf{x}_i, t)(\varphi_h^H)_i(\mathbf{x}) = \sum_{i=1}^{N} \Phi_i(t)(\varphi_h^H)_i(\mathbf{x}). \tag{4.80}$$

The reason the coefficients are the same in both representations (4.79) and (4.80) is due to the decomposition (4.62).

Inserting the above representations (4.79) and (4.80) into (4.78) and replacing w_h and w_h^H by $\varphi_j(\mathbf{x})$ and $(\varphi_h^H)_j(\mathbf{x})$, $j = \overline{1, N}$ we obtain:

$$\begin{aligned} &\text{Find } \Phi_i(t) \text{ s.t. } \quad \forall j = \overline{1, N}, \\ &\sum_{i=1}^{N}\Big(\int_\Omega \varphi_i(\mathbf{x})\varphi_j(\mathbf{x})d\mathbf{x}\Big)\frac{\partial \Phi_i}{\partial t}(t) + \sum_{i=1}^{N}\Big(\int_\Omega (\nabla \cdot \mathbf{v}_H)\varphi_i(\mathbf{x})\varphi_j(\mathbf{x})d\mathbf{x}\Big)\Phi_i(t) + \\ &c_b\sum_{i=1}^{N}\Big(\sum_{\mathbf{K}_h \in \tau_h} \text{meas}(\mathbf{K}_h)^{1/3}\int_{\mathbf{K}_h} (\nabla(\varphi_h^H)_i(\mathbf{x}) \cdot \nabla(\varphi_h^H)_j(\mathbf{x}))d\mathbf{x}\Big)\Phi_i(t) + \\ &c_{sc}\sum_{i=1}^{N}\Big(\sum_{\mathbf{K}_H \in \tau_H} \text{meas}(\mathbf{K}_H)^{1/3}\frac{||\nabla \Phi_h^H(\mathbf{x}, t)||_{0,\mathbf{K}_H}}{||\nabla \Phi_h(\mathbf{x}, t)||_{0,\mathbf{K}_H}}\int_{\mathbf{K}_H} (\nabla\varphi_i(\mathbf{x}) \cdot \nabla\varphi_j(\mathbf{x}))d\mathbf{x}\Big)\Phi_i(t) = 0. \end{aligned} \tag{4.81}$$

If the fully discrete sub-grid-stabilized finite element case is considered,

$$\Phi_h^n(\mathbf{x}) = \sum_{i=1}^{N} \Phi_h(\mathbf{x}_i, t^n)\varphi_i(\mathbf{x}) = \sum_{i=1}^{N} \Phi_i^n \varphi_i(\mathbf{x}), \tag{4.82}$$

$$(\Phi^n)_h^H(\mathbf{x}) = \sum_{i=1}^{N} \Phi_h(\mathbf{x}_i, t^n)(\varphi_h^H)_i(\mathbf{x}) = \sum_{i=1}^{N} \Phi_i^n (\varphi_h^H)_i(\mathbf{x}) \tag{4.83}$$

Using a similar procedure as the one described above for the finite element formulation (no stabilization), we obtain:

(4.84)

$$\sum_{i=1}^{N}\Big(\int_\Omega \{3 + 2\Delta t[\nabla\cdot(2\mathbf{v}^n - \mathbf{v}^{n-1})]\}\varphi_i(\mathbf{x})\varphi_j(\mathbf{x})d\mathbf{x}\Big)\Phi_i^{n+1} +$$

$$2c_b\Delta t\sum_{i=1}^{N}\Big(\sum_{\mathbf{K}_h\in\tau_h}\mathrm{meas}(\mathbf{K}_h)^{1/3}\int_{\mathbf{K}_h}(\nabla(\varphi_h^H)_i(\mathbf{x})\cdot\nabla(\varphi_h^H)_j(\mathbf{x}))d\mathbf{x}\Big)\Phi_i^{n+1} +$$

$$2c_{sc}\Delta t\sum_{i=1}^{N}\Big(\sum_{\mathbf{K}_H\in\tau_H}\mathrm{meas}(\mathbf{K}_H)^{1/3}\frac{||\nabla\Phi_h^H(\mathbf{x},t^{n+1})||_{0,\mathbf{K}_H}}{||\nabla\Phi_h(\mathbf{x},t^{n+1})||_{0,\mathbf{K}_H}}\int_{\mathbf{K}_H}(\nabla\varphi_i(\mathbf{x})\cdot\nabla\varphi_j(\mathbf{x}))d\mathbf{x}\Big)\Phi_i^{n+1}$$

$$= \sum_{i=1}^{N}\Big(\int_\Omega \varphi_i(\mathbf{x})\varphi_j(\mathbf{x})d\mathbf{x}\Big)\Big(4\tilde{\Phi}_i^n - \tilde{\Phi}_i^{n-1}\Big)$$

or,

$$(M_{vf}^{n+1} + 2\Delta t S_h^H + 2\Delta t(C_h^H)^{n+1})\Phi^{n+1} = M(4\tilde{\Phi}^n - \tilde{\Phi}^{n-1}), \tag{4.85}$$

where we made use of the notations (4.41) together with:

$$\begin{aligned}(S_h^H)_{i,j} &= c_b\Big(\sum_{\mathbf{K}_h\in\tau_h}\mathrm{meas}(\mathbf{K}_h)^{1/3}\int_{\mathbf{K}_h}(\nabla(\varphi_h^H)_i(\mathbf{x})\cdot\nabla(\varphi_h^H)_j(\mathbf{x}))d\mathbf{x}\Big),\\ (C_h^H)_{i,j}^{n+1} &= c_{sc}\Big(\sum_{\mathbf{K}_H\in\tau_H}\mathrm{meas}(\mathbf{K}_H)^{1/3}\frac{||\nabla\Phi_h^H(\mathbf{x},t^{n+1})||_{0,\mathbf{K}_H}}{||\nabla\Phi_h(\mathbf{x},t^{n+1})||_{0,\mathbf{K}_H}}\int_{\mathbf{K}_H}(\nabla\varphi_i(\mathbf{x})\cdot\nabla\varphi_j(\mathbf{x}))d\mathbf{x}\Big)\end{aligned} \tag{4.86}$$

Let us ignore for the moment the term $\mathrm{meas}(\mathbf{K}_h)^{1/3}$ that is in from of the local integral in S_h^H (4.87). Then the integral becomes simply:

$$\begin{aligned}(S_h^H)_{i,j} &= c_b\int_\Omega(\nabla(\varphi_h^H)_i(\mathbf{x})\cdot\nabla(\varphi_h^H)_j(\mathbf{x}))d\mathbf{x} =\\ &c_b\sum_{\mathbf{K}_H\in\tau_H}\int_{\mathbf{K}_H}(\nabla(\varphi_h^H)_i(\mathbf{x})\cdot\nabla(\varphi_h^H)_j(\mathbf{x}))d\mathbf{x}.\end{aligned} \tag{4.87}$$

One general remark must be done at this point: even if one node of one macro-element, let us say node 1 in Fig. 4.2 does not belong to a small sub-element, for instance to the second

sub-element with the vortices 5, 6, 9 and 2, it doesn't mean that $(\varphi_h^H)_1$ has no contribution to the global matrix, since its support is larger than the support of $(\varphi_h)_1$. Because of this situation, instead of computing one local matrix and then assemble it to the global matrix the way it was done before (when we computed the matrices for the case of finite element method without stabilization) now, four different local matrices must be computed separately and than assembled to the global matrix.

Therefore, in order to compute $\int_{\mathbf{K}_H}(\nabla(\varphi_h^H)_i(\mathbf{x})\cdot\nabla(\varphi_h^H)_j(\mathbf{x}))d\mathbf{x}$, first we compute the local matrices corresponding to both i and j being nodes of the rough grid (nodes 1 to 10 in Fig. 4.2), secondly we compute the local matrices corresponding to i being a node of the rough grid and j being a node of the fine grid only (nodes 5 to 10 in a local numbering of a sub-tetrahedron or nodes 11 to 35 in Fig. 4.2), thirdly we compute the local matrices corresponding to i being a node of the fine grid only (the mid-pints of the sub-elements) and j being a node of the rough grid and at last, we compute the local matrices corresponding to both i and j being nodes of the fine grid but not of the rough grid. This can be summarized in the following manner:

$$\text{Case 1: } i\ ,\ j \in \mathcal{T}_H,$$

$$\text{Case 2: } i\ \in \mathcal{T}_H \text{ and } j\ \in \mathcal{T}_h - \mathcal{T}_H,$$

$$\text{Case 3: } i\ \in \mathcal{T}_h - \mathcal{T}_H \text{ and } j\ \in \mathcal{T}_H,$$

$$\text{Case 4: } i\ ,\ j \in \mathcal{T}_h - \mathcal{T}_H.$$

In order to do so, we introduce two different connectivity tables, one for the rough grid and one for the fine grid. Except for this, we use exactly the same procedure to compute the matrix S_h^H as we showed in the case of M_{vf}^{n+1}.

We discretized the equations in the same manner and we obtained the following matricial form for computing the intermediate velocities $\mathbf{u}_p^{n+1}$, $\mathbf{v}_p^{n+1}$.

(4.88)

$$\begin{pmatrix} M_1 & M_2+\Delta t(S_1+S_h^H+(C_h^H)_v) \\ M_3+\Delta t(S_2+S_h^H+(C_h^H)_u) & M_1 \end{pmatrix}\begin{pmatrix} \mathbf{u}_p^{n+1} \\ \mathbf{v}_p^{n+1} \end{pmatrix} = \begin{pmatrix} rhs_2 \\ rhs_1 \end{pmatrix}$$

where

$$
\begin{aligned}
(M_1)_{ij} &= -\int_\Omega (\frac{3}{2}\Phi^{n+1}\mu(\Phi^{n+1}) + \Delta t\beta(\Phi^{n+1}))\varphi_i(\mathbf{x})\varphi_j(\mathbf{x})d\mathbf{x},\\
(M_2)_{ij} &= \int_\Omega (\frac{3}{2}\alpha\Phi^{n+1} + \frac{3}{2}\Phi^{n+1}\mu(\Phi^{n+1}) + \Delta t\beta(\Phi^{n+1}))\varphi_i(\mathbf{x})\varphi_j(\mathbf{x})d\mathbf{x},\\
(M_3)_{ij} &= \int_\Omega (\frac{3}{2}(1-\Phi^{n+1}) + \frac{3}{2}\Phi^{n+1}\mu(\Phi^{n+1}) + \Delta t\beta(\Phi^{n+1}))\varphi_i(\mathbf{x})\varphi_j(\mathbf{x})d\mathbf{x},\\
(S_1)_{ij} &= \int_\Omega \mu_d(\Phi^{n+1})\nabla\varphi_i(\mathbf{x})\cdot\nabla\varphi_j(\mathbf{x})d\mathbf{x},\\
(S_2)_{ij} &= \int_\Omega \mu_c(\Phi^{n+1})\nabla\varphi_i(\mathbf{x})\cdot\nabla\varphi_j(\mathbf{x})d\mathbf{x},\\
(M_\Phi)_{ij} &= -\int_\Omega \Phi^{n+1}\varphi_i(\mathbf{x})\varphi_j(\mathbf{x})d\mathbf{x},\\
(M_{\Phi\mu})_{ij} &= -\int_\Omega \Phi^{n+1}\mu(\Phi^{n+1})\varphi_i(\mathbf{x})\varphi_j(\mathbf{x})d\mathbf{x},\\
(M_\xi[k])_{ij} &= -\int_\Omega \xi(\Phi^{n+1})\frac{\partial\varphi_i(\mathbf{x})}{\partial x_k}\varphi_j(\mathbf{x})d\mathbf{x},\\
(L_1[k])_{ij} &= -\int_\Omega \Phi^{n+1}\varphi_i(\mathbf{x})\frac{\partial\psi_j(\mathbf{x})}{\partial x_k}d\mathbf{x},\\
(L_3[k])_{ij} &= -\int_\Omega (1-\Phi^{n+1})\varphi_i(\mathbf{x})\frac{\partial\psi_j(\mathbf{x})}{\partial x_k}d\mathbf{x},
\end{aligned}
\tag{4.89}
$$

$$
\begin{aligned}
(L_{1p}[k])_{ij} &= \int_\Omega \psi_j(\mathbf{x})\frac{\partial(\Phi^{n+1}\varphi_i)(\mathbf{x})}{\partial x_k}d\mathbf{x},\\
(L_{3p}[k])_{ij} &= \int_\Omega \frac{\partial((1-\Phi^{n+1})\varphi_i(\mathbf{x}))}{\partial x_k}\psi_j(\mathbf{x})d\mathbf{x},\\
(L_4)_{ij} &= \int_\Omega \varphi_i(\mathbf{x})\psi_j(\mathbf{x})d\mathbf{x},\\
(M_6)_{ij} &= M_{ij} - (M_\Phi)_{ij},\\
I_\Phi &= \int_\Omega \varphi_i(\mathbf{x}),\\
(PS)_{ij} &= \int_\Omega \nabla\psi_i(\mathbf{x})\cdot\nabla\psi_j(\mathbf{x})d\mathbf{x},
\end{aligned}
\tag{4.90}
$$

$$
\begin{aligned}
rhs_1 &= 2\alpha M_\Phi\tilde{\mathbf{v}}^n - \frac{1}{2}\alpha M_\Phi\tilde{\mathbf{v}}^{n-1} + 2M_{\Phi\mu}\tilde{\mathbf{u}}\tilde{\mathbf{v}}^n - \frac{1}{2}M_{\Phi\mu}\tilde{\mathbf{u}}\tilde{\mathbf{v}}^{n-1}\\
&+ \Delta t M_\xi\Phi^{n+1} + \Delta t L_1 p^n - \Delta t\frac{\alpha}{1-\alpha}\frac{1}{Fr}(0,0,M\Phi^{n+1}),\\
rhs_2 &= 2M_6\tilde{\mathbf{u}}^n - \frac{1}{2}M_6\tilde{\mathbf{u}}^{n-1} - 2M_{\Phi\mu}\tilde{\mathbf{u}}\tilde{\mathbf{v}}^n + \frac{1}{2}M_{\Phi\mu}\tilde{\mathbf{u}}\tilde{\mathbf{v}}^{n-1}\\
&- \Delta t M_\xi\Phi^{n+1} + \Delta t L_3 p^n - \Delta t\frac{1}{1-\alpha}\frac{1}{Fr}(0,0,I_\Phi - M\Phi^{n+1}).
\end{aligned}
\tag{4.91}
$$

The correction equation for the pressure is:

$$PSp^{n+1} = PSp^n + \frac{3(1-\alpha)}{4(\Delta t)^2}(L_4)^T(3\Phi^{n+1} - 4\Phi^n + \Phi^{n-1}) - \frac{3\alpha}{2\Delta t}(L_{1p})^T \cdot \mathbf{v}_p^{n+1} - \frac{3}{2\Delta t}(L_{3p})^T \cdot \mathbf{u}_p^{n+1} \tag{4.92}$$

The matricial form of the equations for $\mathbf{u}^{n+1}$, $\mathbf{v}^{n+1}$ is:

$$\begin{pmatrix} M_1 & M_2 \\ M_3 & M_1 \end{pmatrix} \begin{pmatrix} \mathbf{u}^{n+1} \\ \mathbf{v}^{n+1} \end{pmatrix} = \begin{pmatrix} rhs_4 \\ rhs_3 \end{pmatrix}, \tag{4.93}$$

where

$$rhs_3 = M_3\mathbf{u}_p^{n+1} + M_1\mathbf{v}_p^{n+1} + \Delta t L_1(p^{n+1} - p^n),$$
$$rhs_4 = M_1\mathbf{u}_p^{n+1} + M_2\mathbf{v}_p^{n+1} - \Delta t L_3(p^{n+1} - p^n). \tag{4.94}$$

All the velocity matrices (the matrices of the form $(M_1)_{i,j}$) are stored into eight different blocks corresponding to the cases: j free node, j node has its x velocity component prescribed, j node has its y velocity component prescribed, j node has its z velocity component prescribed, j node has its x and y velocity components prescribed, j node has its x and z velocity components prescribed, j node has its y and z node prescribed and j node is Dirichlet node (all its components are prescribed). Of course, if the gas and liquid velocities have different boundary conditions, than we have to introduce two different structures for storing the matrices. If the matrices are symmetric, than i goes only through the free nodes and we only store the above diagonal part of the matrix. For the void fraction and pressure matrices the situation is simplified, since we only create two blocks corresponding to the free or prescribed case. When solving for each component of the vectors $\mathbf{u}_p^{n+1}$, $\mathbf{v}_p^{n+1}$ or for $\mathbf{u}^{n+1}$, $\mathbf{v}^{n+1}$, if some nodes have that particular component of velocity prescribed, they become part of right hand side.

When dealing with periodic boundary conditions, a new connectivity table was created such that, if nodes i and j were periodic and conTable[el1][node1]=i and conTable[el2][node2]=j than conTableNew[el1][node1]=i but conTableNew[el2][node2]=i. The effect of this new connectivity table was that it produced condensed matrices, in the sense that if nodes i and j were periodic, than both the lines and the columns i and j were added up together, reducing the size of the matrix. That is all that must be done when dealing with velocity matrices. However, when dealing with matrices of type L or PS (when we must compute the products $L \cdot p$ or $PS \cdot p$), we must bear in mind that periodicity in the vertical direction for the pressure is different than

the periodicity for the velocity. The nodes i and j are z periodic if :

$$
\begin{aligned}
(v_z)_i &= (v_z)_j, \\
(u_z)_i &= (u_z)_j, \\
p_j - p_i &= \nabla p(z_j - z_i).
\end{aligned}
\tag{4.95}
$$

Because of this situation, the above described condensation is not enough. If the first row of $PS \cdot p$ is:

$$
\begin{aligned}
& a_{11}p_1 + a_{12}p_2 + ... + a_{1i}p_i + ... + a_{1j}p_j + ... = rhs_1, \\
& a_{11}p_1 + a_{12}p_2 + ... + (a_{1i} + a_{1j})p_i + \nabla p\, a_{1j}(z_j - z_i) + ... = rhs_1,
\end{aligned}
\tag{4.96}
$$

the $PS \cdot p$ will be replaced by $(PS)_{condensed} \cdot p_{condensed} + V_p$. The vector that compensates for the difference between the pressure of two periodic nodes is sent to the right hand side of the equation.

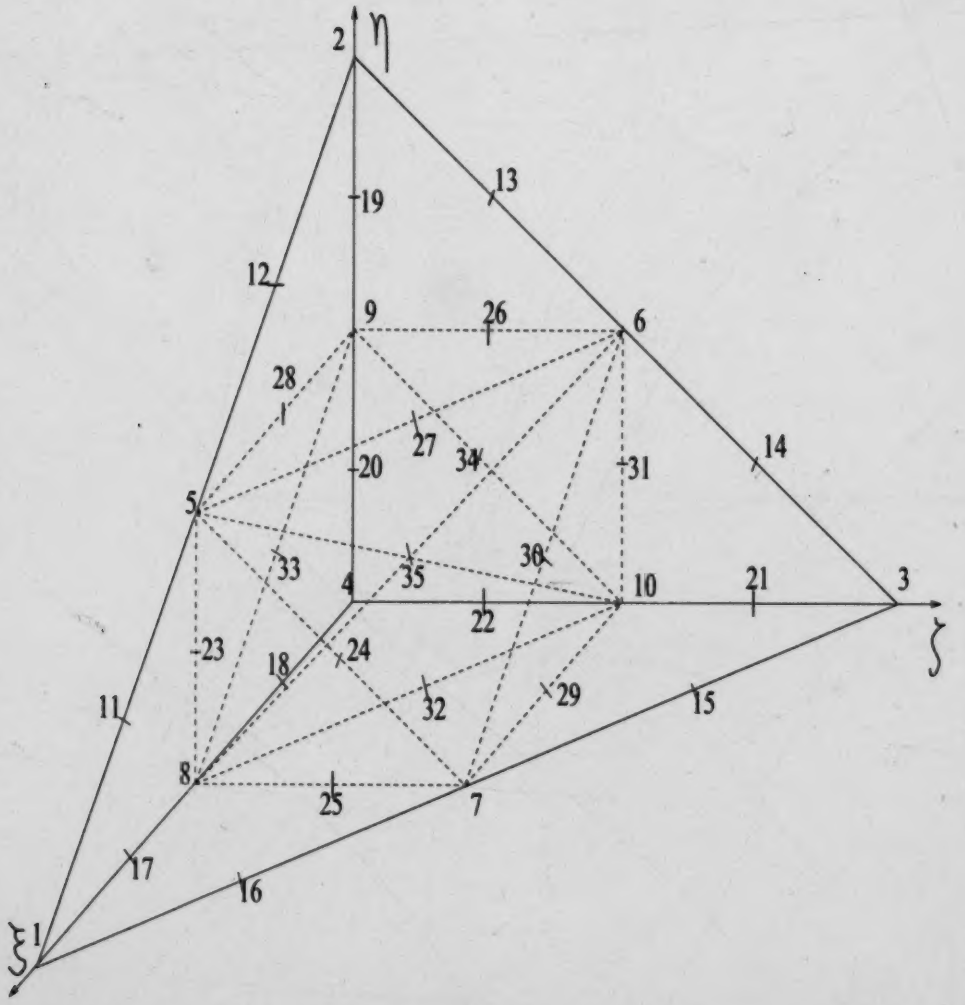

Figure 4.2: Tetrahedral element in local coordinate system, with axes (ξ,η,ζ) where a detailed subgriding is included

Chapter 5

A void fraction wave propagation problem

5.1 Non-linear analysis: modified bulk modulus of elasticity

Minev *et al.* (1999) compared the multiphase flow models relevant to bubbly flows available in the literature by performing one-dimensional linear and nonlinear analysis. The linear analysis of the various possible models showed that only those formulated by Biesheuvel *et al.* (1990) and Stuhmiller (1977) provided reasonable neutral stability curves and critical values for the void fraction. However, the nonlinear analysis of the two models produces a nonlinear equation whose solution is unstable in the long run. There is experimental evidence for the existence of stable void fraction waves. This study revealed that neither of the existing multiphase flow models produces realistic results. However, the study was one-dimensional while any realistic experiment is three-dimensional. Theoretically, there exists a possibility that the initially one-dimensional waves generate, via the nonlinear interaction, three-dimensional waves that could dissipate enough energy to yield a stable (3D) wave solution. This possibility was investigated by introducing a small disturbance in the trivial solution (5) and simulating its development in a 3D cubic domain by solving the full three-dimensional system of equations (4.17)-(4.23). Periodic boundary conditions are imposed in all three directions. The length of the side of the cube is equal to 1. The mesh size used is $dx = dy = dz = 0.05$. Most of the work presented in this chapter has been already published [1].

[1] A variant of this chapter appeared in [30]

The trivial solution (4.5) has the following dimensionless form

$$\Phi = \Phi_0, \quad \mathbf{u} = (0,0,0), \quad \mathbf{v} = (0,0,1)$$
$$\nabla p = \frac{1}{Fr}(\Phi_0 - \frac{1}{1-\alpha}), \tag{5.1}$$

and the perturbed initial condition was chosen to be

$$\Phi(x,y,z,t=0) = \Phi_0 = 0.1, \quad \mathbf{u}(x,y,z,t=0) = (0,0,0),$$
$$\mathbf{v}(x,y,z,t=0) = (0,0,1.0 + 0.01\ \sin(4\pi z)) \tag{5.2}$$

In this case, as shown in Figs. 5.1, 5.2, 5.3 and 5.4, the initial disturbance fades away (within the accuracy of the scheme). The same conclusion can be drawn by analyzing the void fraction profiles in the Figs. 5.5 and 5.6. This indicates that for $\Phi_0 = 0.1$ the trivial solution (5.1) is stable. If Figs. 5.3 and 5.4 or 5.5 and 5.6 are compared, it can be concluded that the amplitude of the wave is slightly decreased. This means that the stabilization terms make the solution reach the steady state in less computational time. In Figs. 5.3 and 5.4, the point that was monitored has as coordinates: $(x,y) = (0.5,0.5)$. Most of the profiles showed in Figs. 5.3 - 5.11 have rough edges because of the mesh resolution ($dx = 0.05$).

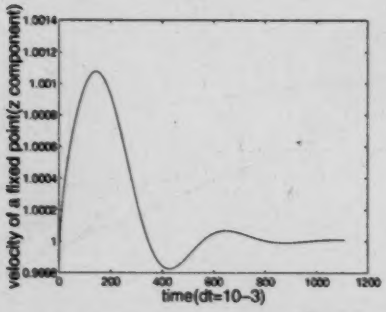

Figure 5.1: Velocity profile of a fixed point in time.$\Phi_0 = 0.1$(with stabilization)

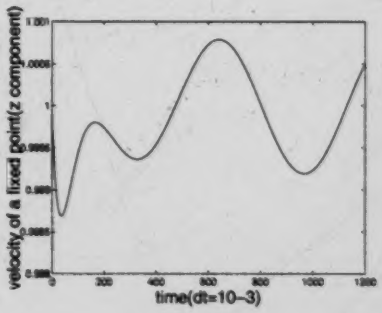

Figure 5.2: Velocity profile of a fixed point in time.$\Phi_0 = 0.1$(no stabilization)

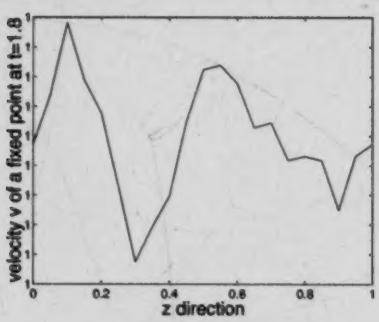

Figure 5.3: The velocity profile in the z direction at the final time.$\Phi_0 = 0.1$ (with stabilization)

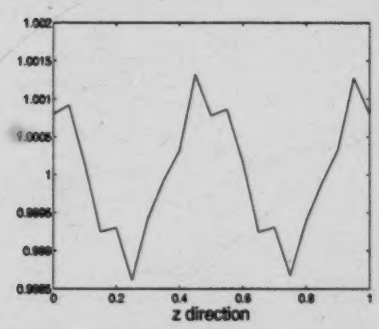

Figure 5.4: The velocity profile in the z direction at the final time(x and y are fixed) $\Phi_0 = 0.1$ (no stabilization)

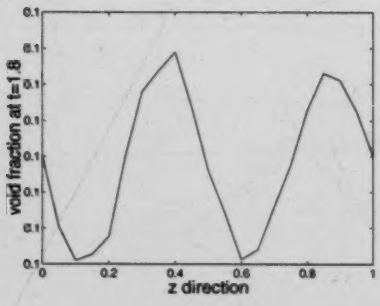

Figure 5.5: The void fraction profile in the z direction at the final time (x and y are fixed) $\Phi_0 = 0.1$ (with stabilization)

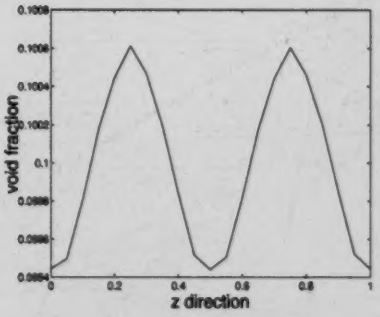

Figure 5.6: The void fraction profile in the z direction at the final time(x and y are fixed) $\Phi_0 = 0.1$ (no stabilization)

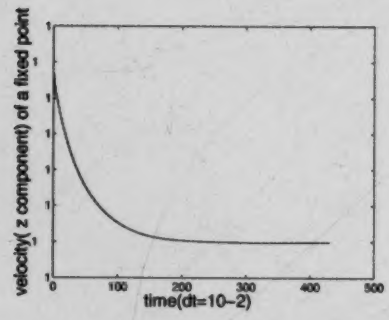

Figure 5.7: Velocity of a fixed point in time $\Phi_0 = 0.15$(random perturbation) (with stabilization)

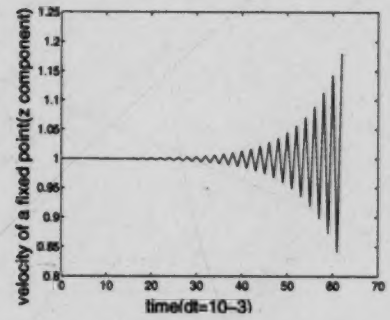

Figure 5.8: The velocity profile of a fixed point in time $\Phi_0 = 0.175$

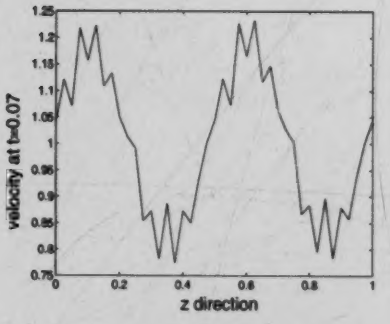

Figure 5.9: The velocity profile in the z direction at the final time(x and y are fixed).$\Phi_0 = 0.175$. (Case:with stabilization)(random perturbation)

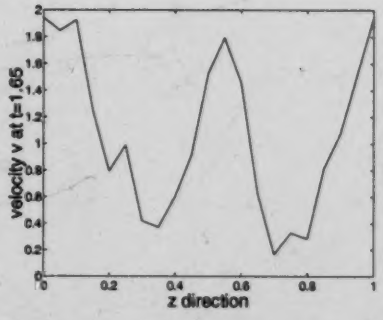

Figure 5.10: The velocity profile in the z direction at the final time(x and y are fixed).$\Phi_0 = 0.15$.(drag coefficient given by (3.10)) (Case:with stabilization)(random perturbation)

Similar results were obtained for higher initial void fraction values ($\Phi_0 = 0.15$) and random perturbation of amplitude 0.01 as can be seen in Fig. 5.7.

$$\Phi(x,y,z,t=0) = \Phi_0 = 0.15, \quad \mathbf{u}(x,y,z,t=0) = (0,0,0)$$
$$\mathbf{v}(x,y,z,t=0) = (0,0,1.0 + 0.01 \text{ random}[z]) \tag{5.3}$$

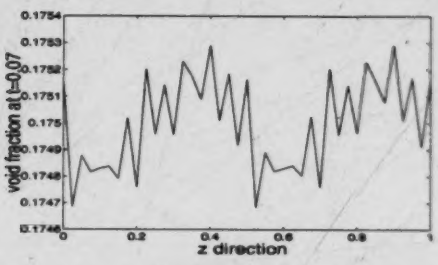

Figure 5.11: The void fraction profile in the z direction at the final time(x and y are fixed).$\Phi_0 = 0.175$.(Case:with stabilization)(random perturbation)

At initial void fraction $\Phi_0 = 0.175$, the perturbation is amplified exponentially in time, as it can be seen in Fig. 5.8, Fig. 5.9 and Fig. 5.11. Actually, by varying the initial void fraction, it can be concluded that up to a value of the void fraction approximately equal to 0.155 the initial disturbance fades away. For larger values, the solution loses stability because of the wave breaking phenomena. The same threshold of instability was obtained if the stabilization technique was used. This indicates that the scheme is not overstabilized.

There is, however, experimental and theoretical evidence that such a flow is dissipative enough, to allow for stable void fraction waves to be developed (see Lammers *et al.* (1996)). This suggests that the expressions for the coefficients of the closure terms must be modified. As mentioned above, there is agreement in the literature regarding the magnitude of the added-mass coefficient. The other closure terms are the drag coefficient and the bulk modulus of elasticity. We first analyze the influence of the drag coefficient.

In the undistorted particle regime (viscous regime), Ishii *et al.* (1979) suggest the following form of the drag coefficient $C_D = 24/Re_m(1+0.1Re_m^{0.75})$, where $Re_m = \dfrac{2r_d\rho_1|\mathbf{v}-\mathbf{u}|}{\mu_m}$ and r_d is the particle radius. μ_m, the mixture velocity, is approximated as $\mu_m = \mu_c\dfrac{1}{1-\Phi}$. Since the drag force per unit volume is $3C_D/(8r_d)\rho_1\Phi|\mathbf{v}-\mathbf{u}|(\mathbf{v}-\mathbf{u})$ it follows that $\beta = 3C_D/(8r_d)\rho_1\Phi|\mathbf{v}-\mathbf{u}|$. For void fraction equal to 0.15, the solution becomes unstable, as it is demonstrated in Figs. 5.12 and Figs. 5.13.

Cliff *et al.* (1978) suggest another form of the drag coefficient, which gives a good fit to numerical predictions of drag on spherical bubbles (for $Re \gg 2$):

$$C_D = 14.9Re^{-0.78}, \quad \text{where} \quad Re = \frac{\rho_1 r_d v_\infty}{\mu_c}.$$

Using this new form of the drag coefficient, the initial perturbation increases exponentially even for lower initial values of the void fraction, before any nonlinear behavior is observed. This can be notice if we compare (5.7) with (5.12), (5.14) with (5.10) and (5.15) with (5.13).

Therefore we concluded that the drag coefficient does not significantly alter the qualitative behavior of the system.

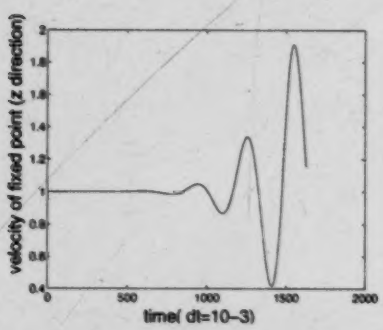

Figure 5.12: The velocity profile of a fixed point in timeΦ_0 = 0.15(Zuber's drag)(random perturbation)

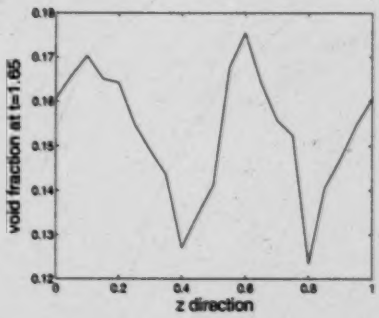

Figure 5.13: The void fraction profile in the z direction at the final timeΦ_0 = 0.15(Zuber's drag coefficient)(with stabilization)(random perturbation)

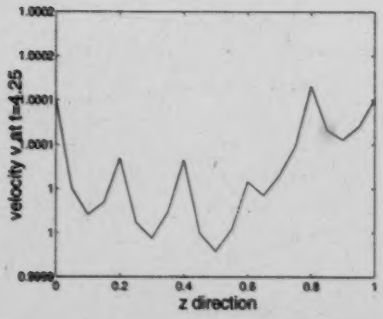

Figure 5.14: The velocity profile in the z direction at the final time(x and y are fixed).Φ_0 = 0.15. (Case:with stabilization)(random perturbation)

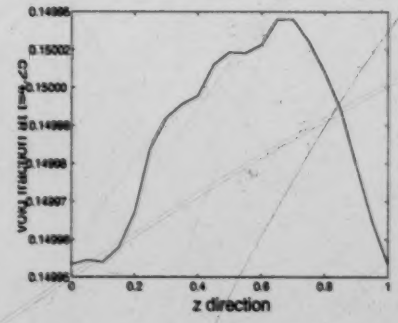

Figure 5.15: The void fraction profile in the z direction at the final time(x and y are fixed).Φ_0 = 0.15.(Case:with stabilization)(random perturbation)

In order to find the reason for the unstable (and aphysical) behavior of the system, we performed a weakly nonlinear analysis using the original set of of equations (4.1)-(4.4) for the one-dimensional case. Since we want to compare our results with the experiments performed by Lammers *et al.* (1996), the following conditions must be met:

(i) The superficial liquid velocity $j_l = (1-\Phi)u$ must be equal to 0.03 m/s.

(ii) The mixture velocity $U_m = \Phi v + (1-\Phi)u$ should be time-independent. Since Lammers *et al.* (1996) presented their results in a frame of reference moving with the bulk velocity U_m, we use the same reference frame. In order to define all quantities in a zero-volume-flux reference frame, as done by Lammers *et al.* (1996), it is necessary to transform the variables.

(iii) $v = U_m + U(\Phi)$ where $U(\Phi) = v_\infty(1-\Phi)(1-\Phi+0.55\Phi^2)$ and $v_\infty = 0.219\ m/s$

(iv) The drag coefficient $\beta(\Phi)$ must be chosen so that to be in agreement with (i),(ii) and (iii).

If we combine (i), (ii) and (iii) we obtain:

$$v - u = \frac{U(\Phi)}{1-\Phi}.$$

A trivial solution to the equations (4.1)-(4.4) is:

$$v - u = \frac{\Phi(1-\Phi)(\rho_1-\rho_2)g}{\beta(\Phi)}, \tag{5.4}$$

$$\nabla p = -(\Phi\rho_2 + (1-\Phi)\rho_1)g.$$

These relations yield the value of the drag coefficient that fits the experiments.

$$\beta(\Phi) = \frac{\Phi(1-\Phi)^2(\rho_1-\rho_2)g}{U(\Phi)}. \tag{5.5}$$

Using the above formula for the drag coefficient, the weakly nonlinear analysis yields a certain expression for the added-mass term corresponding to the experimentally observed value of the effective diffusivity. However, since the coefficients were modified, the dimensionless set of momentum equations to be used from now on must be specified

$$\Phi\frac{D_{\mathbf{v}}\mathbf{v}}{Dt} = -\frac{1}{\alpha}\Phi\nabla p - \frac{\xi(\Phi)}{\rho_2 v_*^2}\nabla\Phi - \frac{1}{Fr}\frac{1}{\alpha}\frac{\Phi(1-\Phi)^2}{\bar{U}(\Phi)}(\mathbf{v}-\mathbf{u}) - \frac{1}{Fr}\frac{\Phi}{1-\alpha}(0,0,1)$$

$$-\frac{1}{\alpha}\Phi\mu(\Phi)\frac{D_{\mathbf{v}}(\mathbf{v}-\mathbf{u})}{Dt} + \frac{1}{\rho_2 l v_*}\nabla\cdot(\mu_d(\Phi)\nabla\mathbf{v}) \tag{5.6}$$

(5.7)

$$(1-\Phi)\frac{D_{\mathbf{u}}\mathbf{u}}{Dt} = -(1-\Phi)\nabla p + \frac{\xi(\Phi)}{\rho_1 v_\star^2}\nabla\Phi + \frac{1}{Fr}\frac{\Phi(1-\Phi)^2}{\breve{U}(\Phi)}(\mathbf{v}-\mathbf{u}) - \frac{1}{Fr}\frac{1-\Phi}{1-\alpha}(0,0,1) + \Phi\mu(\Phi)\frac{D_{\mathbf{v}}(\mathbf{v}-\mathbf{u})}{Dt}$$

where $v_\star = U(\Phi_0)$ is the velocity scale used for non-dimensionalization and $T = 4.352s$ (or $T = 2.176s$) is the time scale corresponding to the wave periods imposed in the experiments. The length scale $l = v_\star T$.

If the pressure is eliminated from the dimensionless equations and the velocity of the mixture is assumed to be constant, in other words:

$$u = -\frac{\Phi}{1-\Phi}v + \frac{\overline{U}_m}{1-\Phi},$$

the system of equations can be reduced to two equations in terms of v and Φ only: the continuity equation (4.6) and

$$\alpha_1(\Phi)\frac{Dv}{Dt} + \alpha_2(\Phi)(v-\overline{U}_m)\frac{\partial v}{\partial x} = \alpha_3(\Phi,v)\frac{\partial\Phi}{\partial x} - \frac{1}{Fr}\alpha_4(\Phi)(v-\overline{U}_m) +$$

(5.8)
$$\frac{1}{Fr}\alpha_5(\Phi) + \frac{\partial(\alpha_6(\Phi)\frac{\partial v}{\partial x})}{\partial x}$$

where

(5.9)
$$\alpha_1(\Phi) = \alpha\Phi + \frac{\Phi^2}{1-\Phi} + \frac{\Phi}{(1-\Phi)^2}\mu(\Phi),$$

(5.10)
$$\alpha_2(\Phi) = -2\frac{\Phi^2}{(1-\Phi)^2} - \frac{\Phi^2}{(1-\Phi)^3}\mu(\Phi),$$

(5.11)
$$\alpha_3(\Phi,v) = \frac{(v-\overline{U}_m)^2\Phi}{(1-\Phi)^3} - \frac{\xi(\Phi)}{(1-\Phi)\rho_1 v_\star^2},$$

(5.12)
$$\alpha_4(\Phi) = \frac{\Phi}{\overline{U}(\Phi)},$$

(5.13)
$$\alpha_5(\Phi) = \Phi,$$

(5.14)
$$\alpha_6(\Phi) = \frac{1}{\rho_1 l v_\star}\mu_d(\Phi).$$

In an experiment on the wave propagation in an uniform bubbly flow (see Lammers *et al.* (1996)), it was noticed that only the long wavelength components of the initial disturbance

could propagate over appreciable distances. That is why it is convenient to introduce 'fast' and 'slow' space/time scales.

$$\theta = t - \frac{1}{c_0}x,$$

$$Z = \epsilon x,$$

$$\Phi_0 = 0.06,$$

$$\Phi(x,t,\epsilon) = \tilde{\Phi}(\theta, Z, \epsilon) = \Phi_0 + \epsilon\tilde{\Phi}_1(\theta, Z) + \epsilon^2\tilde{\Phi}_2(\theta, Z) + \dots,$$

$$v(x,t,\epsilon) = \tilde{v}(\theta, Z, \epsilon) = \overline{U}_m + \overline{U}(\Phi_0) + \epsilon\tilde{v}_1(\theta, Z) + \epsilon^2\tilde{v}_2(\theta, Z) + \dots.$$

By eliminating the velocity, we obtain for Φ_1 the following Burgers' equation in the original variables:

$$\frac{\partial\Phi_1}{\partial x} + \left(\frac{1}{\bar{a}_0} - \frac{\bar{a}_1}{\bar{a}_0^2}\Phi_1\right)\frac{\partial\Phi_1}{\partial t} = \frac{\bar{D}}{\bar{a}_0^3}\frac{\partial^2\Phi_1}{\partial t^2},$$

where

(5.15)
$$\bar{a}(\Phi) = \overline{U}_m + \overline{U}(\Phi) + \Phi\frac{d\overline{U}}{d\Phi},$$

$$\bar{a}_0 = \bar{a}(\Phi_0),$$

$$\bar{a}_1 = \{d\bar{a}/d\Phi\}_{\Phi=\Phi_0},$$

(5.16)
$$\bar{D} = \frac{D}{v_* l} = \vec{U}(\Phi_0)\Big((\overline{U}_m + \overline{U}(\Phi_0) + \alpha_2(\Phi_0)\overline{U}(\Phi_0) - \bar{a}_0\alpha_1(\Phi_0))\left\{\frac{d\overline{U}}{d\Phi}\right\}_{\Phi=\Phi_0}$$
$$- \alpha_3(\Phi_0, \overline{U}_m + \overline{U}(\Phi_0))\Big)$$

The overbarred quantities are the nondimensional equivalents of the original ones. By using the above formulae to compute the diffusivity for different values of Φ_0, we obtain a positive value up to a certain threshold and a negative value above that limit. For instance, at $\Phi_0 = 0.2$ we obtain $\bar{D} = -0.594$. Negative diffusivity naturally leads to unstable solutions of Burgers' equation. This explains the breaking wave phenomena that we obtained in the numerical simulations. On the other hand, Lammers *et al.* (1996) provided experimental evidence that, in this range of void fraction, the dimensioned diffusivity D is around $2.5{*}10^{-4}\frac{m^2}{s}$, and therefore a stable solution should exist.

Lammers *et al.* (1996) came up with the following polynomial fit for the kinematic wave speed measurements:

(5.17)
$$a(\Phi) = U_m + v_\infty(1-\Phi)(1 - 3.08\Phi + 2.77\Phi^2 - 0.55\Phi^3).$$

Since the kinematic wave speed was measured experimentally and then the velocity of the bubbles was obtained by integration of the relation (5.15), it is better to use this formula for the wave speed instead of (5.15). The formula (5.17) was used in our numerical simulations.

Using the above value for the diffusivity together with (5.11) and (5.16), the new expression for $\xi(\Phi)$ is determined.

$$\frac{\xi(\Phi)}{(1-\Phi)\rho_1 v_*^2} = \frac{(v-\overline{U}_m)^2\Phi}{(1-\Phi)^3} + \frac{\bar{D}}{\overline{U}(\Phi)} - (\overline{U}_m + \overline{U}(\Phi) + \alpha_2(\Phi)\overline{U}(\Phi) - \bar{a}(\Phi)\alpha_1(\Phi))\frac{d\overline{U}}{d\Phi} \tag{5.18}$$

The resulting expression for the bulk modulus of elasticity ξ (based on Lammers' measurements of the diffusivity in uniform bubbly flows) yields a Generalized Burgers equation with a positive viscosity, and the resulting wave solutions can be expected to be stable.

5.2 Validation of the new expression for the bulk modulus of elasticity

So far, we showed how to correct the bulk modulus of elasticity ξ. In order to verify our proposed expression of ξ against the experiments of Lammers *et al.* (1996), we simulated a fully 3D bubbly flow in a periodic cubic domain. Since at this range of void fraction the linear waves are strongly dissipated, in order for the nonlinear effect to occur, we start with an initial nonlinear wave profile given by the signal recorded at the lowest measuring station. The so-called Khokhlov solution is used to fit the measured wave profile.

$$\tilde{\Phi}(\hat{x},\hat{y},\hat{z}=x_1,\hat{t}) = \frac{\hat{t}}{T}\Delta\tilde{\Phi} + \tilde{\Phi}_0 - \frac{1}{2}\Delta\tilde{\Phi} - \frac{1}{2}\,\Delta\tilde{\Phi}\tanh(\frac{2}{S}(\hat{t}-\frac{T}{2})),\ \hat{t}\in[0,T]. \tag{5.19}$$

Note that their experiments can be described by the Burgers'equation in the form appropriate to signalling problems. Therefore, their space and time variables must be transformed into our time and space variables via:

$$\begin{aligned} \bar{t} &= \frac{1}{\bar{a}_0}\,(\hat{\bar{z}} - \hat{\bar{x}}_1), \\ \bar{z} &= \bar{a}_0\,\hat{\bar{t}}. \end{aligned} \tag{5.20}$$

All the overbarred variables are nondimensional. This yields:

$$\Phi(\bar{x},\bar{y},\bar{z},\bar{t}=0) = \bar{z}\frac{l}{L}\Delta\Phi + \Phi_0 - \frac{1}{2}\Delta\Phi - \frac{1}{2}\,\Delta\Phi\tanh(\frac{2l}{Sa_0}(\bar{z}-\frac{L}{2l})),\ \bar{z}\in\left[0,\frac{L}{l}\right], \tag{5.21}$$

where

$$L = a_0 T \quad \Phi_0 = 0.06 \qquad a_0 = 0.207 \quad D = 0.00023.$$

For the first set of experiments the following values are used

$$\Delta\Phi = 0.05 \quad T = 4.352 \quad S = 1.263.$$

For the second set of experiments the following values are used

$$\Delta\Phi = 0.05 \quad T = 2.176 \quad S = 0.526.$$

The heights of their measuring stations are: $\hat{z}_1 = 0.87\ m$, $\hat{z}_2 = 2.04\ m$, $\hat{z}_3 = 3.22\ m$ and $\hat{z}_1 = 4.47\ m$. Using (5.20), the corresponding nondimensional stopping times are: $\bar{t}_1 = 1.29$, $\bar{t}_2 = 2.60$ and $\bar{t}_3 = 3.99$ when $T = 4.352$ and $\bar{t}_1 = 2.59$, $\bar{t}_2 = 5.22$ and $\bar{t}_3 = 7.99$ when $T = 2.176$.

With the new values for the coefficients a standing wave, qualitatively and quantitatively similar to the one experimentally observed by Lammers *et al.* (1996) was obtained. The computed nonlinear waves are presented in the Figs. 5.16 and 5.17 and the experimental results of Lammers *et al.* (1996) [117] are presented in Figs. 5.18 and 5.19.

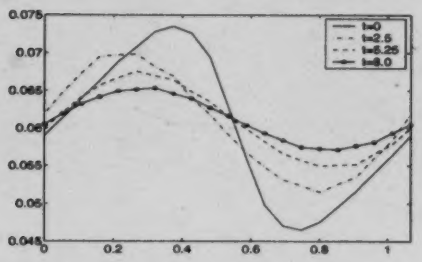

Figure 5.16: The void fraction profile in the z direction at t=0,2.5,5.25,8.0 from bottom to top when the period T=2.176 (x and y are fixed) $\Phi_0 = 0.06$

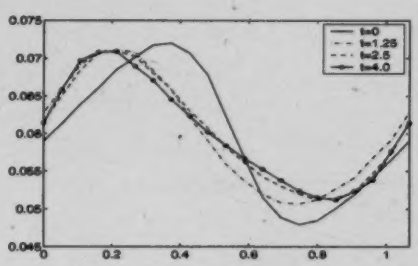

Figure 5.17: The void fraction profile in the z direction at t=0,1.25,2.5,4.0 from bottom to top when the period T=4.352 (x and y are fixed) $\Phi_0 = 0.06$

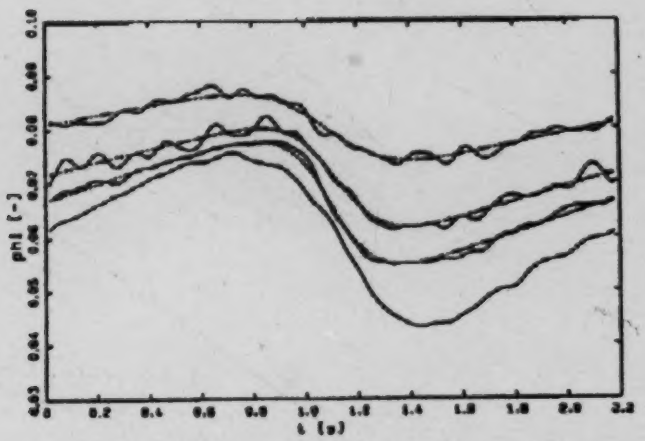

Figure 5.18: The evolution of sinusoidal finite-amplitude concentration disturbances in time for x=0.87,2.04,3.22,4.47 from bottom to top shifted in order to be presented by Lammers *et al.* (1996) [117] on a single picture T=2.176 $\Phi_0 = 0.06$ (Reprinted with the permission of Cambridge University Press)

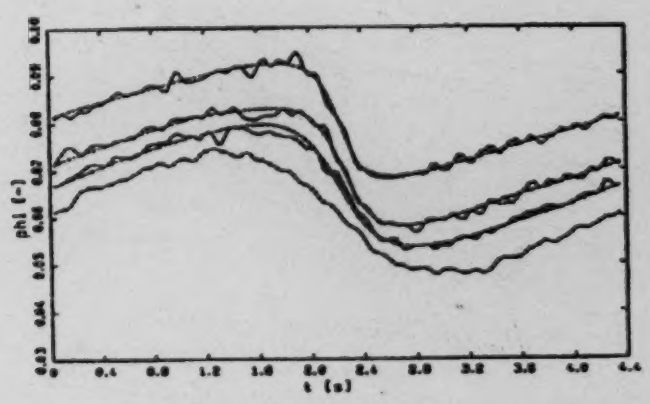

Figure 5.19: The evolution of sinusoidal finite-amplitude concentration disturbances in time for x=0.87,2.04,3.22,4.47 from bottom to top shifted in order to be presented by Lammers *et al.* (1996) [117] on a single picture T=4.352 $\lambda = 0.0$ $\Phi_0 = 0.06$ (Reprinted with the permission of Cambridge University Press)

The quantitative comparison between Figs. 5.16 and 5.18, and between Figs. 5.17 and 5.19 is not easy since the experimental framework and the simulations were not performed exactly under the same conditions. First, the simulations presumed a periodic cubic domain, while the experiments were performed in a cylinder (equivalent to non-slip boundary condition on the walls) and a sinusoidal, time-dependent, wave profile at the inlet. Also the disturbances in the void fraction were generated by simultaneously changing the air and water flow rates, such that the total volume flow rate was kept constant. For the shortest periods used, Lammers *et al.* (1996) varied the flow rates rather than the void fraction sinusoidally. The figures 5.18 and 5.19 illustrate the wave profiles recorded at (from bottom to top) 0.87 m, 2.04 m, 3.22 m and 4.47 m above the inlet of the pipe. The last three profiles had been vertically shifted in order to be presented in the same figure. In each case the superficial liquid velocity is 0.03 m/s and the mean volume concentration is 6%. The wave periods are 2.176 s in Fig. 5.18 and 4.352 s in Fig. 5.19.

The experimental results of Lammers *et al.* (1996) indicate the following distinctive features of these nonlinear waves:

(i) Waves with higher frequencies are more strongly dissipated, which means that $\Delta\Phi$ decreases with the height of the measuring station.

(ii) The slope S of the nonlinear wave can increase at low frequencies with the height of the measuring station. The cause of the second effect seems to be the increase in the void fraction due to the growth of the bubbles, triggered by the decrease of the hydrostatic pressure along the column. However, this effect was not initially included into our model since we solved a pure advection equation for the void fraction. Lammers *et al.* (1996) introduced a term $\lambda\Phi$ in their generalized Burgers' equation corresponding to signalling problems to account for the increase of the void fraction. λ is a positive function of the height. It is difficult to determine what term in the original model should be included in order to give rise to such term in the Generalized Burgers' Equation. Lammers *et al.* (1996) suggested to add a term $\lambda\Phi v$ to the first continuity equation (4.6) and subtract it from the second one, (4.7). The magnitude of λ is hard to be determined in the present setting and we did not try to fit the experimental results. Such a term, however, can have a significant influence and therefore it will be studied in more detail in a future study.

The first feature (i) is clearly demonstrated in Figs. 5.17 and 5.16. Fig. 5.17 corresponds to a wave with a period of 4.352 s and it is much less dissipated than the wave in Fig. 5.16,

which has a period of 2.176 s. The ratio between the wave strength $\Delta\Phi$ of the initial and last wave in Fig. 5.16 is approximatively 2.85. The same ratio in Fig. 5.17 is almost 1. The corresponding ratios in the experimental results in Figs. 5.18 and 5.19 are approximatively 2.75 and 1.6. The agreement between the results at high frequencies ($T = 2.176\ s$) is very good. The difference between our results and the experimental measurements can be attributed to the loss of hydrostatic head along the bubble column that is hard to be accounted for in a periodic domain.

Another distinctive feature that was first noticed by Lammers *et al.* (1996) was that in the case of high frequencies the wave amplitude at the upper measuring station has become nearly independent of the signal amplitude (see Fig. 5.18) The wave profile is typical for waves in the final stage of decay. We reached the same conclusion in our simulations (see Fig. 5.16).

So far we tried to simulate the void fraction nonlinear wave propagation phenomena in a three-dimensional periodic domain. However, the experiments were performed in a tall cylindrical column. In order to be as close as possible of the experimental framework, we repeated the simulations in a real bubble column. We used the following boundary conditions: the inlet void fraction profile was prescribed and it had the form

$$\tilde{\Phi}(\hat{x},\hat{y},\hat{z}=x_1,\hat{t}) = \frac{\hat{t}}{T}\Delta\tilde{\Phi} + \tilde{\Phi}_0 - \frac{1}{2}\Delta\tilde{\Phi} - \frac{1}{2}\,\Delta\tilde{\Phi}\,\tanh(\frac{2}{S}(\hat{t}-\frac{T}{2})),$$

$$\hat{t}\in[0,T],$$

$$\Delta\Phi = 0.05 \quad T = 4.352 \quad S = 1.263.$$

$$\Delta\Phi = 0.05 \quad T = 2.176 \quad S = 0.526.$$

The horizontal components of both the gas and the liquid velocities at the inlet were set to zero. The vertical liquid velocity at the inlet had a parabolic profile so that the liquid velocity at the wall to vanish and the average inlet liquid velocity was multiplied by the inlet void fraction to be equal to the experimental liquid superficial velocity of 0.03 m/s. The gas velocity at the inlet was chosen so that the mixture velocity to remain constant in time, since that's how the experiments were performed. At the wall, the non-slip boundary conditions were imposed for the liquid phase. Neumann boundary conditions were prescribed for the gas phase and the void fraction was not prescribed at the wall. The outlet was assumed a free surface.

Lammers *et al.* (1996) noticed experimentally that the bubbles increase in size in the upper part of the column. This behavior is due to the loss of hydrostatic head. Therefore, in

tall columns, this effect must be taken into consideration in order to be closer to the experiment. Since in our model, the densities of both the gas and the liquid are assumed constant (incompressible case), we add mass mass through the system to the continuity equation for the gas by introducing a growth factor. The modified continuity equation for the gas is:

$$\frac{\partial \Phi}{\partial t} + \nabla \cdot (\Phi \mathbf{v}) = \lambda \Phi \mathbf{v}, \tag{5.22}$$

where

$$\lambda = \frac{\rho_l g(1-\Phi_m)}{p_l},$$
$$p_l(z) = P_a + (1-\Phi_m)\rho_m g(H-z).$$

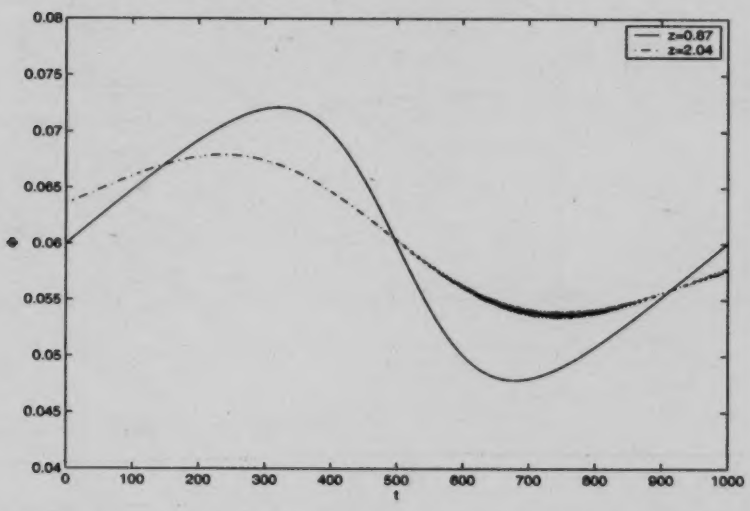

Figure 5.20: The void fraction profile in the z direction at z=0.87,2.04 when the period T=2.176 $\Phi_0 = 0.06$

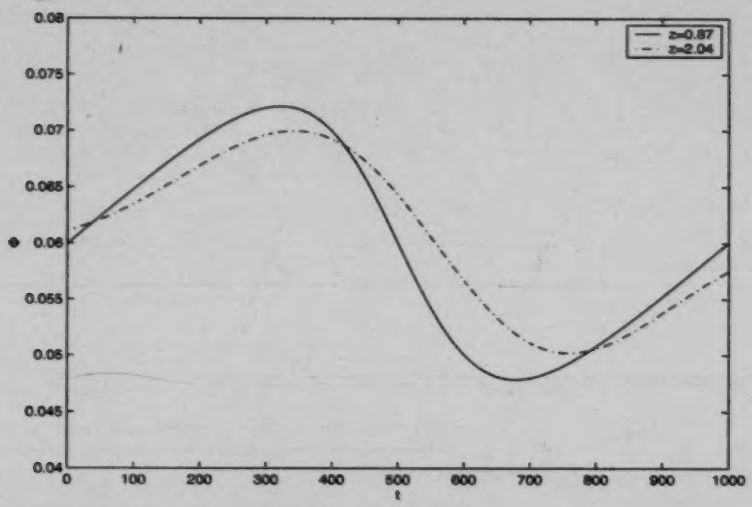

Figure 5.21: The void fraction profile in the z direction at z=0.87,2.04 when the period T=4.352 $\Phi_0 = 0.06$

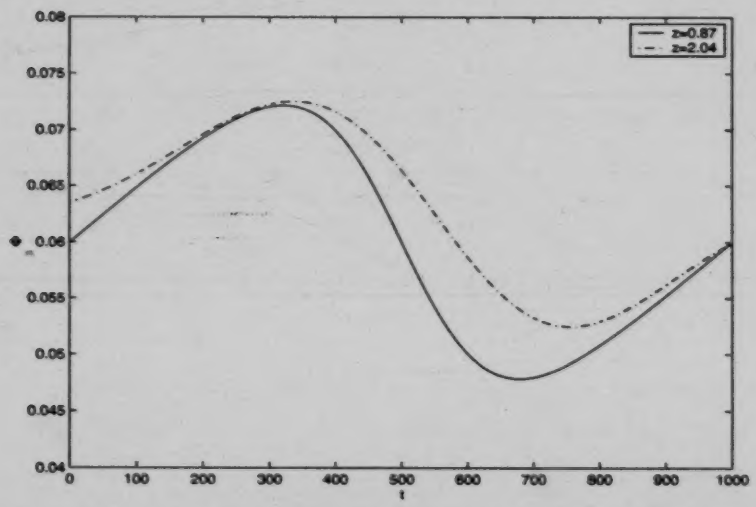

Figure 5.22: The void fraction profile in the z direction at z=0.87,2.04 when the period T=4.352 $\Phi_0 = 0.06$ when the growth factor term was included in the model

Chapter 6

Model validation

In the previous chapter we validated the new expression of the bulk modulus of elasticity, providing comparison with the void fraction wave propagation experiments of Lammers *et al.* (1996). This chapter provides validation of our numerical scheme.

By numerical simulations we came to the conclusion that the numerical scheme without stabilization is not stable within the range of parameters we expected. That was the reason we modified the finite element method by introducing two stabilization terms in the weak formulation of the discrete problem: one term is called the stabilization term and it acts as a filter. It basically denoises the velocity and void fraction profiles, in other words it compensates for the numerical noise. The other term is called the shock capturing term and it deals with shock discontinuities. Every time the solution is on the brick of getting discontinuous, therefore every time the gradient of the void fraction or of any of the velocity fields becomes steep, it introduces some diffusion around the shock only, so that the numerical scheme does not lose its stability. In this way, we show how a continuous model can deal with shock discontinuities without having to introduce a discontinuous Galerkin formulation in our problem.

The sedimentation problem was chosen as test case for the numerical scheme especially because, despite its easy formulation, is a very hard problem numerically. Not only that it deals with a discontinuous solution, but the discontinuity travels within the domain. If the discontinuity had been static and known a-priori, than the classical grid refinement around the discontinuity and the discontinuous Galerkin formulation would have been more appropriate numerical tools.

6.1 Sedimentation problem

This section of chapter 6 has already been presented elsewhere.[1] In the book [85], the following benchmark test problem was given:

$$\frac{\partial \Phi}{\partial t} + \nabla \cdot (\Phi \mathbf{v}) = 0, \tag{6.1}$$

$$\frac{\partial (1-\Phi)}{\partial t} + \nabla \cdot ((1-\Phi)\mathbf{u}) = 0, \tag{6.2}$$

$$\Phi \rho_2 \frac{D_{\mathbf{v}}\mathbf{v}}{Dt} = -\Phi \nabla p - \xi(\Phi)\nabla\Phi - \beta(\Phi)(\mathbf{v}-\mathbf{u}) + \Phi\rho_2\mathbf{g} - \Phi\rho_1\mu(\Phi)\frac{D_{\mathbf{v}}(\mathbf{v}-\mathbf{u})}{Dt}, \tag{6.3}$$

$$(1-\Phi)\rho_1 \frac{D_{\mathbf{u}}\mathbf{u}}{Dt} = -(1-\Phi)\nabla p + \xi(\Phi)\nabla\Phi + \beta(\Phi)(\mathbf{v}-\mathbf{u}) + (1-\Phi)\rho_1\mathbf{g} + \Phi\rho_1\mu(\Phi)\frac{D_{\mathbf{v}}(\mathbf{v}-\mathbf{u})}{Dt}, \tag{6.4}$$

The coefficients used for this case, as stated in [85], are:

$$\mu(\Phi) = \frac{1}{2}\frac{1+2\Phi}{1-\Phi},$$

$$\beta(\Phi) = c_f((1-\Phi)\rho_1 + \Phi\rho_2)(1-\Phi)\Phi,$$

$$g = -\frac{1}{2}\frac{\rho_1+\rho_2}{\rho_1-\rho_2},$$

$$\xi(\Phi, v, u) = \rho_2\xi_1(v_3-u_3)^2,$$

$$c_f = 1 \quad \xi_1 = 1.$$

The equations are one-dimensional, in the sense that the velocity vector fields have one component only. Since our code is three-dimensional, in order to simulate this case we assumed the domain to be a very thin parallelepiped. The dimensions are : width = 0.025 , depth = 0.025, height = 2.0. In this way, the x and y dimensions are negligibly small compared to the vertical component and the case can be approximated with the one-dimensional one. We assumed periodic boundary conditions in x and y directions and prescribed inlet and outlet boundary conditions in the z direction. The domain was discretized using: $\Delta x = 0.00625$, $\Delta y = 0.00625$, $\Delta z = 0.00625$.

The sedimentation process is very easy: it starts with the heavier phase on top and, due to gravity, the lighter phase gradually moves in the upper half of the column, while the heavier phase moves to the bottom. In other words, the two-phases swap their positions in space. If

[1] A variant of this section was presented at [29].

this case is to be simulated, the following problem arises: first the velocity of the lighter phase is non-zero at the bottom and the velocity of the heavier phase can be considered zero and gradually the reversed situation happens. Since we don't know a-priori how these velocities will change in time and we still want to prescribe them on top and on the bottom, we eliminated these complications with the boundary conditions by starting with a slightly sedimentated case, in the sense that we assume that the sedimentation process has already begun and we want to see if we can simulate how the phases separate totally. The initial conditions of our simulations are:

$$\Phi_0[z] = \begin{cases} 0\,, & \text{if } z \in [0, \frac{1}{4}], \\ \frac{1}{2}\left(1 - e^{1 - \frac{1}{1-(4(z-\frac{1}{4}))^2}}\right), & \text{if } z \in [\frac{1}{4}, \frac{1}{2}], \\ \frac{1}{2}\,, & \text{if } z \in [\frac{1}{2}, \frac{3}{2}], \\ \frac{1}{2}\left(1 + e^{1 - \frac{1}{1-(4(\frac{7}{4}-z))^2}}\right), & \text{if } z \in [\frac{3}{2}, \frac{7}{4}], \\ 1\,, & \text{if } z \in [\frac{7}{4}, 2]. \end{cases}$$

The following pictures clearly illustrate that our numerical scheme can capture the one-dimensional sedimentation without introducing artificial diffusion everywhere. The diffusion is introduced only around the moving shock and is just enough to prevent the wave from breaking without dampening the shock. If we analyze the results produced by Coquel (see Fig. 6.5), we see that the way their solver reaches the steady state is quite artificial (see the profile obtained at $t = 0.5$ s). This happens because in their solver, they introduce a diffusion term that acts everywhere in the domain. Also, at $t = 10s$ in Fig. 6.5, the final sedimentation state is not as accurately reproduced as in Fig. 6.4. Their void fraction profile is more diffused.

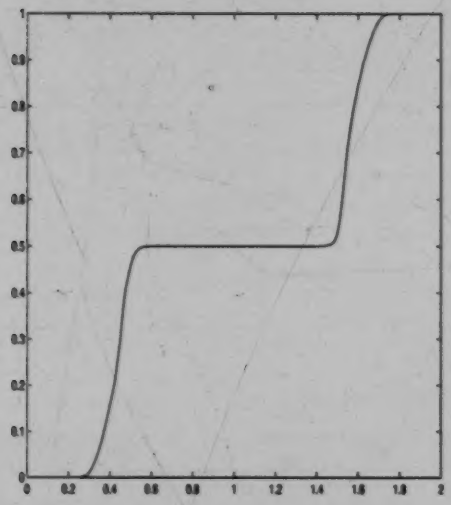

Figure 6.1: The void fraction profile after 50 iterations (x axis: vertical direction, y axis: Φ)

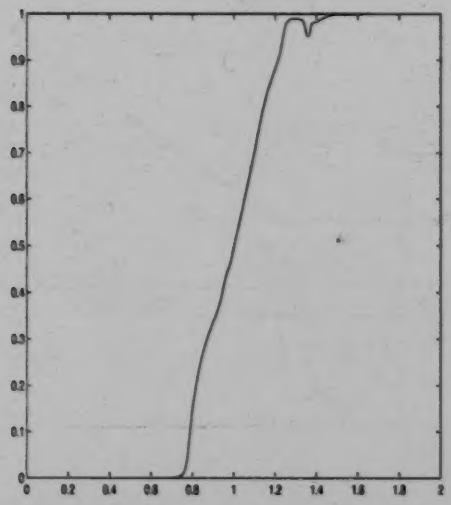

Figure 6.2: The void fraction profile after 1000 iterations (t = 1) (x axis: vertical direction, y axis: Φ)

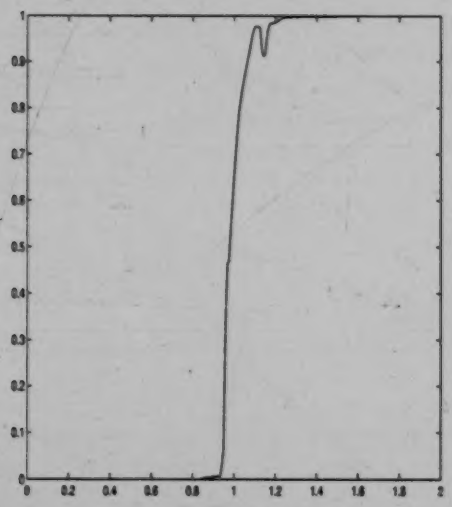

Figure 6.3: The void fraction profile after 1500 iterations (t = 1.5) (x axis: vertical direction, y axis: Φ)

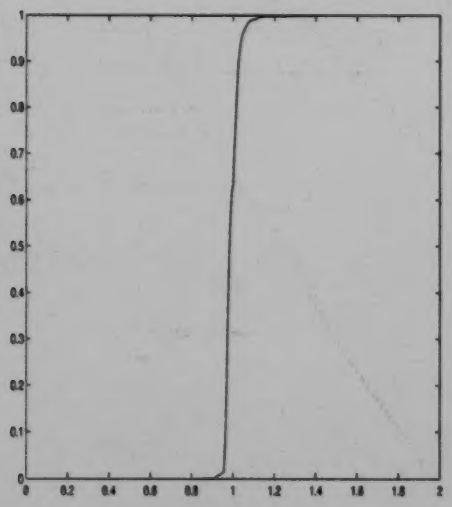

Figure 6.4: The void fraction profile after 2000 (t = 2.0) iterations (x axis: vertical direction, y axis: Φ)

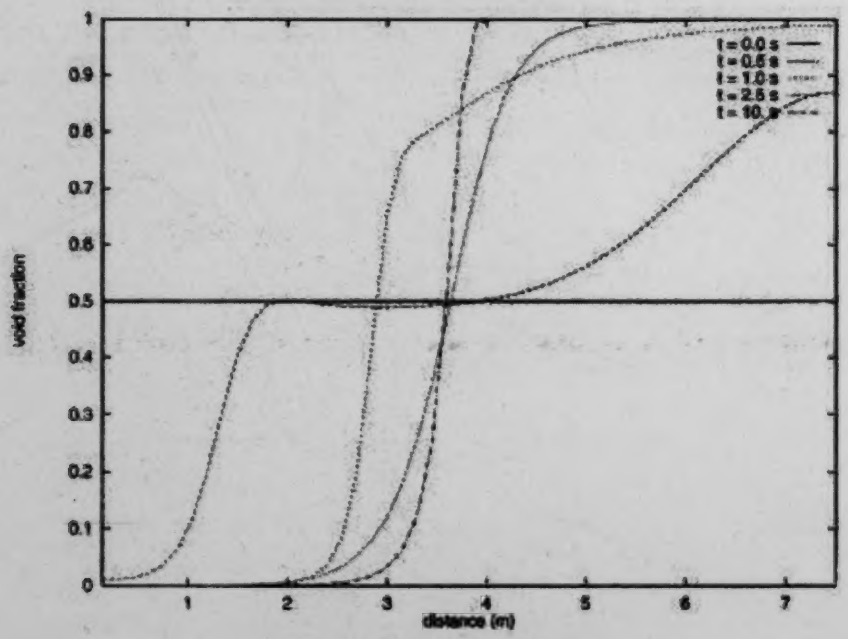

FIG. 3. Void fraction history, 50 cells.

Figure 6.5: The void fraction profile prescribed by Coquel [44] "Reprinted from [44], Copyright (2005), with permission from Elsevier"

However, we must bear in mind that this type of sedimentation happens only in the one-dimensional case and it was chosen as test case for validation of our numerical scheme only. The two- and three-dimensional sedimentation are very different from the one-dimensional case. That is the reason no one-dimensional theory (see chapter 5 of the thesis) can replace truly three-dimensional simulations. What happens in the three-dimensional case can be very different from the one-dimensional situation. If sedimentation is to be simulated in the two-dimensional case, for instance, the Rayleigh-Taylor instability phenomenon occurs at the interface. Therefore, the interface is no longer stable. That is the reason our next test case is three-dimensional.

6.2 Circulation flow in a viscous fluid. Comparison with Durst's case

The results presented in this section have already been presented elsewhere.[2] In this section we chose to compare our numerical results with the experiments by Durst et al.(1984) [61] of a bubble-driven laminar flow in an axisymmetric cylindrical column. The reason we stopped at this set of experiments was that the authors provided detailed local information on bubble size and bubble velocity, as well as local liquid velocity. They had eight measuring stations throughout a relatively short column, which meant that the simulations could be closely compared with the experiments. That is very rarely the case. The geometric configuration was: diameter = 0.1 m, height=0.098 m. The liquid used in the experiments was castor oil (density=960.3 kg/m^3, kinematic viscosity=0.699*10^{-3} m$^2/s$). Due to its high viscosity, the velocity fluctuations are damped and the flow is more stable than it would have been if water had been used instead. That guaranteed a laminar liquid flow and also non-spiral motion of the rising air bubbles. The air was supplied through a 0.5 mm diameter nozzle located on the axis of the cylinder. The bubbles had diameters within the range 5-6.5 mm. The simulations were performed assuming d_b=6 mm. The boundary conditions used in our simulations are:

Inlet boundary conditions

$$\Phi|_{z=0} = \begin{cases} \Phi_0\,, & \text{for } r \in [0, r_s] \\ 0\,, & \text{if } z \in (r_s, R] \end{cases} \tag{6.5}$$

$$\Phi_0 = 0.12$$

$$\mathbf{u}|_{z=0} = 0$$

$$v_z|_{z=0} = 0.4 * v_{max}$$

$$v_{max} = 3.09 cm/s$$

$r_s = 0.25$ mm and $R = 0.05$ m stand for the radius of the nozzle and of the column.

Side wall boundary conditions

$$\mathbf{u}|_{r=R} = 0$$

$$v_x|_{r=R} = 0, v_y|_{r=R} = 0$$

[2] A variant of this section was presented at [29].

Outlet boundary conditions

$$u_z|_{z=H} = 0$$

$$p|_{z=H} = 0$$

The mesh consisted in 29 horizontal planes, each of $1601 (= 41^2)$ nodes.

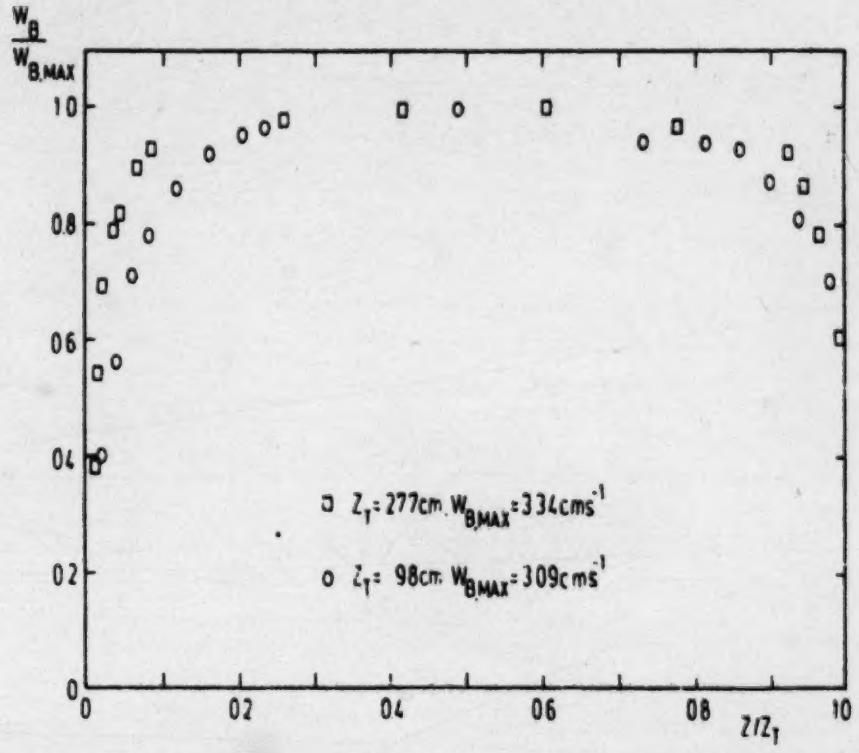

Figure 6.6: Axial (center-line) development of bubble velocity for two liquid heights "Reprinted from Durst *et al.* (1984) [61], Copyright (2005), with permission from Elsevier"

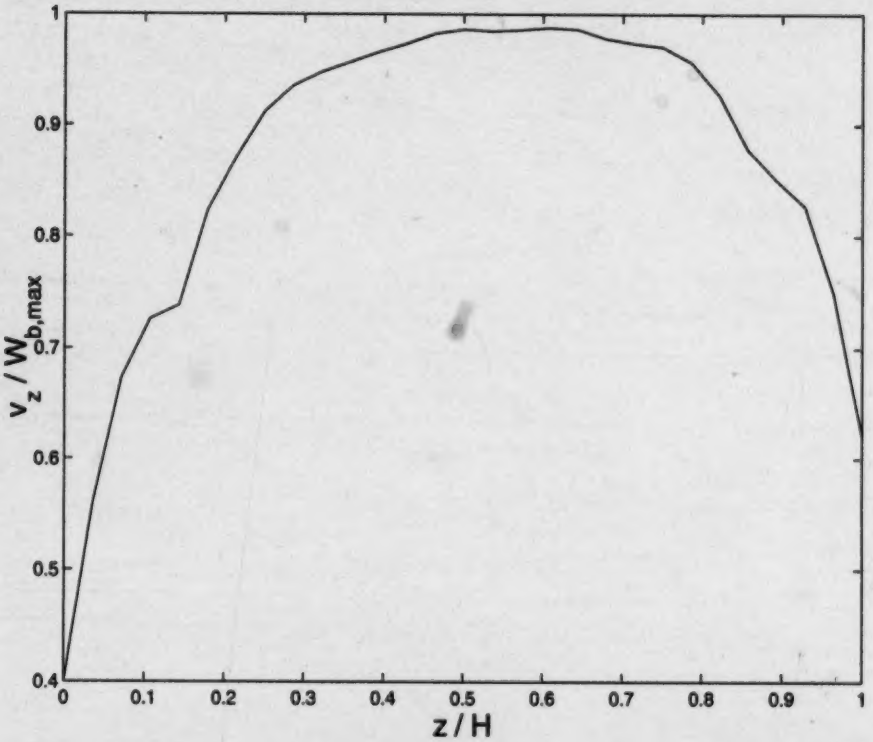

Figure 6.7: Axial (center-line) development of gas velocity for liquid height = 9.8 cm

The axial variation of the bubble velocity is presented by Durst for two liquid heights. We only simulated one case. The maximum velocity attained experimentally is $W_{B,max} = 3.09$ cm/s. Our maximum velocity is almost equal to 1 in Fig. 6.7. This value is dimensionless. The dimensioned value is exactly 3.09 cm/s because this is the value of the velocity we used to non-dimensionalize the equations. Also the shape of the profile presented in Fig. 6.7 is similar to the one given in Fig. 6.6.

Detailed liquid-velocity profiles were measured at eight locations. The radial profiles of axial velocity (see Fig. 6.8 and Fig. 6.9) reveal that the maximum liquid velocity that was measured experimentally was about one half that of a bubble, with a very rapid radial decay of velocity away from the rising bubbles, showing that the liquid in the immediate vicinity of the bubbles undergoes large shear. The flow is clearly recirculating and, as expected, the negative velocities are about one tenth of the magnitude of the positive ones. Once again, our numerical results fit the experimental measurements closely. As Durst et al.(1984) [61] concluded, the difference in the magnitudes is expected in axisymmetric geometries, because

the negative velocities can flow over much larger areas than can the positive velocities.

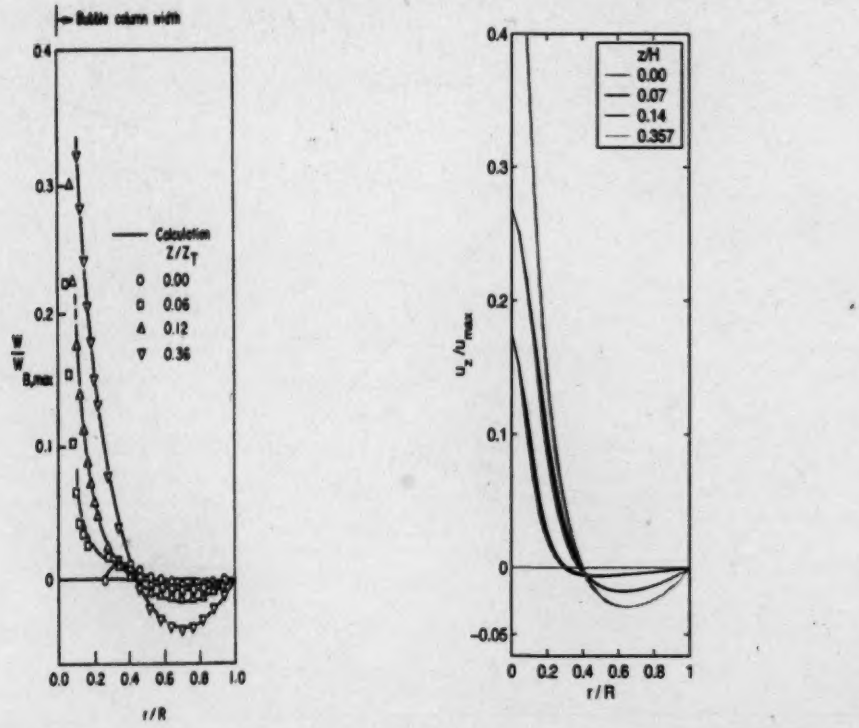

Figure 6.8: Profiles of the liquid axial velocity at successive axial stations (lower half of the cylinder) "Reprinted from Durst *et al.* (1984) [61], Copyright (2005), with permission from Elsevier"

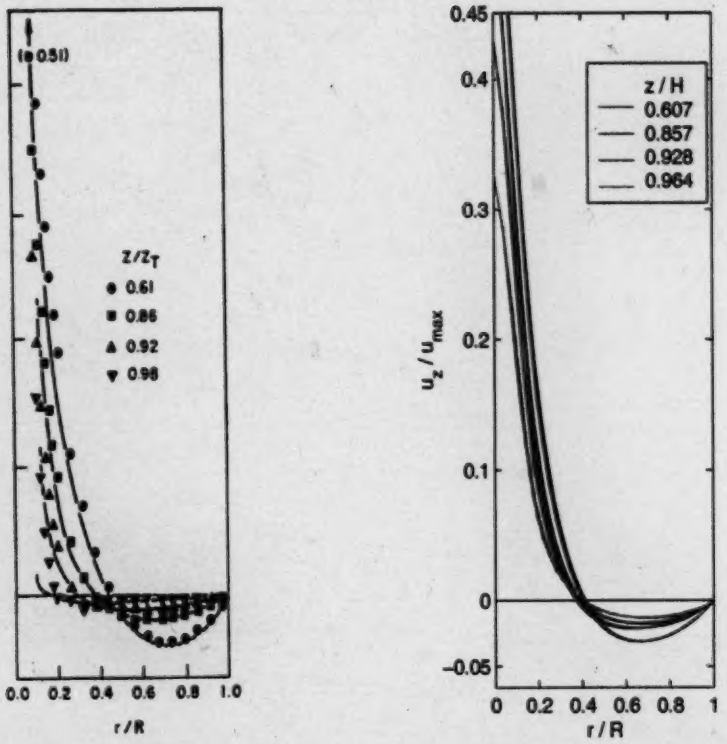

Figure 6.9: Profiles of the liquid axial velocity at successive axial stations (upper half of the cylinder) "Reprinted from Durst *et al.* (1984) [61], Copyright (2005), with permission from Elsevier"

A comparison of the radial velocity profiles measured experimentally and our numerical simulations can done by looking at Fig. 6.10 and Fig. 6.11. Particularly large values occur near the free surface as the axial liquid flow, carried along by the bubble street, approaches the free surface and is deflected radially. Our liquid velocity profiles clearly show that the flow is axisymmetric. As it can be seen in Fig. 6.10 and Fig. 6.11, the deviation from symmetry is minimum, since the velocities computed throughout the domain at a fixed height and a fixed radial distance (x and y components are on the same circle for different points but they represent different spatial positions), yield almost the same values. Notice that more profiles for different radial directions at the same z-pozition are plotted on top of each other.

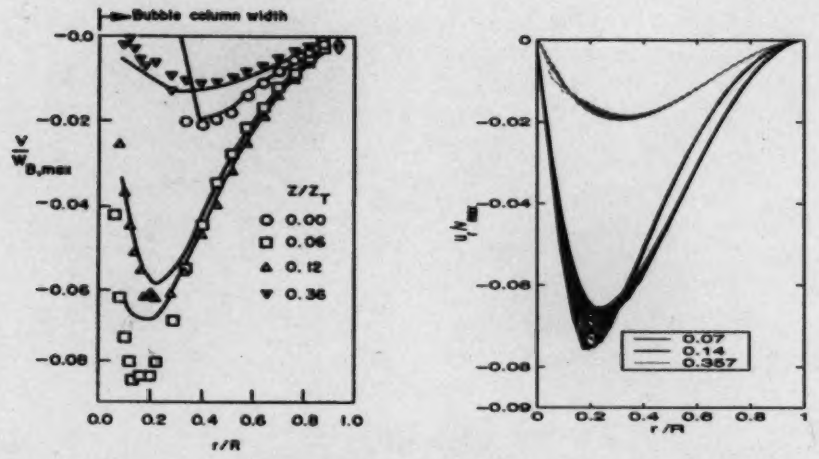

Figure 6.10: Profiles of the liquid radial velocity at successive axial stations (lower half of the column)"Reprinted from Durst *et al.* (1984) [61], Copyright (2005), with permission from Elsevier"

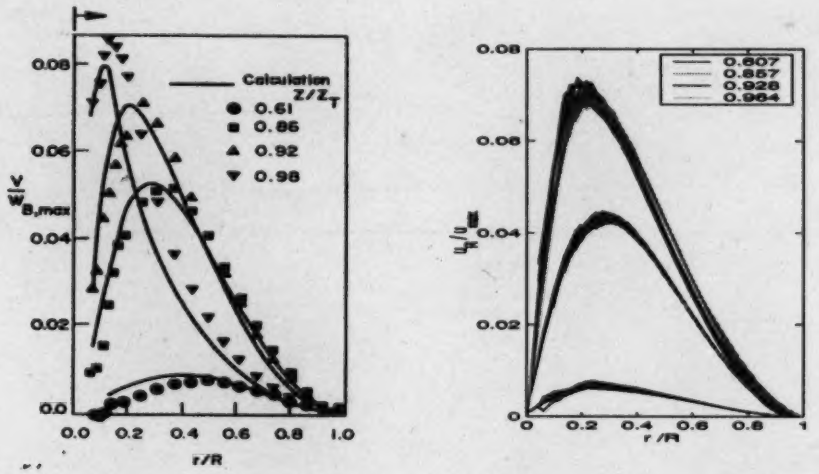

Figure 6.11: Profiles of the liquid radial velocity at successive axial stations (upper half of the column) "Reprinted from Durst *et al.* (1984) [61], Copyright (2005), with permission from Elsevier"

The flow reaches the classical steady state with two large circulation cells distributes along the height of the column both experimentally and numerically, as it can be seen clearly in Fig. 6.12. The steady profile is shown in Fig. 6.13.

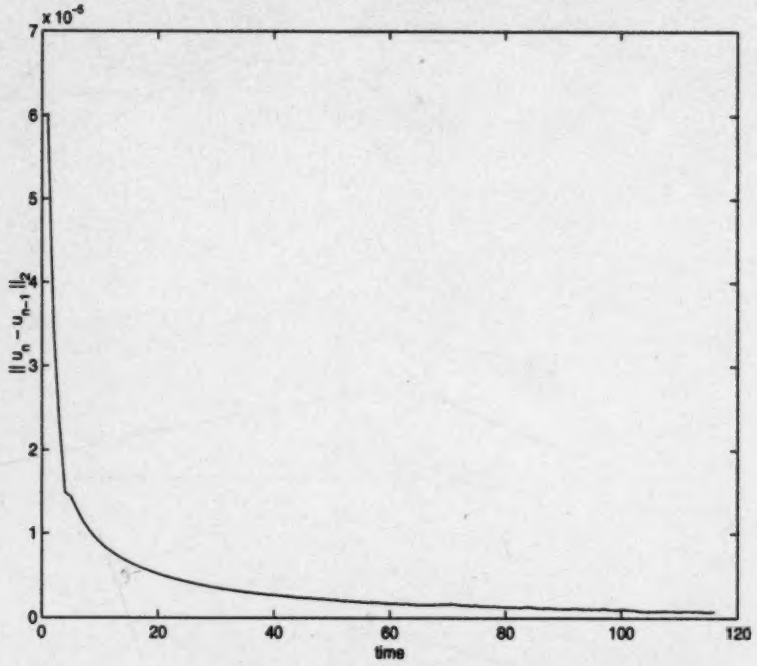

Figure 6.12: The Euclidean norm of two consecutive velocities in time

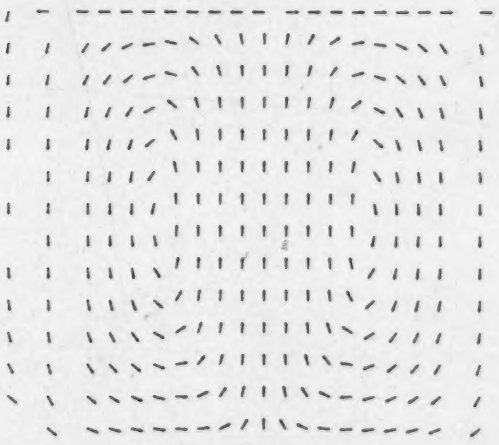

Figure 6.13: Liquid velocity vector field after the flow reaches the steady state.

6.3 Coherent structures in a two-dimensional bubble column

So far, we tested our numerical scheme on a void fraction wave propagation problem, the one-dimensional sedimentation problem and the golf-stream circulation problem in a viscous fluid. The sedimentation problem showed that our continuous formulation of a problem dealing with discontinuous solutions gives very accurate results due to the small diffusivity introduced around the discontinuity by the shock capturing term. The circulation problem in a viscous fluid treated the case where the diffusivity dominated the convective terms. The situation that was not covered yet was the case of convection dominated flows. Among all the cases, this is by far the most challenging one. Most of the numerical methods are especially designed to solve only one specific type of the above problems. Even though the performance of a numerical scheme as ELLAM, for instance, that deals specifically with convection-dominated flows is expected to outperform our numerical scheme, we would like to see how well, if at all, our numerical scheme can capture the highly dynamical convective vortices that appear in two and three-dimensional bubble columns.

For this purpose we chose as a test case the experiments of Borchers et al. (1999) [21]. Even though this is an academic example, which deals with the case of a locally aerated flat bubble column, operated at low gas throughput, this example has proved to be crucial for the evaluation of the two-phase flow models and numerical schemes since it is extremely sensitive to small changes in model assumptions and it is highly dependant on the accuracy of the numerical method. Actually, there is a series of papers that attempt to match the experiments of Sokolichin and Eigenberger (1999) [171]. They are identical with the experiments of Borchers et al. (1999) [21] except for the fact that their frit sparger is located laterally and the Borchers's paper deals with the case of a symmetrically aerated flat bubble column. The reason we chose to simulate this case is because in this set of experiments they monitored the time-dependant behavior of the flow in two points instead of only one and they also present their phase portraits, allowing us to compare both the vertical and horizontal amplitudes of the liquid velocities in the measuring points.

This is a pseudo-two dimensional case since the third dimension is much smaller than the other two. The dimensions of this thin parallelepipedic box are: width = W = 50cm, depth = D = 8cm, height = H = 200cm. The aerated inlet area is 4 cm in diameter and it is placed at the center of the inlet. The column is filled with water to yield three different aspect ratios: $H/W = 1$, $H/W = 2$ and $H/W = 3$ Two gas flow rates, of 1 l/min and 2 l/min were considered. The time-series liquid profiles are illustrated only for the cases $H/W = 1$ and $H/W = 2$. For

the case $H/W = 2$ high-frequency turbulent fluctuations around the mean velocity can be observed, which are of the order of the mean velocity itself. In addition to the high-frequency fluctuations, low-frequency quasi-periodic oscillations of the liquid velocity were measured at both monitoring points indicating the periodic movement of the bubble plume. Our model is laminar, therefore we will compare our numerical simulations with the experimental data after a Fast Fourier Transformation is applied to them in order to obtain signals containing only the low-frequency oscillations. We would like to see if a laminar model can yield the same number of coherent structures as noticed in the experiments. Their number depends on the height to width ratio. We would also like to see if the dynamic, quasi-periodic behavior of the flow can be captured with a laminar model. We are also interested in studying the grid convergence of our laminar model.

The most common approach used by different researchers in modelling this experiment is to use the $k-\epsilon$ turbulent model or its low Reynolds number variant. It seems that the three-dimensional $k-\epsilon$ turbulent model works well in this case. This is the conclusion reached by Sokolichin and Eigenberger (1999) [171], Borchers et al. (1999) [21], Mudde and Simonin (1999) [133], Sokolichin et al. (1997) [172] and Pfleger and Becker [142].

These coherent structures, even though they account for a small fraction of the energy of the turbulence, are probably responsible for a large fraction of the transport of the conserved properties such as mass, momentum and energy. Thus, they are an important component of every turbulent flow and they first appear in the transitional regime from the laminar flow towards turbulence. Even though our goal is not to model or simulate turbulence,we would like to see if we are able to capture these unstable vortical coherent structures using a laminar model. Therefore, even though most researchers apply a turbulent model even when the flow is not in the turbulent regime, we would like to go with a laminar model towards turbulence and try to capture these coherent structures.

The difference between a laminar model and a turbulence model comes in the modelling of the diffusivity. The laminar models have only a laminar viscosity incorporated. The diffusivity term in the turbulent models consists of two parts: one is the classical laminar viscosity and the other one is called the turbulent kinematic viscosity and it is a function of the turbulent kinetic energy k and its dissipation rate ϵ. However, turbulent models are usually derived for the case of one-phase flow and the extension to the two-phase flow case does not have a solid justification. Sokolichin and Eigenberger (1999) [171], Borchers et al. (1999) [21] and other researchers performed two and three-dimensional simulations using both, the laminar model and the $k-\epsilon$ model and they concluded that the only model that works well is the three-dimensional $k-\epsilon$

model. They say that the number of circulation cells resolved by two-dimensional laminar models grows continuously with the spacial resolution. Also, by performing simulations using the 2D $k-\epsilon$ model, the dynamic nature of the flow is not reproduced. This is because the long-time-averaged velocities do not change too much in depth but the high frequency component of the velocity fluctuations does yielding an overestimation of the viscosity in 2D. In their simulations they used the TVD scheme to discretize the advection terms. Becker et al. (1994) [16] used two different grid resolutions in the context of 2D laminar numerical simulations using the upwind scheme. The course grid yielded a stationary result, however the fine grid simulations were able to simulate the desired transient solution. To do so, they increased the laminar viscosity by a factor of 100 to account for the influence of the turbulent viscosity. However, this is an artificial way of forcing the model to get closer to the experimental results and has no physical meaning.

Pan et al. (2000) [138], even though in a different experimental framework, are the only ones, as far as we know, that were able to perform 2D dynamic simulations using a laminar model. To improve their prediction, they introduce a bubble-induced enhancement in viscosity based on the concept of mixing length of Sato et al. (1975) [163].

The common feature of all the above simulations is that, in different ways, they all introduce some extra diffusivity in their model in order to improve, in some cases, or to obtain, in other cases, a dynamic behavior of the bubble plume, and consequently of the liquid phase, close to the experiments. Our model already contains a sort of extra diffusion in the stabilization and the shock capturing terms. The advantage of it is that it is localized around the high gradient fluctuations, so it is not the same for all the points in the grid like in Becker et al. (1994) [16] and also it has a mathematical justification, in the sense that the convergence of the numerical scheme was proven theoretically, even though it was done for a simple convection-diffusion equation.

Our numerical code is a three-dimensional code. To perform 2D simulations, the x-components of the velocities are set to 0. This means that we never compute the x-components of the velocities (we don't advance them in time from level n to level $n+1$). The front and back plane, corresponding to $x = 0$ and $x = 0.16$ (the dimensioned value x=D=8 cm) are treated as symmetry planes. The bottom and side walls are treated as solid walls. This means that the liquid velocity is set to 0 both at the inlet and on the side walls. The gas velocity is prescribed at the inlet and the normal component to the walls are set to be equal to zero. The volume fraction is not prescribed at the walls. At the outlet the pressure is set to zero together with the normal derivatives of the velocity components. Two different meshes are

used: a rough grid consisting of $5 \times 29 \times 52$ nodes and a fine grid consisting of $5 \times 37 \times 52$ nodes. In the experiment, the gas is inserted through a circular frit, therefore breaking the 2D-symmetry. To overcome this inconvenience and to make really 2D simulations, the sparger is assumed to cover the whole depth of the inlet, in other words, $D_S = 8$ cm instead of 4 cm. The inlet gas velocity of the bubbles of the aerated area is fixed at $v_0 = 20cm/s$. Borchers et al. (1999) [21] used two different gas flow rates $\Phi_v = 1$ l/min and $\Phi_v = 2$ l/min. However, the dynamic behavior of the liquid is only depicted for the case $\Phi_v = 1$ l/min probably because the quasi-periodicity recorded experimentally is clearer in that situation. That is why most of our numerical simulations are performed for that case. To arrive at the appropriate driving force, the volume fraction at the aerated inlet area is computed using $\Phi_0 = \frac{\Phi_v}{D_S W_S v_0}$ where D_S is as close as the mesh resolution allows to the width of the sparger, 4 cm.

Let us first analyze the qualitative behaviour of our simulations for $H/W = 1$, $H/W = 2$ and $H/W = 3$.

For the aspect ratio $H/W = 1$ only one circulation cell was obtained in both the present simulation and in the experiment. Three vortices can be observed for $H/W = 2$ and four vortices can be observed for $H/W = 3$ (see Figure 6.14). The instationary nature of flow, due to the meandering motion of the bubble swarm, can be observed both, experimentally and in our numerical simulations. To illustrate the oscillating flow behavior for the cases $H/W = 2$ and $H/W = 3$, we included two different snap shots for each case (see Figs. 6.15, 6.16 and 6.17).

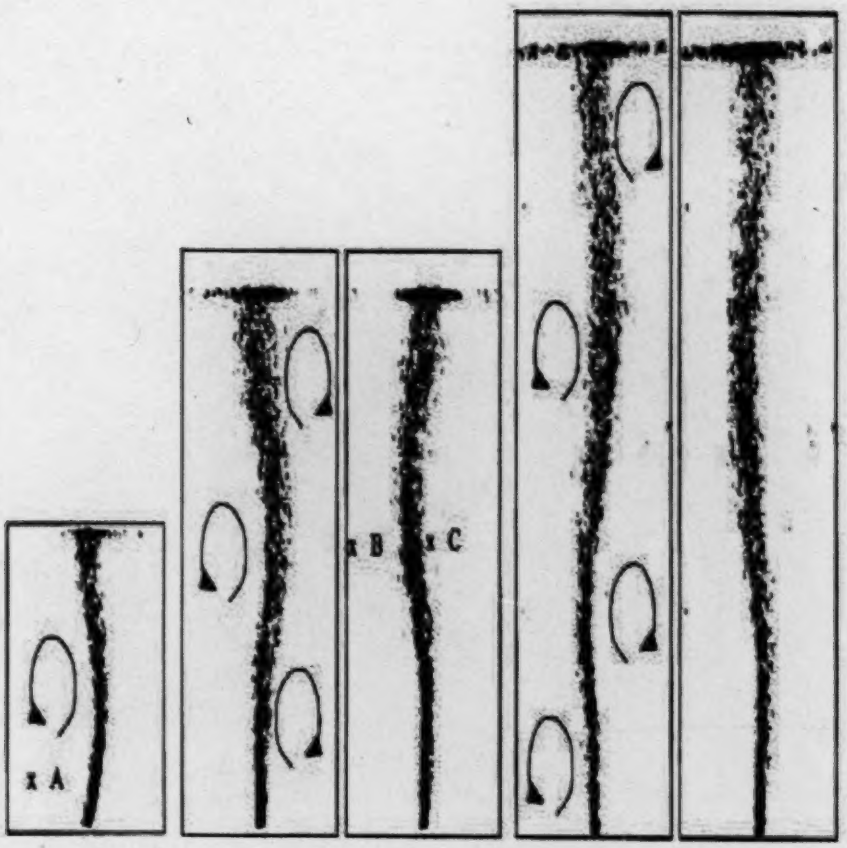

Figure 6.14: Bubble images of the locally aerated flat column, with increasing aspect ratio measured experimentally. Steady state flow at H/D = 1 (a). Oscillating flow behaviour at H/D = 2 (b) and H/D =3 (c) "Reprinted from Borchers *et al.* (1999) [21], Copyright (2005), with permission from Elsevier"

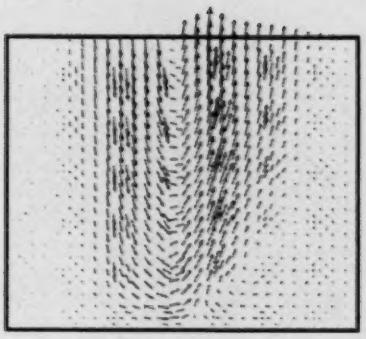

Figure 6.15: Liquid velocity field (steady state) (H/D=1).

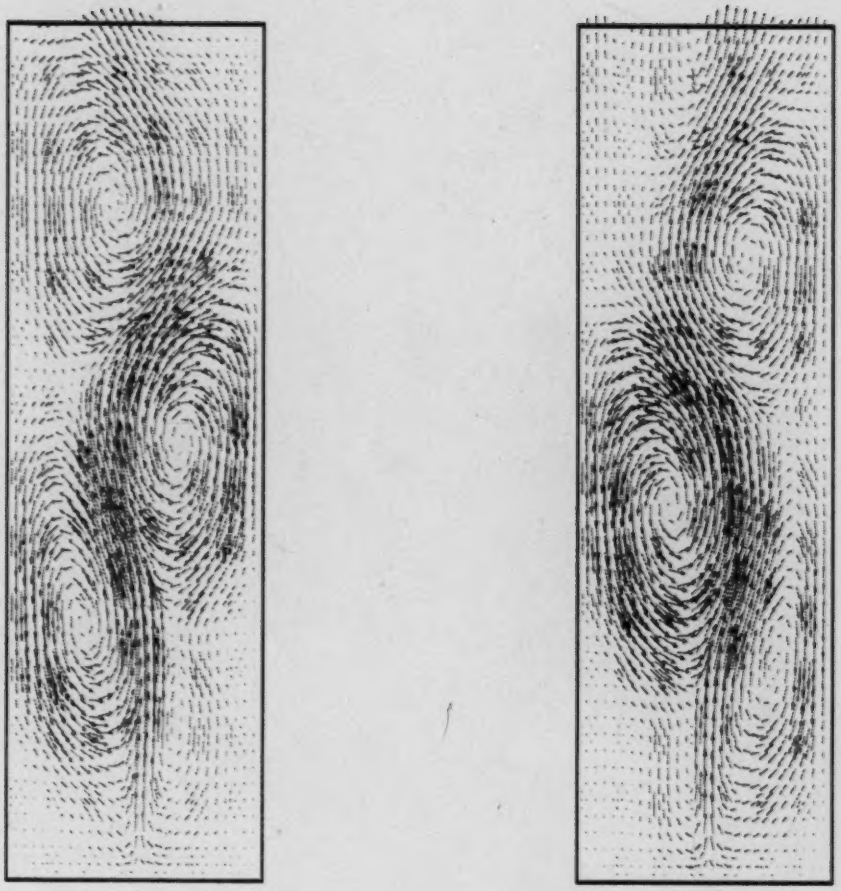

Figure 6.16: Liquid velocity field at 2 different times (H/D=2)

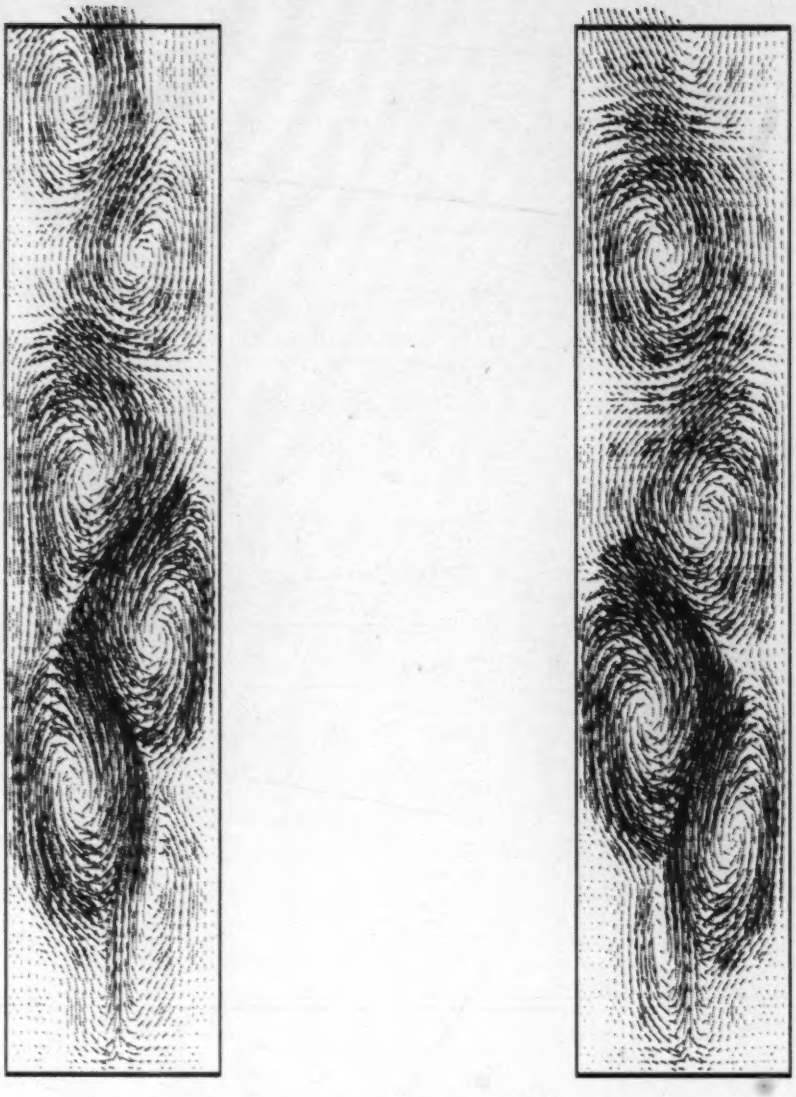

Figure 6.17: Liquid velocity field at 2 different times (H/D=3)

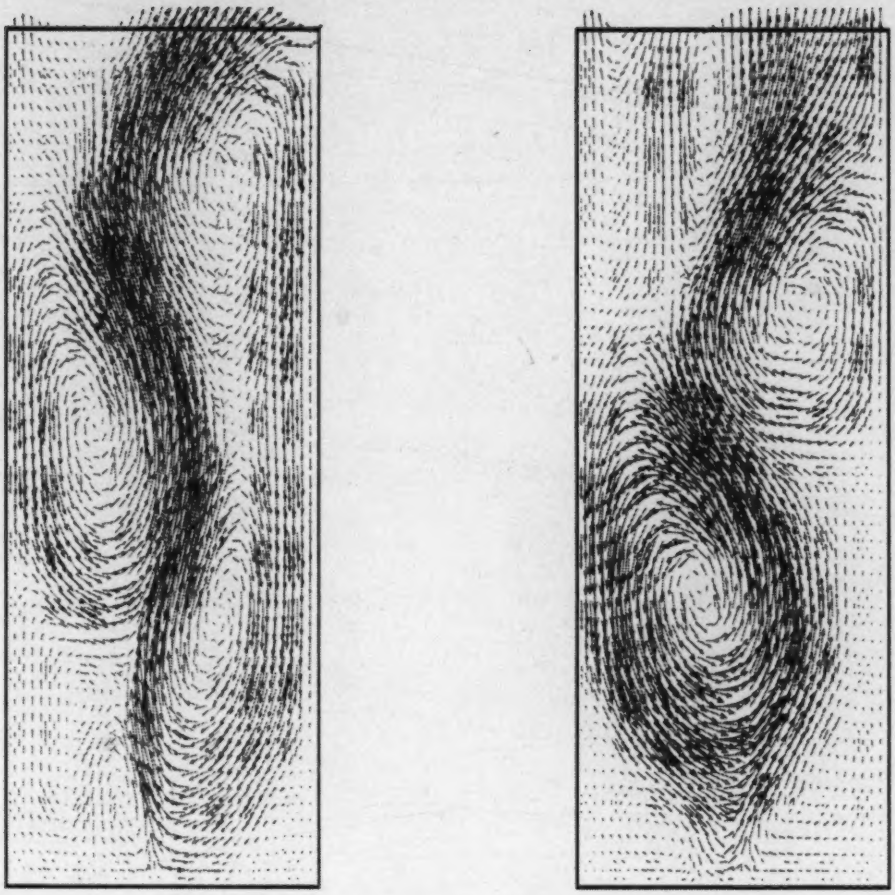

Figure 6.18: Liquid velocity field at 2 different times (H/D=2) (fine grid)

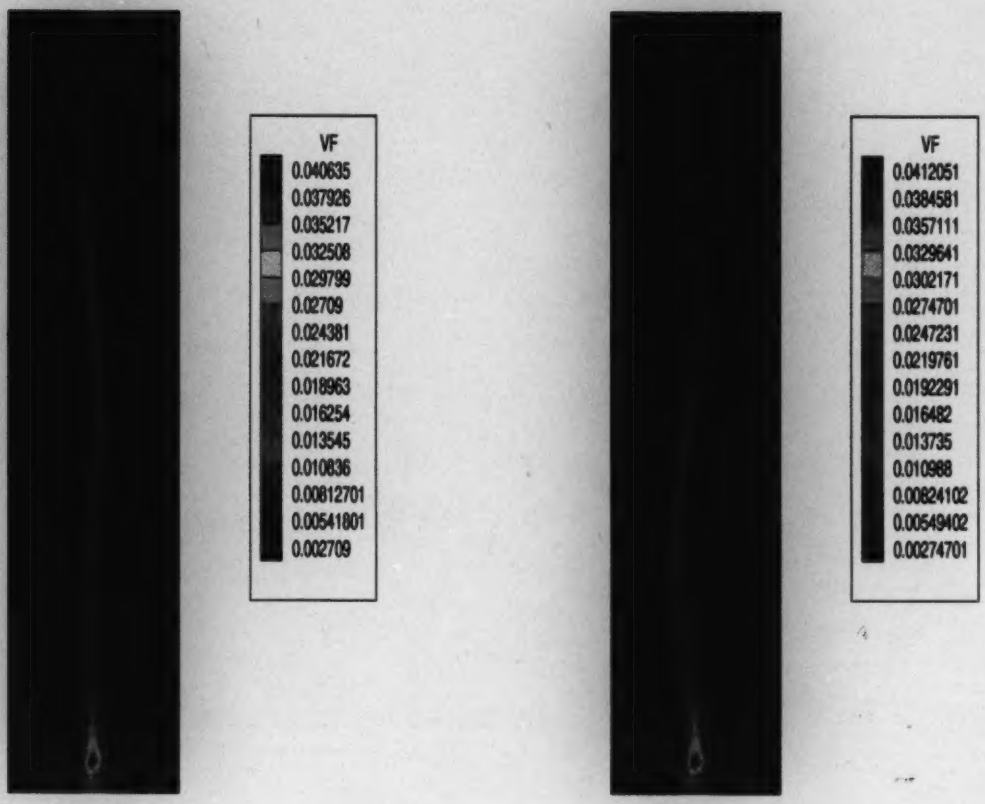

Figure 6.19: Gas hold-up at 2 different times (H/D=2) (fine grid)

Figure 6.20: Gas hold-up (H/D=2)

Using a more refined grid, both the liquid velocity profiles and the meandering of the bubble swarm show a closer resemblance to the experiments (see Fig. 7 of Borchers et al. (1999) [21]). This was illustrated in Figs. 6.18, 6.19 and 6.20.

So far we compared the experiments with our simulations at a qualitative level and we showed that we were able to obtain the same number of vortices and a very similar meandering wave as the one noticed in the experiments.

Now we would like to see if the agreement still holds at quantitative level. In their experiments, Borchers et al. (1999) [21] recorded the time dependent velocity measurements at two different locations: point B(y = 1 cm, z = 50 cm) and point C(y = 25 cm, z=50 cm). Point B is located very close to the wall and at half of the height of the column. Point C represents the

center of the column which means the horizontal coordinate is half the width of the rectangular column and the vertical coordinate is half the height of the column. In our simulations, point C has the same location but point B has its y component slightly modified because B had to be one of the mesh points so its location is as close as possible to the experiments but it depends on the mesh resolution used.

In the experiments, after a transitional period of 40-50 s, the flow becomes quasi-periodic, i.e. one (relatively low) frequency is dominated. We started our simulations on a rough grid of $5 \times 29 \times 53$ nodes first. Even though we don't solve for the x components of the velocities, we must use at least 5 nodes in the x direction because of the way the stabilization terms work: we start from a rough grid and by subdividing each element into subelements we obtain a finer grid. Using this rough grid, the quasi-periodicity is not well captured in the mid point of our domain C. However, close to the wall, the behavior of the flow is more or less periodic. The time-dependent velocity measurements at point C are presented in Fig 6.21. The time-dependant velocity profiles and the phase portrait at point B, close to the wall, show a quasi-periodic behavior (see Figure 6.22). Note that we were able to reproduce the periodic behavior without using any denoising.

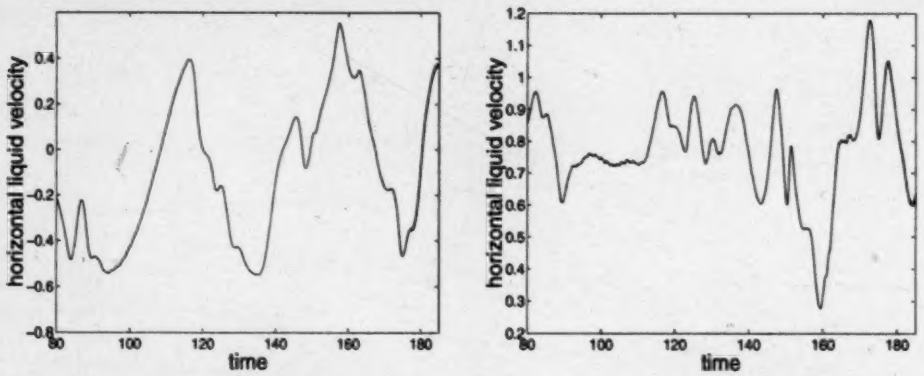

Figure 6.21: Time series of the horizontal liquid velocity to the left and of the vertical liquid velocity to the right at point C

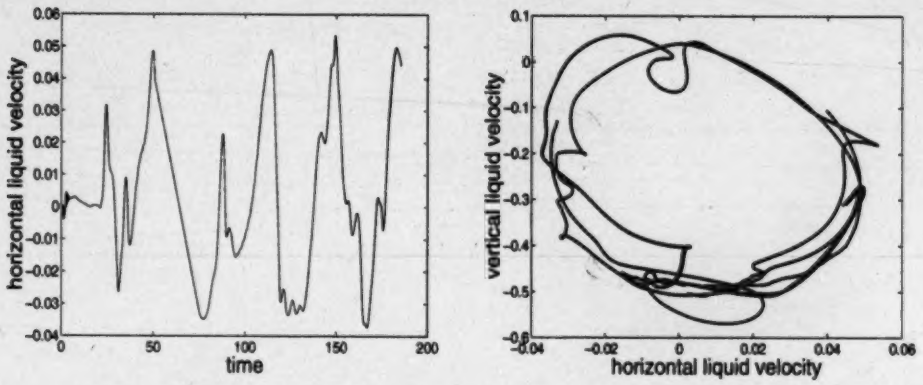

Figure 6.22: Time series of horizontal liquid velocity to the left and the phase-portrait/trajectory of the liquid velocity to the right at point B

Next we used a refined grid of $5 \times 37 \times 53$ nodes. The time-dependent velocity profiles as well as the phase portrait for point C, the central point, illustrate the quasi-periodic behavior of the liquid, induced by the periodic movement of the bubble swarm. This can be seen in Figure 6.24. The velocity is non-dimensionalized in the picture by the velocity of gas at the inlet $v_0 = 0.2m/s$. By analyzing the phase portrait from Figure 6.24 we can see that the horizontal liquid velocity varies within the dimensionless range (-1,1). If we multiply by v_0 this means that the actual range is (-0.2,0.2) m/s. If we compare these values with the ones measured by Borchers et al. (1999) [21] (see Fig. 6.23) we see that we obtain a perfect match. The amplitude of the vertical liquid velocity oscillations in both the experiment and in our case are less than 0.2 m/s. However, our signal is a bit shifted above the horizontal axis corresponding to $u_z = 0$. Also, the period of our oscillations is larger than the one measured experimentally. Nonetheless, the oscillatory quasi-periodic behaviour is well captured and the agreement with the experiments is good, indicating that, with an appropriate numerical scheme, a laminar model can capture the highly unstable, advective vortical structures that represent the first step towards the turbulent flows.

By analyzing the Figure 6.25, we see that our simulations can also capture the quasi-periodic behavior of the liquid close to the solid walls. The phase-portrait is not a perfect circle, but this is neither the case in the experiments. The amplitude of both vertical and horizontal components of the liquid velocities are lower than the experimental values. The reason for this discrepancy is that, unless a really fine grid is used, the boundary layer that appears near the walls cannot be correctly resolved. However, the present result show that a two-dimensional laminar model in conjunction with a proper numerical scheme can capture

the dynamic behavior of the bubble plume.

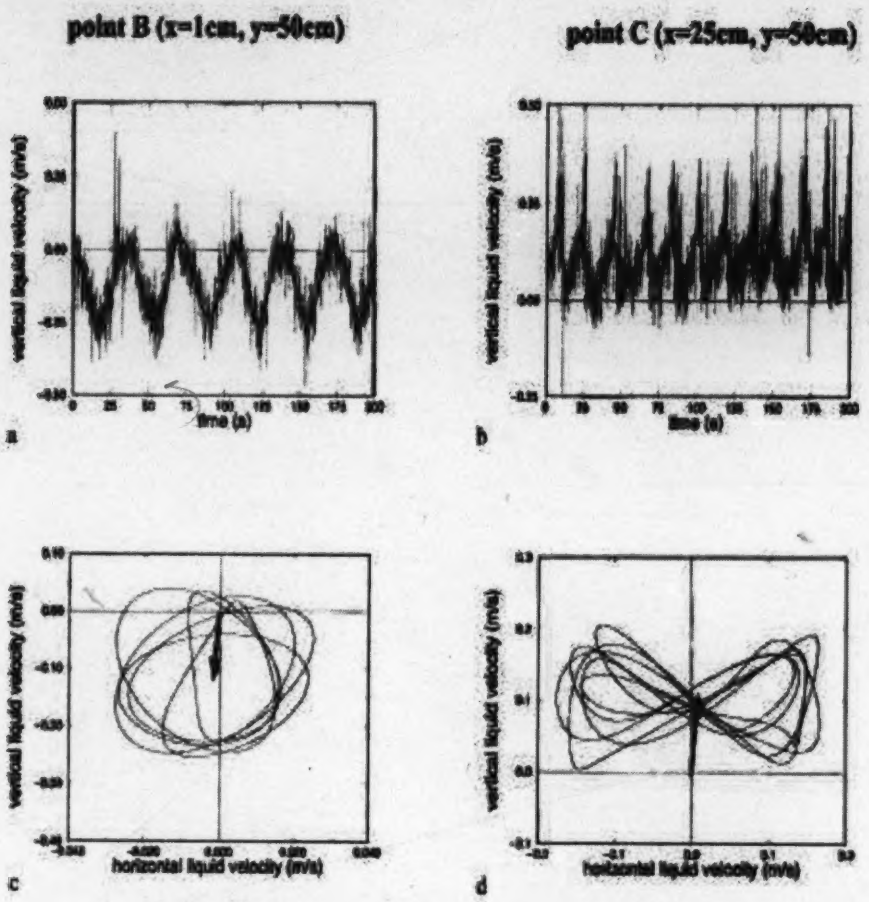

Figure 6.23: Time series of vertical velocities (a/b), raw data (grey curves) and FFT-filtered data (black curves). Trajectories of two-dimensional FFT-filtered velocities (c/d) "Reprinted from Borchers *et al.* (1999) [21], Copyright (2005), with permission from Elsevier"

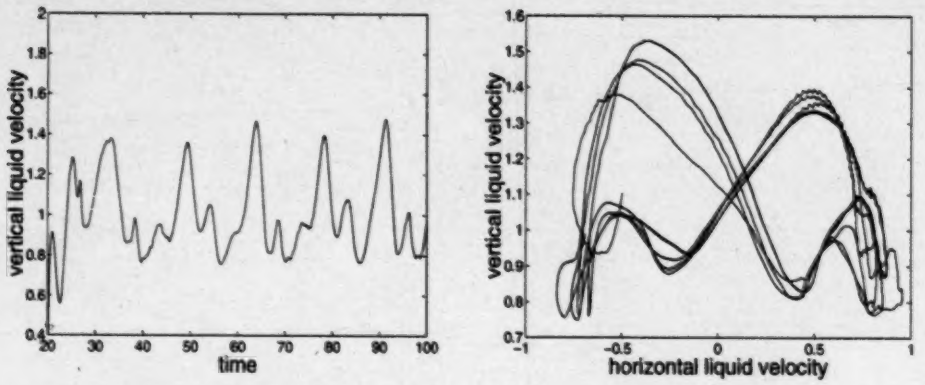

Figure 6.24: Time series of vertical liquid velocity to the left and the phase-portrait/trajectory of the two-dimensional liquid velocity to the right at point C (finer grid)

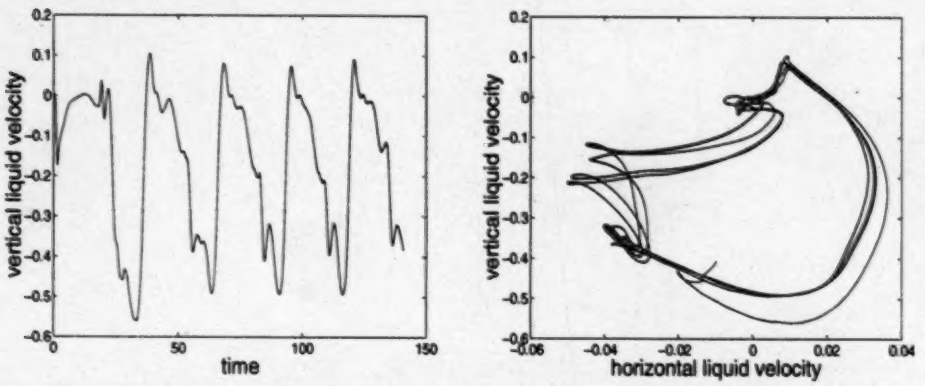

Figure 6.25: Time series of vertical liquid velocity to the left and the phase-portrait/trajectory of the two-dimensional liquid velocity to the right at point B (finer grid)

The simulations described above were conducted using an equal pressure model with the drag force used by Pan et al. (2000) [138], where the drag coefficient is characteristic for sufficiently contaminated systems. The expressions of the inter-phase terms are

$$\beta(\Phi, \mathbf{u}, \mathbf{v}) = \frac{3\Phi(1-\Phi)}{8R_b} C_D \rho_1 |\mathbf{v} - \mathbf{u}|$$

$$C_D = max\left\{ \frac{24}{Re_m}\left(1 + 0.15 {Re_m}^{0.687}\right), \frac{8}{3}\frac{Eo}{Eo+4} f \right\}$$

$$f = \left\{ \frac{1 + 17.67(1-\Phi)^{9/7}}{18.67(1-\Phi)^{3/2}} \right\}^2$$

$$Re_m = \frac{2R_{b1}|\mathbf{v}-\mathbf{u}|}{\mu_m}$$

$$\mu_m = \frac{\mu_1}{1-\Phi}$$

$$p_1 = p_2 = p$$

$$\xi(\Phi) = 0$$

$$M^i_{Gvm} = -M^i_{Lvm} = \Phi\rho_1\mu(\Phi)\left(\frac{D_{\mathbf{v}}\mathbf{v}}{Dt} - \frac{D_{\mathbf{u}}\mathbf{u}}{Dt}\right)$$

$$\mu(\Phi) = \frac{1}{2}(1-\Phi)(1+0.32\Phi)$$

$$\mu_d = 0$$

$$\mu_c(\Phi) = (1-\Phi)\mu_1(1+0.25\Phi)$$

If we alter the formula for the drag coefficient and instead, we use the classical formula specific for the homogeneous regime, $C_d = 24/Re$, the fluctuations of the vertical liquid velocity almost die out at the center of the column as it can be clearly seen from Figure 6.26. This illustrates how crucial the choice of the drag force is.

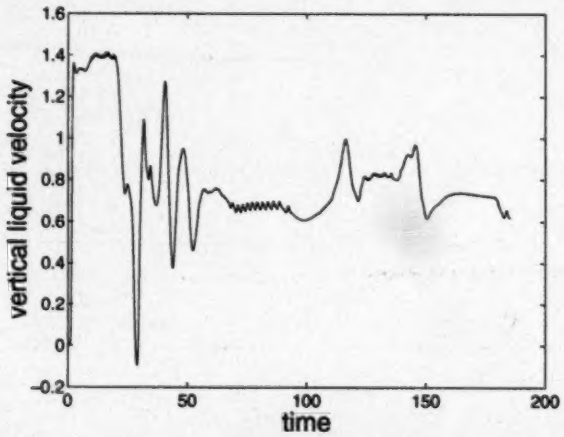

Figure 6.26: Time series of the vertical liquid velocity at point C (different drag).

We also implemented a two-pressure model where the difference between the two pressures was modelled according to the formula (3.42) given in chapter 3.

$$p_2 - p_1 = -c_p\ \rho_1\ (1-\Phi)|\mathbf{v}-\mathbf{u}|^2$$

$$c_p = 1/4$$

The vertical liquid profile in the reference point C is given in Figure 6.27 and the horizontal profile in point C is given in Figure 6.28.

The new model is able to capture more than one frequency of the signal, therefore it looks a bit more irregular than the one dimensional model (compare Figs. 6.27 with 6.24). The amplitude of the oscilations is within the same range as the experiments. The improvement of the two-pressure model it is clearly illustrated if we compare the frequencies of the experimental signal and of the predicted signal. Notice that a timeframe $T = 200s$ represents T (nondimensionlized)= 80. This can be seen if we analyze Figs. 6.27 and 6.23 for point C. We obtain almost the same period as the experimental value of 17 s. With the one pressure model the period was overestimated (it was twice as the experimental value) (Fig. 6.24 versus Fig. 6.23 - Part b). Therefore, the improvement brought by a two pressure model is considerable (compare Figs. 6.27 with 6.24). Close to the wall (see Fig. 6.29) the amplitude of the signal continues to be too small compared to the experimental values. We have to refine the grid to resolve the boundary layer close to the wall.

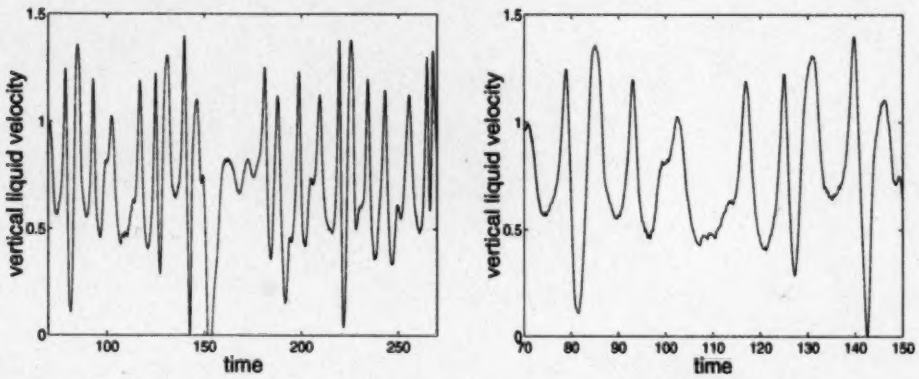

Figure 6.27: Time series of the vertical liquid velocity at point C (left: T=280) (right: T=80 Tdim=200s)

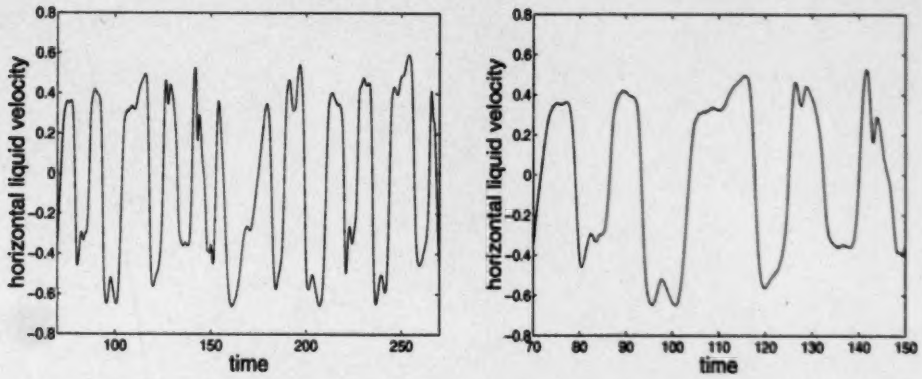

Figure 6.28: Time series of the horizontal liquid velocity at point C (left: T=280) (right: T=80 Tdim=200s)

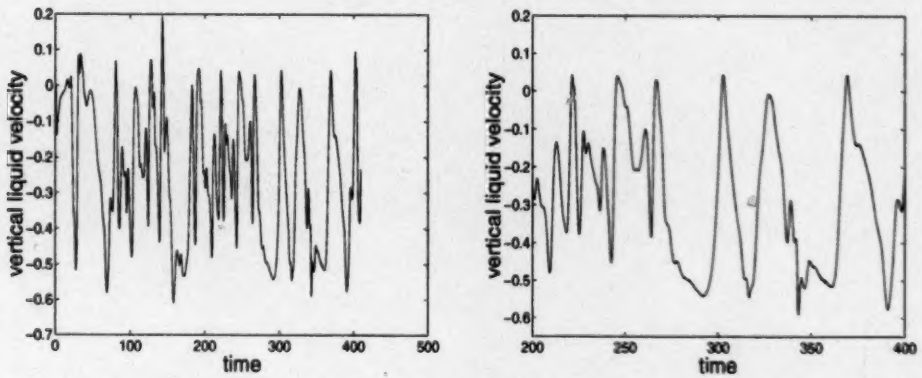

Figure 6.29: Time series of the vertical liquid velocity at point B (left: T=420) (right: T=200)

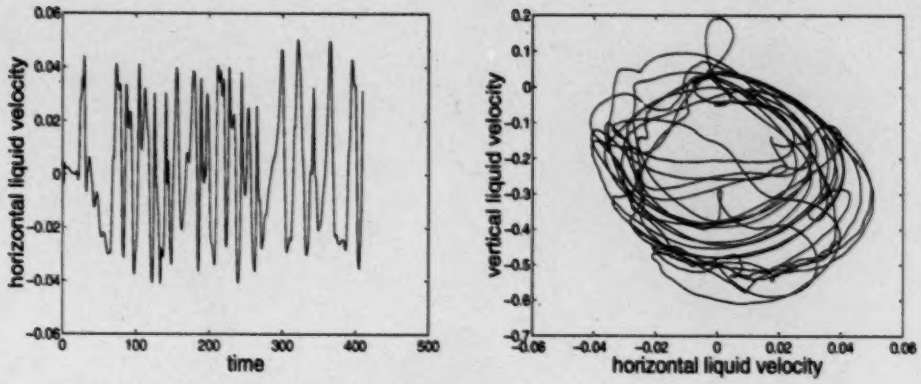

Figure 6.30: Time series of the horizontal liquid velocity at point B (left: T=420) and the phase-portrait/trajectory to the right

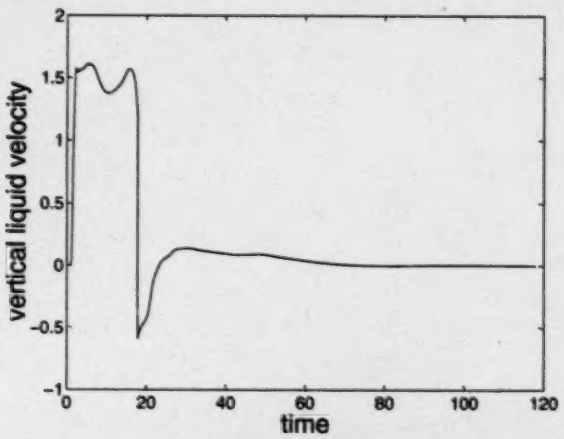

Figure 6.31: Time series of the vertical liquid velocity at point C .

We also tried the case of the two-pressure model taking also into account the bubble induced shear stress term given by the formula (3.43). This means that at the right hand side of the momonetum equation for the liquid phase we added the term

$$\nabla \cdot [(1-\Phi)\tau_L^T]$$

$$p_2 - p_1 = -c_p\ \rho_1\ (1-\Phi)|\mathbf{v}-\mathbf{u}|^2$$

$$\tau_L^T = -\Phi\rho_1 \left[\frac{3}{20}|\mathbf{v}-\mathbf{u}|^2 I + \frac{1}{20}(\mathbf{v}-\mathbf{u})\otimes(\mathbf{v}-\mathbf{u})\right]$$

The vertical liquid profile in the reference point C given in Figure 6.31 does not seem to catch the dynamical movement of the bubble plume.

Many other formulas and correlations can be tested. The conclusion is that our understanding regarding the appropriate closure terms for the coefficients is far from being elucidated and extensive numerical simulations are the only way to validate them. However, with the increasing computer power, this type of simulations will become possible.

The best fit with the experimental values considering both the frequency and the amplitude of the oscillation was obtained with the two-dimensional two-pressure model.

6.4 Three-dimensional simulations in a cylindrical bubble column

In the previous section we saw that, a flat, rectangular, almost two-dimensional bubble column, non-uniformally aerated, with a sparger located in the center axis can be used for the validation of dynamic flow models. This is because in 2D, the bubble plume behaves in a periodic, thus predictable way. The regular movement of the bubble swarm triggers a similar periodic behavior for the liquid phase. The liquid velocity time series in vertical and horizontal direction resemble the undamped harmonic oscillations. However, as very well illustrated in the paper by Becker et al. (1999) [15], the dynamic behavior in a cylindrical column is chaotic and not predictable. That is the reason for which most of the numerical simulations existent in the literature are done for the case of a flat rectangular column and not for the case of a cylindrical column. Becker et al. [15] actually calculated the Kolmogorov entropy through the software RRCHAOS and proved the chaotic character of the velocity time series. They showed that there is no low frequency that is characteristic for the whole column. They assume that the dynamic behavior is linked to the irregular radial movement of the bubble hose in the sparger zone.

However, Franz et al. [71] and Fisher et al. [70], both recognize experimentally the phenomenon of the bubble hose, defined as a zone of high bubble number density moving helically in a bubble column. Therefore, because of one more degree of freedom, the periodical movement of the bubble hose noticed in flat bubble columns is replaced by a helical movement in cylindrical bubble columns. As noticed by Fisher et al. [70], the height of the turns of the helix seems to be a function of the superficial gas velocity: the higher the gas velocity, the smaller the height of the turn. The helical rise of the bubbles triggers a helical liquid flow both upwards and downwards. The movement of the bubble hose also gives rise to eddies, small vortices that move along the streamlines. In the central part of the column, a region of homogeneous turbulence (swarm turbulence) exists. In this zone, bubble coalescence predominates.

Because of this, large bubbles will be formed in the central area that will rise with a different speed than the regular small bubbles. Our model does not handle this type of behaviour, since the bubble coalescence is not modelled in our equations. All the bubbles are assumed to be perfect spheres of constant radius. Despite all these clear drawbacks, we examined if at least at a qualitative level we can capture the helical motion of the bubbles. We would also like to see if once the superficial velocity is increased, the height of the turn gets smaller.

In all the simulations, we assumed the dimensions of the column to be fixed, namely $D = 20$ cm and $H = 40$ cm. Of course, the higher the column, the more spectacular the helical behavior would become, but that would increase the cost of the 3D computations. We just want to see if our homogeneous model can capture this helical regime, characteristic for the transition to turbulence.

We considered three different flow rates and two different radii for the aerated inlet areas. The first case corresponds to a flow rate of $\Phi_v = 1$ l/min, $r_s = 2$ cm yielding a volume fraction of $\Phi_0 = 6.63\%$. The second case corresponds to a flow rate of $\Phi_v = 2$ l/min, $r_s = 2$ cm yielding a volume fraction of $\Phi_0 = 13\%$. The third case corresponds to a flow rate of $\Phi_v = 4$ l/min, $r_s = 4$ cm yielding a volume fraction of $\Phi_0 = 3.3\%$.

Figures 6.32 and 6.33 show that for that set of parameters we are still in the homogeneous regime, therefore we have not yet reached the transition to turbulence regime.

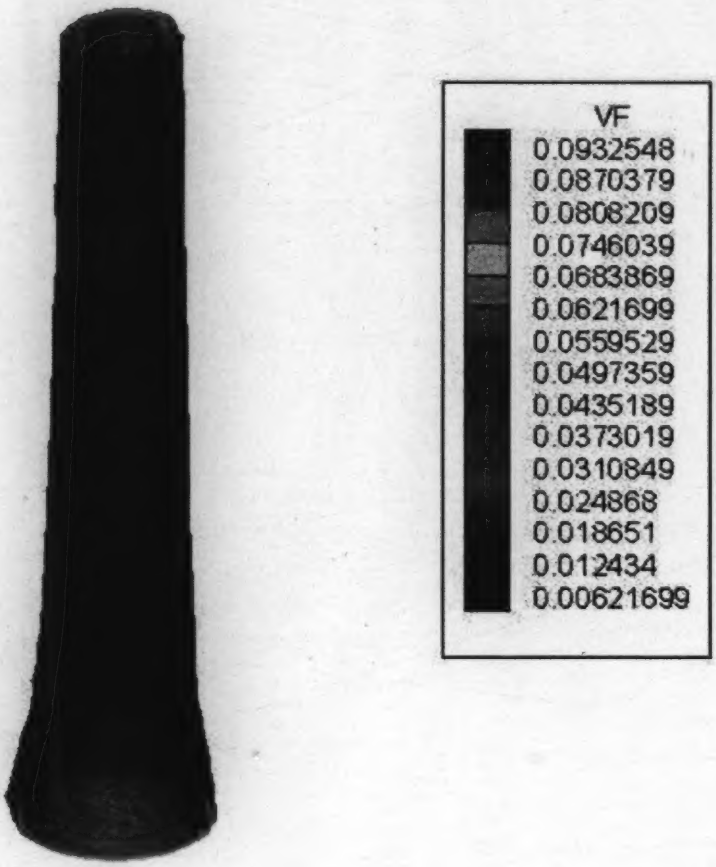

Figure 6.32: Snapshot of gas hold-up profile: $\Phi_v = 1$ l/min, $r_s = 2$ cm

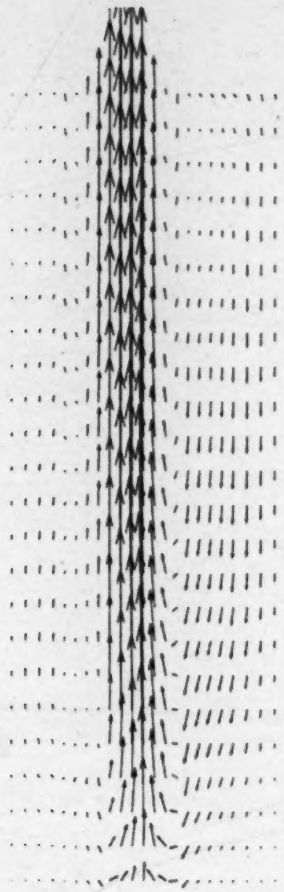

Figure 6.33: Liquid velocity field (x=D/2: vertical central plane cross-section): $\Phi_v = 1$ l/min, $r_s = 2$ cm

Figures 6.34 and 6.35 show that for the second set of parameters we are already in the spiral-flow regime. The helical movement of the bubble swarm is clearly pictured in these two pictures (the same picture - two different angles). They are snapshots taken after 43 s from the beginning of the simulations. The asymmetric behavior of the flow can be seen better in Figs. 6.36 and 6.37 which present the 2D slices of gas holdup distribution in two planes, perpendicular to each other, containing the central axis of the cylinder. The motion of the bubble plume induces a similar spiral-type of motion of the liquid phase. It also creates small

eddies that go with the flow. Both phenomena can be seen in Figs. 6.38 - 6.41.

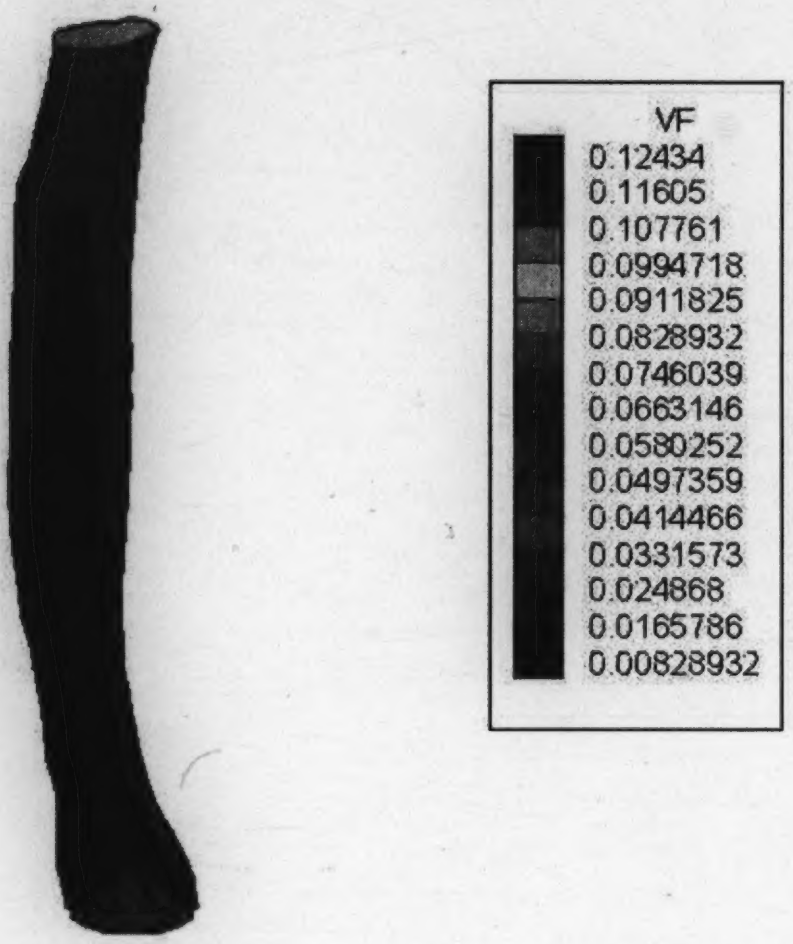

Figure 6.34: Snapshot of gas hold-up profile: $\Phi_v = 2$ l/min, $r_s = 2$ cm

Figure 6.35: Snapshot of gas hold-up profile (different angle): $\Phi_v = 2$ l/min, $r_s = 2$ cm

Figure 6.36: Snapshot of gas hold-up profile (slice x = D/2): $\Phi_v = 2$ l/min, $r_s = 2$ cm

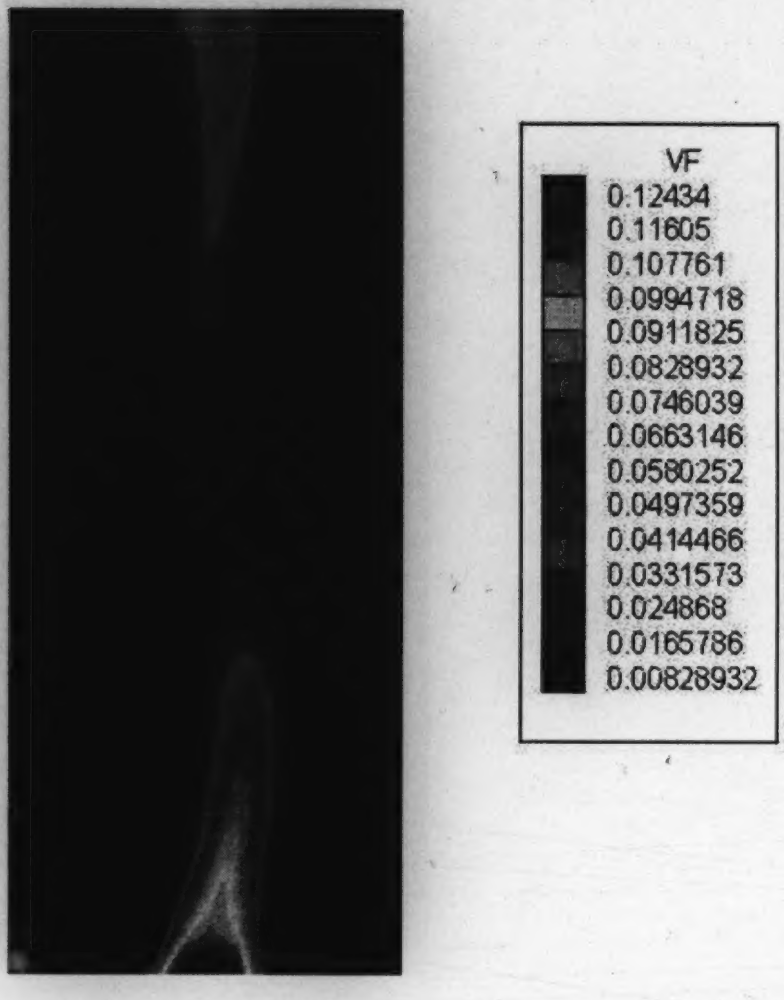

Figure 6.37: Snapshot of gas hold-up profile (slice y = D/2): $\Phi_v = 2$ l/min, $r_s = 2$ cm

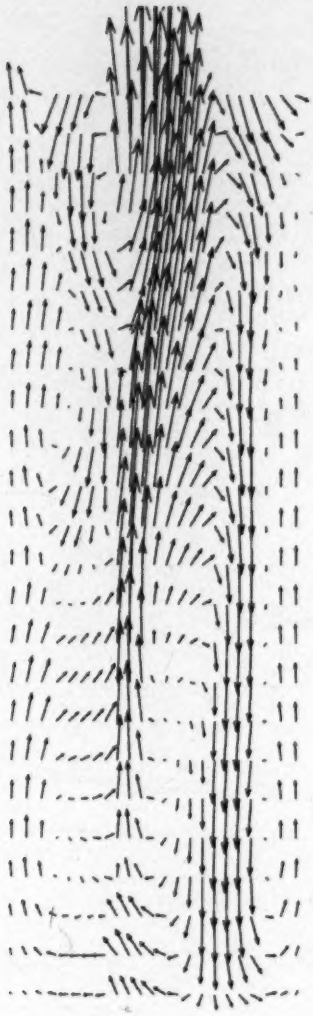

Figure 6.38: Liquid velocity field (x=D/2: vertical central plane cross-section): $\Phi_v = 2$ l/min, $r_s = 2$ cm

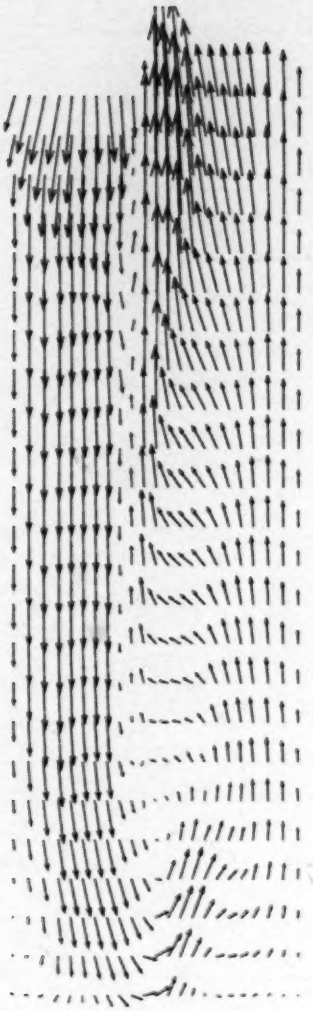

Figure 6.39: Liquid velocity field (y=D/2: vertical central plane cross-section): $\Phi_v = 2$ l/min, $r_s = 2$ cm

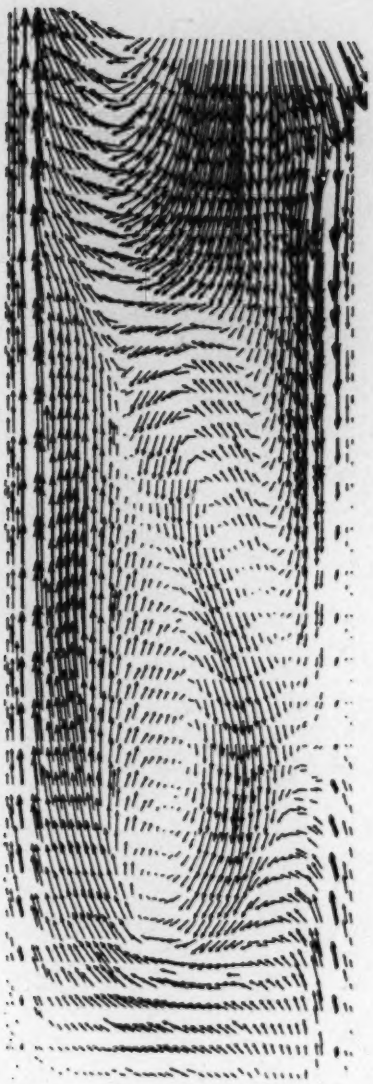

Figure 6.40: Liquid velocity field (XZ plane: y=0.25) $\Phi_v = 2$ l/min, $r_s = 2$ cm

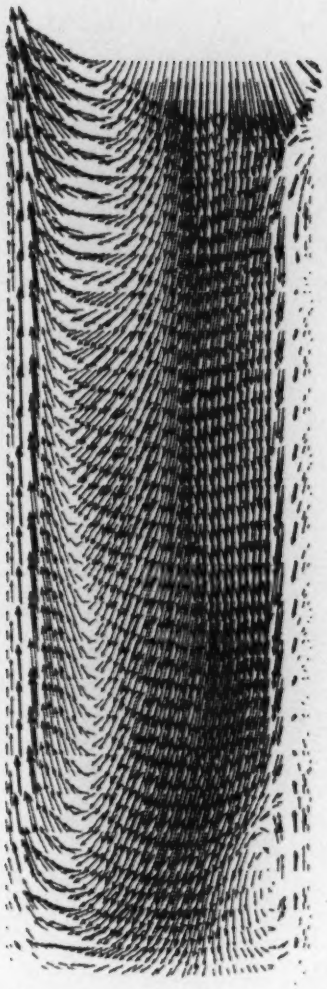

Figure 6.41: Liquid velocity field (XZ plane: y=0.75) $\Phi_v = 2$ l/min, $r_s = 2$ cm

Figures 6.42 - 6.45 show that by increasing the flow rate, the height of the turn got smaller yielding a more pronounced helical shape. The similar spiral-type of motion of the liquid phase and the small eddies that go with the flow can be seen in Figs. 6.46 - 6.50.

Figure 6.42: Snapshot of gas hold-up profile: $\Phi_v = 4$ l/min, $r_s = 4$ cm

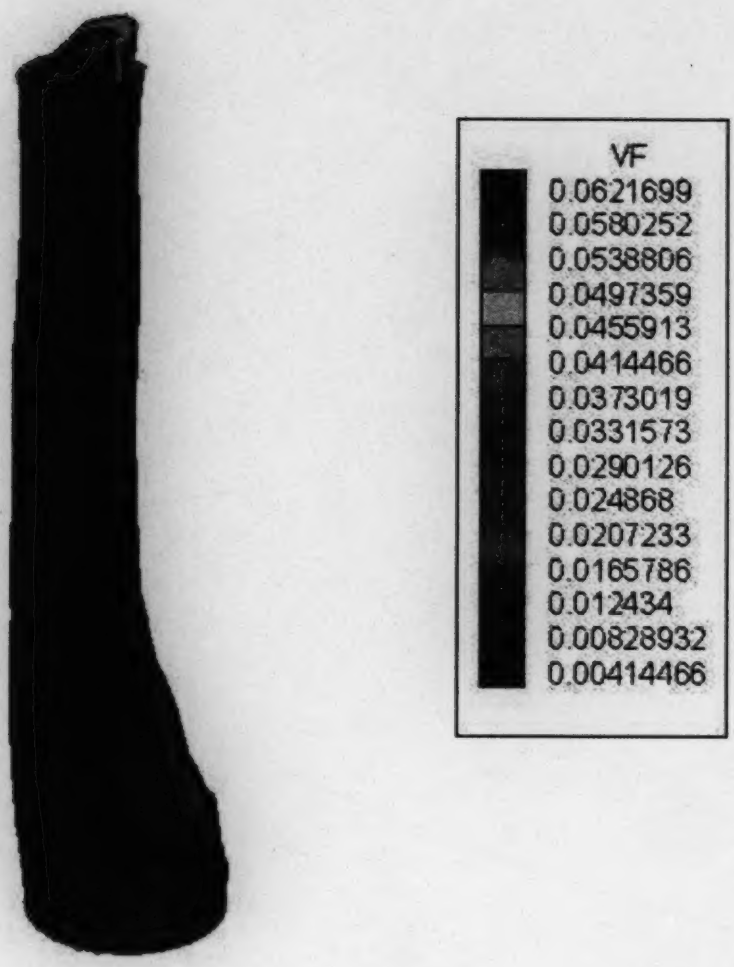

Figure 6.43: Snapshot of gas hold-up profile (different angle): $\Phi_v = 4$ l/min, $r_s = 4$ cm

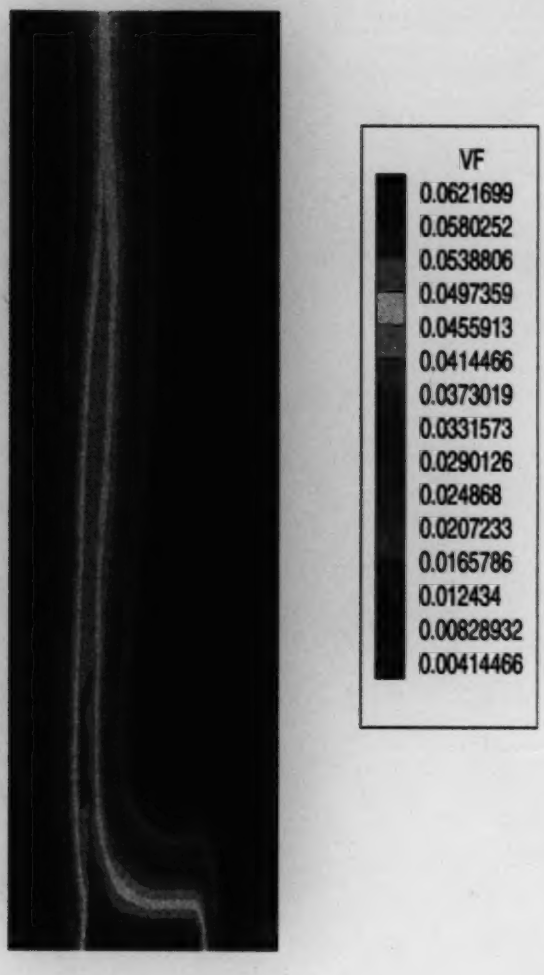

Figure 6.44: Snapshot of gas hold-up profile (slice x = D/2): $\Phi_v = 4$ l/min, $r_s = 4$ cm

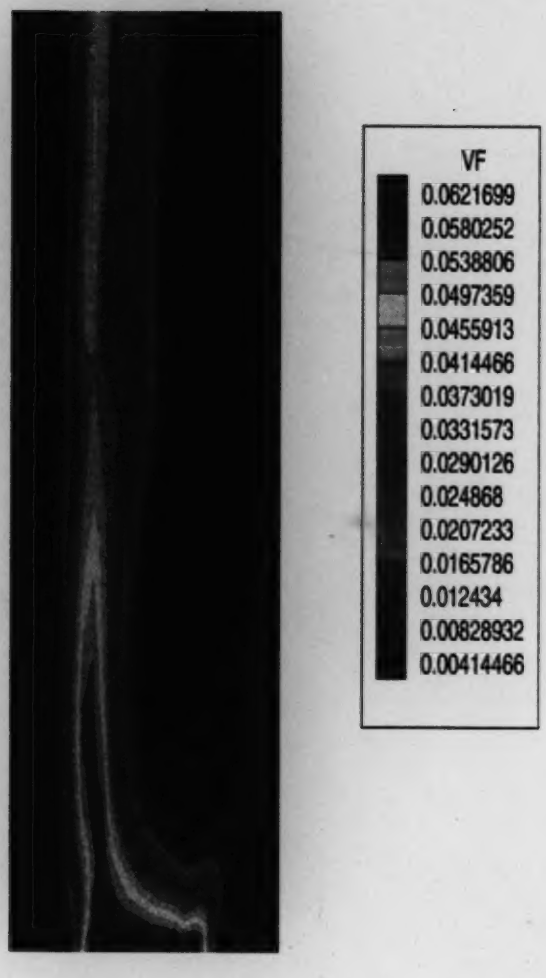

Figure 6.45: Snapshot of gas hold-up profile (slice y = D/2): $\Phi_v = 4$ l/min, $r_s = 4$ cm

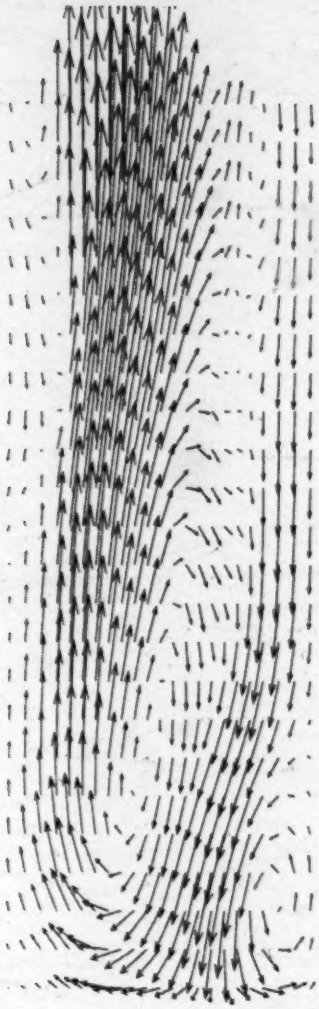

Figure 6.46: Liquid velocity field (x=D/2: vertical central plane cross-section): $\Phi_v = 4$ l/min, $r_s = 4$ cm

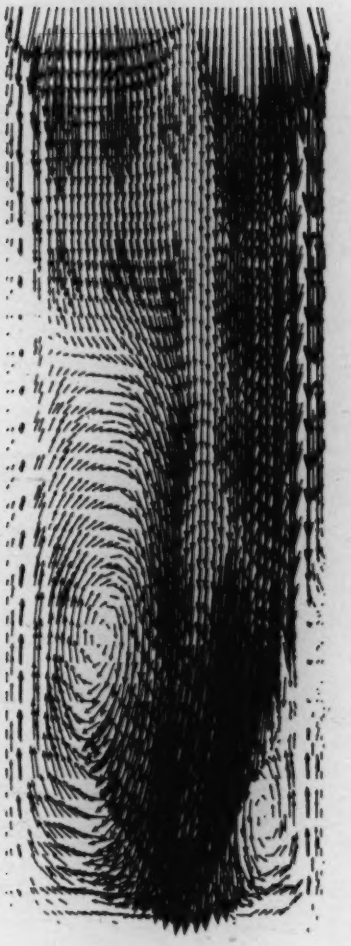

Figure 6.47: Liquid velocity field (YZ plane: x=0.75) $\Phi_v = 4$ l/min, $r_s = 4$ cm

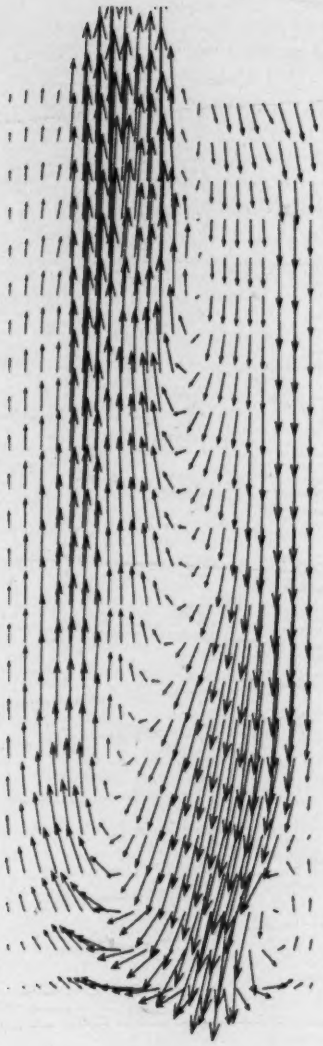

Figure 6.48: Liquid velocity field (y=D/2: vertical central plane cross-section): $\Phi_v = 4$ l/min, $r_s = 4$ cm

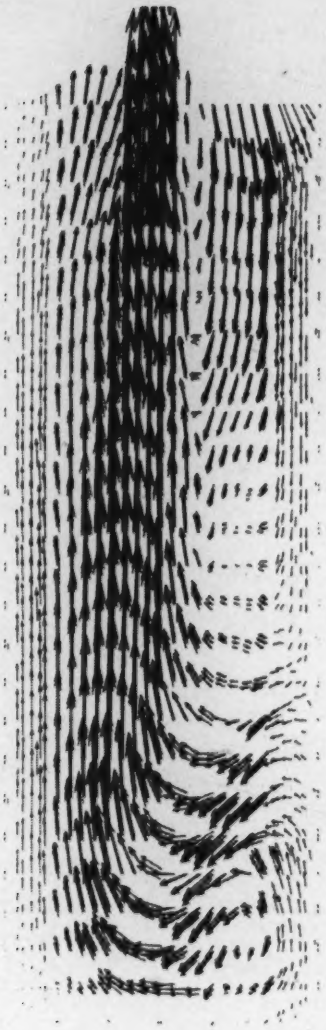

Figure 6.49: Liquid velocity field (XZ plane: y=0.35) $\Phi_v = 4$ l/min, $r_s = 4$ cm

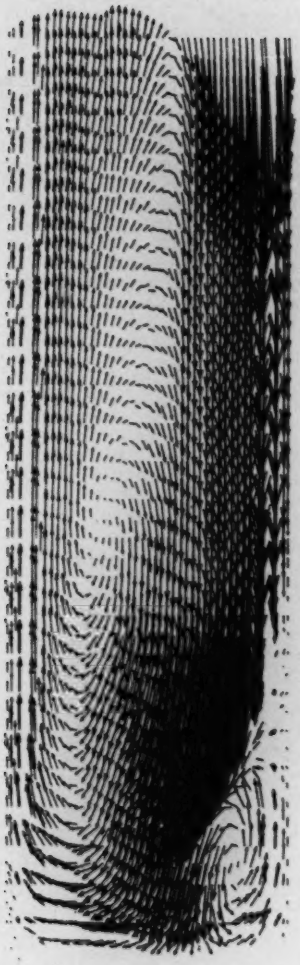

Figure 6.50: Liquid velocity field (XZ plane: y=0.75) $\Phi_v = 4$ l/min, $r_s = 4$ cm

The present technique is clearly capable of resolving a transitional flow in a cylindrical column, but a further quantitative comparison with experimental data is needed for a complete validation.

Chapter 7

Conclusions and Future Directions

In this thesis, a new numerical scheme was developed for solving a set of non-linear partial differential equations that are used to describe two-phase flow models. The numerical scheme is robust and can be applied for solving a very diverse set of problems. We tested our numerical scheme on a sedimentation problem and showed the effectivness of the shock-capturing term. We also simulated the cases of a wave propagation phenomena in a cylindrical bubble column and the circulation flow in a viscous fluid, solving in this way both a convection-diffusion system of equations and a problem where the elliptic operator is dominant. In chapter 6 we showed that our numerical scheme performs well even when dealing with advection-dominated flows. We were able to obtain the same number of vortical structures as in the experiments.

Another challenge we faced was the choice of appropriate correlations for the inter-phase terms. When dealing with a unidirectional flow, as in the case of wave propagation, we were able to perform a rigorous mathematical non-linear analysis and derive a correlation for the bulk modulus of elasticity such that our numerical simulation to be as close as possible with the experiments. However, this approach can only work when the flow is one-dimensional or unidirectional, therefore when dealing with two- or three-dimensional flows this correlation does not hold since all three components of the velocities are of the same order of magnitude.

We also addressed the issue of predicting the transition to turbulence, which is characterized by a highly vortical, quasi-periodic flow in 2D and a spiral-vortical flow (helical shape) in 3D using a laminar model. Our agreement with the experiments in 2D was reasonable. We also tried different forms for the interaction terms between the two phases. In agreement with our expectations, a two-pressure model performed better than a one pressure model. The one pressure model was not able to capture the frequency of the oscillations properly. Also, the introduction of a bubble-induced turbulence term did not have a positive effect. The

most important inter-phase term proved to be the drag force. The appropriate choice of the coefficients is still not a topic that is completely understood. Other terms like the lift force, the wall force and many other terms can be incorporated in the model and they may have a positive impact.

With the continuous increase in computer power, more advanced direct simulations will soon be performed. By averaging those results, new formulas for the inter-phase terms may become available. Further research is required to find satisfactory formulae for the inter-phase terms.

Bibliography

[1] Y. Achdou and J.-L. Guermond. Convergence analysis of a finite element projection/lagrange-galerkin method for the incompressible navier-stokes equations. *SIAM J.Numer. Anal.*, 37:799–826, 2000.

[2] T.B. Anderson and R. Jackson. Fluid mechanical description of fluidized beds. equations of motion. *Indust. Engng. Chem. Fundam.*, 6:527–539, 1967.

[3] S.P. Antal, R.T. Lahey Jr., and J.E. Flaherty. Analysis of phase distribution in fully developed laminar bubbly two-phase flow. *Int. J. of Multiphase Flow*, 17(5):635–652, 1991.

[4] S.V. Apte, K. Mahesh, and T. Lundgren. A eulerian-lagrangian model to simulate two-phase/particulate flows. *Center for Turbulence Research*, Annual Research Briefs 2003:161–171, 2003.

[5] G.S. Arnold. *Entropy and objectivity as constraints upon constitutive equations for two-fluid modeling of multiphase flow.* Phd thesis, Reensselaer Polytechnique Institute, Troy, New York, 1988.

[6] N. Ashgriz and J.Y. Poo. Flair-flux line-segment model for advection and interphase reconstruction. *J. Comput. Physics*, 93:449, 1991.

[7] A.K. Ask, H.K. Dahle, K.H. Karlsen, and H.F. Nordhaug. A local streamline eulerian-lagrangian method for two-phase flow. In *Proceedings of the XIII international conference on computational methods in water resources*, pages 645–650, 2000.

[8] P. Bach and J. Villadsen. Simulation of the vertical flow of a thin, wavy film using a finite-element method. *Int. J. Heat Mass Transfer*, 37:815–827, 1984.

[9] P.K. Barr and W.T. Ashurst. *An interphase scheme for turbulent flame propagation.* Sandia National Laboratories, 1984. Technical Report SAND82-8773.

[10] J W. Barrett and K.W. Morton. Approximate symmetrization and petrov-galerkin methods for diffusion-convection problems. *Comp. Meth. Appl. Mech. Eng.*, 45:97–122, 1979.

[11] G.K. Batchelor. Statistical hydrodynamics of dispersed systems. *J. Fluid Mech.*, 49:489–507, 1970.

[12] G.K. Batchelor. Sedimentation in a dilute dispersion spheres. *J. Fluid Mech.*, 52:245–268, 1972.

[13] G.K. Batchelor. Void fraction disturbunces in a uniform bubbly fluid. *Ann. Rev. Fluid Mech.*, 16:211–231, 1974.

[14] G.K. Batchelor. A new theory of instability of a uniform fluidized bed. *J. Fluid Mech.*, 193:75–110, 1988.

[15] S. Becker, H. De Bie, and J. Sweeney. Dynamic flow behaviour in bubble columns. *Chemical Engineering Science*, 54:4929–4935, 1999.

[16] S. Becker, A. Sokolichin, and G. Eigenberger. Gas-liquid flow in bubble columns and loop reactors: Part ii. comparison of detailed experiments and flow simulations. *Chemical Engineering Science*, 49:5747–5762, 1994.

[17] D. Bestion and F. Barre. Status of thermal-hydraulic modelling and assessment: open issues. In *OECD/CSNI Workshop on Transient Thermal-Hydraulic and Neutronic Codes Requirements*, Annapolis, Md, USA, 5-8 November 1996.

[18] A. Biesheuvel and W.C.M. Gorissen. Void fraction disturbances in a uniform bubbly fluid. *Intl J.Muliphase Flow*, 16:211–231, 1990.

[19] A. Biesheuvel and L.Van Wijngaarden. Two-phase flow equations for a dilute dispersion of gas bubbles in liquid. *J. Fluid Mech.*, 148:301–318, 1984.

[20] S. Biesheuvel, A.and Spoelstra. The added mass coefficient of a dispersion of spherical gas bubbles in liquid. *Intl J.Muliphase Flow*, 15:911–924, 1989.

[21] O. Borchers, C. Busch, A. Sokolichin, and G. Eigenberger. Applicability of the standard $k-\epsilon$ turbulence model to the dynamic simulation of bubble columns. part ii: Comparison of detailed experiments and flow simulation. *Chemical Engineering Science*, 54:5927–5935, 1999.

[22] E.T. Bouloutas and M.A. Celia. An improved cubic petrov-galerkin method for simulation of transient advection-diffusion processes in rectangularly decomposable domains. *Comp. Meth. Appl. Mech. Eng.*, 91:289–308, 1991.

[23] J.A. Bouré. Two-phase flow models: the closure issue. In G.F. Hewitt, J.M. Delhaye, and N. Zuber, editors, *Multiphase Science and Technology*, 3. Hemisphere Publishing Corporation, 1987.

[24] F. Brezzi, T.J.R. Hughes, L.D. Marini, A. Russo, and E. Süli. A priori analysis of residual-free bubbles for advection-diffusion problems. *SIAM J.Numer. Anal.*, 36:1933–1948, 1999.

[25] A.N. Brooks and T.J.R. Hughes. Streamline upwind/petrov-galerkin formulations for convection dominated flows with special emphasis on the incompressible navier-stokes equations. *Comput. Meth. Appl. Mech. Eng.*, 32:199–259, 1982.

[26] B. Bunner and G. Tryggvason. Direct numerical simulations of three-dimensional bubbly flows. *Physics of Fluids*, 11:1967–1969, 1999.

[27] L.F. Burns. *The effect of lower surface tension on fluid dynamics and mass transfer in bubble column reactors.* Ms thesis, Louisiana State University, Baton Rouge, 1995.

[28] L.F. Burns and R.G. Rice. Circulation in bubble columns. *AIChE Journal*, 43(6):1390–1402, 1997.

[29] C. Caia and P. Minev. Validation of an eulerian model for bubbly flows and three-dimensional numerical simulations. In *Minisymposium on Computational Dynamics of Complex Fluids: Polymers, Glasses,Suspensions and Emulsions, for the Seventh U.S. National Congress on Computational Mechanics*, Albuqerque, New Mexico, 28-30 July 2003.

[30] C. Caia and P. Minev. A finite element method for an averaged multiphase flow model. *Int. J. of Computational Fluid Dynamics*, 18(2):111–123, 2004.

[31] M.A. Celia, T.F. Russell, I. Herrera, and R.E. Ewing. An Eularian-Lagrangian localized adjoint method for the advection-diffusion equation. *Adv. Water Resources*, 13:187–206, 1990.

[32] I. Celik and Y.Z. Wang. Numerical simulation of circulation in gas-liquid column reactors: Isothermal, bubbly, laminar flow. *International Journal of Multiphase Flow*, 20(6):1053–1070, 1994.

[33] J. Chen, A. Kemoun, M.H. Al-Dahhan, M.P. Dudukovic, D.J. Lee, and L.-S. Fan. Comparative hydrodynamics study in a bubble column using computer-automated radioactive particle tracking (carpt)/computed tomography (ct) and particle image velocimetry (piv). *Chemical Engineering Science*, 54:2199–2207, 1999.

[34] J.J.J. Chen, M. Jamialahmadi, and S.M. Li. Effect of liquid depth on circulation in bubble columns. *Chemical Engineering Research and Design*, 67:203–207, 1989.

[35] R.C. Chen and L.-S. Fan. Particle image velocimetry for characterizing the flow structure in three-dimensinal gas-liquid-solid fluidized beds. *Chemical Engineering Science*, 47:3615, 1992.

[36] R.C. Chen, J. Reese, and L.-S. Fan. Flow structure in a three-dimensional bubble column and three-phase fluidized bed. *AIChE Journal*, 40(7):1093–1104, 1994.

[37] X.-Q. Chen. Efficient particle tracking algorithm for two-phase flows in geometries using curvilinear coordinates. *Numerical Heat Transfer*, 32A(4):387–405, 1997.

[38] A.J. Chorin. Flame advection and propagation algoritms. *J. Comput. Physics*, 35:1–11, 1980.

[39] I. Christie, D.F. Griffiths, A.R. Mitchell, and O.C. Zienkiewicz. Finite element methods for second order differential equations with significant first derivatives. *Int. J. Num. Eng.*, 10:1389–1396, 1976.

[40] R. Clift, J.R. Grace, and M.E. Weber. *Bubbles, drops, and particles.* New York:Academic Press, 1978.

[41] J.P. Cocchi and R. Saurel. A riemann problem based method for compressible multifluid flows. *J. Comput. Phys.*, 137:265–298, 1997.

[42] P. Colella. A direct eulerian muscl scheme for gas dynamics. *SIAM J. Sci. Stat. Comp.*, 6:104–117, 1985.

[43] J.J. Connor and C.A. Brebbia. *Finite element techniques for fluid flow.* New York:Newness-Butterworths, 1977.

[44] F. Coquel, K.El. Amine, E. Godlewski, B. Perthame, and P. Rascle. A numerical method using upwind schemes for the resolution of two-phase flows. *Journal of Computational Physics*, 136:272–288, 1997.

[45] V. Daru and C. Tenaud. Evaluation of tvd high resolution schemes for unsteady viscous shocked flows. *Computers Fluids*, 30:89–113, 2001.

[46] C.N. Dawson. Godunov-mixed methods for advection-diffusion equations in multidimensions. *SIAM J. Num. Anal.*, 30:1315–1332, 1993.

[47] R. DeBar. *Fundamentals of the KRAFEN code.* LLNL, 1974. Technical Report UCIR-760.

[48] J.M. Delhaye. Instantaneous space-averaged equations. *Two-phase flows and heat transfer*, 1:81–90, 1976.

[49] E. Delnoij, J.A.M. Kuipers, and W.P.M. van Swaaij. Computational fluid dynamics applied to gas-liquid contactors. *Chemical Engineering Science*, 52:3623, 1997b.

[50] E. Delnoij, F.A. Lammers, J.A.M. Kuipers, and W.P.M. van Swaaij. Dynamic simulation of dispersed gas-liquid two-phase flows using a discrete bubble model. *Chemical Engineering Science*, 52:1429, 1997a.

[51] N.S. Deshpande and J.B. Joshi. Simultaneous measurements of gas and liquid phase velocities and gas hold-up using laser doppler velocimeter. *Chemical Engineering Communications*, 162:151–168, 1997.

[52] N. Devanathan, M.P. Dudukovic, A. Lapin, and A. Lübbert. Chaotic flow in bubble column reactors. *Chemical Engineering Science*, 50:2661, 1995.

[53] N. Devanathan, D. Moslemian, and M.P. Dudukovic. Flow mapping in bubble columns using carpt. *Chemical Engineering Science*, 45(8):2285–2291, 1990.

[54] J. Douglas Jr., F. Pereira, and L.-M. Yeh. A locally conservative eulerianlagrangian numerical method and its application to nonlinear transport in porous media. *Computational Geosciences*, 4:1–40, 2000.

[55] J. Douglas Jr. and T.F. Russell. Numerical methods for convection-dominated diffusion problems based on combining the method of characteristics with finite element or finite difference procedures. *SIAM J. Num. Anal.*, 19:871–885, 1982.

[56] D.A. Drew. Mathematical modeling of two-phase flow. *Annual Review of Fluid Mechanics*, 15:261–291, 1983.

[57] D.A. Drew, L.A. Cheng, and R.T. Lahey. The analysis of virtual mass effects in two-phase flow. *Intl. J. of Multiphase Flow*, 5:233–242, 1979.

[58] D.A. Drew and R.T. Lahey. The virtual mass and lift force on a sphere in rotating and straining inviscid flow. *Intl. J. of Multiphase Flow*, 13:113–121, 1987.

[59] D.A. Drew and R.T. Lahey. Application of general constitutive principles to the derivation of multidimensional two-phase flow equations. *Intl. J. of Multiphase Flow*, 5:243–263, 1989.

[60] D.A. Drew and L.A. Segel. Averaged equations for two-phase flows. *Stud. Appl. Maths*, 50:205–231, 1971.

[61] F. Durst, A.M.K.P. Taylor, and J.H. Whitelaw. Experimental and numerical investigation of bubble driven laminar flow in an axi-symmetric vessel. *International Journal of Multiphase Flow*, 10:557–569, 1984.

[62] T. Dyakovski, R.B. Edwards, C.G. Xie, and R.A. Williams. Application of capacitance tomography to gas-solid flows. *Chemical Engineering Science*, 52:2099–2110, 1997.

[63] B. Einfeldt. On godunov-type methods for gas dynamics. *SIAM J. Num. Anal.*, 25:294–318, 1988.

[64] A. Esmaeeli, E. Ervin, and G. Tryggvason. Numerical simulations of rising bubbles. In J.R. Blake, J.M. Boulton-Stone, and N.H. Thomas, editors, *Bubble Dynamics and Interphase Phenomena. Proc. IUTAM Symp.*, pages 247–255, Birmingham,U.K., 6-9 September 1993. Kluwer Academic: Dordrecht.

[65] A. Esmaeeli and G. Tryggvason. An inverse energy cascade in two-dimensional, low reynolds number bubbly flows. *J. Fluid Mech.*, 314:315–330, 1996.

[66] A. Esmaeeli and G. Tryggvason. Direct numerical simulations of bubbly flows. part1.low reynolds number arrays. *J. Fluid Mech.*, 377:313–345, 1998.

[67] A. Esmaeeli and G. Tryggvason. Direct numerical simulations of bubbly flows. partii. moderate reynolds number arrays. *J. Fluid Mech.*, 377:325–358, 1999.

[68] I. Faille and E. Heintzé. A rough finite volume scheme for modeling two-phase flow in a pipeline. *Computers Fluids*, 28(2):213–241, 1999.

[69] R.L. Ferch. Method of characteristics solutions for non-equilibrium transient flow boiling. *Int. J. Multiphase Flow*, 5:265–279, 1979.

[70] J. Fischer, H. Kumazawa, and E. Sada. On the local gas holdup and flow pattern in standard-type bubble columns. *Chemical Engineering and Processing*, 33:7–21, 1994.

[71] K. Franz, T. Börner, H.J. Kantorek, and R. Buchholz. Flow sructures in bubble columns. *Ger. Chem. Eng.*, 7:365–374, 1984.

[72] O.S. Galaktionov, P.D. Anderson, G.W.M. Peters, and F.N. van de Vosse. An adaptive front tracking technique for three-dimensional transient flows. *Int. J. Num. Meth. Fluids*, 32:201–218, 2000.

[73] N.W. Geary and R.G. Rice. Circulation and scale-up in bubble columns. *AIChE Journal*, 38(1):76–82, 1992.

[74] Ginzburg and Wittum. Two-phase flows on interface refined grids modeled with vof, staggered finite volumes, and spline interpolants. *Journal of Computational Physics*, 166(2):302 – 335, 2001.

[75] M.F. Göz and C.-D. Munz. Approximate riemann solvers for fluid flow with material interfaces. In E.F. Toro and J.F. Clarke, editors, *Numerical methods for wave propagation*, pages 211–235. Kluwer Academic Publishers, 1998.

[76] S. Grevskott, B.H. Sannaes, M.P. Duduukovic, K.W. Hjarbo, and H.F. Svendsen. Liquid circulation, bubble size distributions, and solids movement in two- and three-phase bubble column. *Chemical Engineering Science*, 51:1703–1713, 1996.

[77] J. Grienberger and H. Hofmann. Investigations and modelling of the bubble columns. *Chemical Engineering Science*, 47:2215–2220, 1992.

[78] J.S. Groen, R.G.C. Oldeman, R.F. Mudde, and H.E.A. Van Den Akker. Coherent structures and axial dispersion in bubble column reactors. *Chemical Engineering Science*, 51(10):2511–2520, 1996.

[79] J.-L. Guermond. Stabilization of Galerkin approximations of transport equations by subgrid modeling. *Modél. Math. Anal. Numér.*, 33:1293–1316, 1999.

[80] J.-L. Guermond. A subgrid viscosity method for solving non-coercive pde's in environmental science. In *ISFMA Symposium on Environmental Science and Engineering with Related Mathematical Problems*, Hangzhou, China, August 19-26 2000.

[81] T.Z. Harmathy. Velocity of large drops and bubbles in media of infinite or restricted extent. *AIChE Journal*, 6(2), 1961.

[82] B. Harton, A. Engquist, , S. Osher, and S. Chakravarthy. Uniformly high order accurate essentially non-oscillatory schemes iii. *Journal of Computational Physics*, 71(2):213–303, 1987.

[83] G. Hauke. Simple stabilizing matrices for the computation of compressible flows in primitive variables. *Comput. Methods Appl. Mech. Engrg*, 190:6881–6893, 2001.

[84] I. Herrera, R.E. Ewing, M.A. Celia, and T.F. Russell. Eulerian-lagrangian localized adjoint methods: the theoretical framework. *Num. Methods for PDEs*, 9:431–458, 1993.

[85] G.F. Hewitt, J.M. Delhay, and N. Zuber, editors. *Muliphase science and technology*. Washington, D.C.:Hemisphere, 1982.

[86] J.H. Hills. Radial non-uniformity of velocity and voidage in a bubble column. *Transactions of Institution of Chemical Engineers*, 52:1–9, 1974.

[87] C.W. Hirt and B.D. Nichols. Volume of fluid (vof) methods for the dynamics of free boundaries. *J. Comput. Physics*, 39:201–225, 1981.

[88] G.M. Homsy, M.M. El-Kaissy, and A. Didwania. Instability waves and the origin of bubbles in fluidized beds. Part ii. Comparison with theory. *Intl J.Muliphase Flow*, 6:305–318, 1980.

[89] B.P.B. Hoomans, J.A.M. Kuipers, W.J. Briels, and W.P.M. van Swaaij. Disrete particle simulation of bubble and slug formation in a two-dimensional gas-fluidised bed: a hard-sphere approach. *Chemical Engineering Science*, 51(1):99–118, 1996.

[90] S.M. Huang, A. Plaskovski, C.G. Xie, and M.S. Beck. Tomographic imaging of two-component flow using capacitance sensors. *Journal of Physica E*, 22:173–177, 1989.

[91] T.J.R. Hughes and A.N. Brooks. A multidimensional upwinding scheme with no cross-wind diffusion. In Hughes, editor, *Finite element methods for convection dominated flows*, volume 34. ASME: New York, 1979.

[92] T.J.R. Hughes, J.P. Franca, and G. Hulbert. A new finite element formulation for computational fluid dynamics: Viii. the galerkin/least-squares method for advective-diffusive equations. *Comput. Methods Appl. Mech. Engrg.*, 73:173–189, 1989.

[93] S.R. Idelsohn, M.A. Stori, and E. Onate. Lagrangian formulations to solve free surface incompressible inviscid fluid flows. *Computer Methods in Applied Mechanics and Engineering*, 191:583–593, 2001.

[94] M. Iguchi, T. Kondoh, Z.I. Morita, K. Nakajima, K. Hanazaki, T. Uemura, and F. Yamamoto. Velocity and turbulence measurements in a cylindrical bath subject to centric bottom gas injection. *Mettalurgical Transactions B*, 26 B(2):241–247, 1995.

[95] M. Ishii. *Thermo-fluid dynamics theory of two-phase flow.* Paris: Eyrolles, 1975.

[96] M. Ishii and N. Zuber. Drag coefficient and relative velocity in bubbly, droplet and particulate flows. *AIChE Journal*, 25:843–855, 1979.

[97] R. Jackson. Fluid mechanical theory. In J.F. Davidson and D. Harrison, editors, *Fluidization.* Academic, 1971.

[98] H.A. Jakobsen. Phase distribution phenomena in two-phase bubble column reactors. *Chemical Engineering Science*, 56:1049–1056, 2001.

[99] H.A. Jakobsen, B.H. Sannaes, S. Grevskott, and H.F. Svendsen. Modeling of vertical bubble-driven flows. *Ind. Eng. Chem. Res.*, 36:4052–4074, 1997.

[100] D.J. Jeffrey. Conduction through a random suspension of spheres. *Proc. R. Soc. Lond.*, A335:355–367, 1973.

[101] C. Johnson. *Numerical solutions of partial differential equations by the finite element method.* Cambridge University Press, 1987.

[102] C. Johnson and J. Pitkäranta. An analysis of discontinuous galerkin methods for a scalar hyperbolic equation. *J. Math. Comp.*, 46:1–26, 1986.

[103] C. Johnson, A. Szepessy, and P. Hansbo. On the convergence of shock-capturing streamline diffusion finite element methods for hyperbolic conservation laws. *J. Math. Comp.*, 54:107–129, 1990.

[104] A.V. Jones and A. Prosperetti. On the suitability of first-order differential models for two-phase flow prediction. *Intl J.Muliphase Flow*, 11:133–148, 1985.

[105] J.B. Joshi. Computational flow modelling and design of bubble column reactors. *Chemical Engineering Science*, 56:5893–5933, 2001.

[106] J.B. Joshi and M.M. Sharma. A circulation cell model for bubble columns. *Transactions of Institution of Chemical Engineers*, 57:244–251, 1979.

[107] B.A. Kashiwa and R.M. Rauenzahn. *A multimaterial formalism.* New York: ASME, 1994.

[108] P. Keast. Moderate-degree tethahedral quadrature formulas. *Computer Methods in Apllied Mechanics and Engineering*, 55:339–348, 1986.

[109] E. Kojima, H. Unno, Y. Sato, T. Chida, H. Imai, K. Endo, I. Inoue, J. Kobayashi, H. Kaji, H. Nakanishi, and K. Yamamoto. Liquid phase velocity in a 5.5 m diameter bubble column. *Journal of Chemical Engineering of Japan*, 13(1):16–21, 1980.

[110] J.B.W Kok. *Dynamics of gas bubbles moving through liquid.* Phd thesis, University of Twente, Enschede, Netherlands, 1989.

[111] D.B. Kothe et al. Computer simulations of metal casting processes: A new approach. Technical report LALP-95-197, Los Alamos National Laboratories, 1995.

[112] S. Kumar, N. Devanathan, D. Moslemian, and M.P. Dudukovic. Effect of scale on liquid circulation in bubble columns. *Chemical Engineering Science*, 49:5637–5652, 1994.

[113] S. Kumar, B. Vanderheyden, W, N. Devanathan, and N.T. Padial. Numerical simulation and experimental verification of the gas-liquid flow in bubble columns. *AIChE Symposium Series*, 305:11–19, 1995.

[114] S.B. Kumar, D. Mosleman, and M.P. Dudukovic. Gas-holdup measurements in bubble columns using computer tomography. *AIChE Journal*, 43:1414–1425, 1997.

[115] R.T. Lahey Jr. Void wave propagation phenomena in two-phase flow (kern award lecture). *AIChE Journal*, 37(1):123–135, 1991.

[116] R.T. Lahey Jr. and D.A. Drew. The current state-of-the-art in the modeling of vapor/liquid two-phase flows. *ASME 90-WA/HT-13*, 1990.

[117] J.H. Lammers and A. Biesheuvel. Concentration waves and the instability of bubbly flows. *J. Fluid Mech.*, 328:64–94, 1996.

[118] A. Lapin and A. Lubbert. Numerical simulation of the dynamics of two-phase gas-liquid flows in bubble columns. *Chemical Engineering Science*, 49:3361, 1994.

[119] G. Le Coq, J.M. Ghidaglia, and A. Kumbaro. A new new numerical finite volume colocalized technique for the prediction of two-phase flow. In *The 3rd Int. Congress on Industrial and Applied Mathematics*, Hamburg, Germany, July 1995.

[120] E. León-Becerril and A. Liné. Stability analysis of a bubble column. *Chemical Engineering Science*, 56:6135–6141, 2001.

[121] T.-J. Lin, J. Reese, T. Hong, and L.-S. Fan. Quantitative analysis and computation of two-dimensional bubble columns. *AIChE Journal*, 42(2):301–318, 1996.

[122] H. Liu, Z. Zhang, and C. Qiu. Buoyancy-driven circulation in bubble columns. *AIChE Journal*, 44(11):2561–2564, 1998.

[123] Y. Maday, A.T. Patera, and E.M. Ronquist. An operator-integration-factor splitting method for time-dependent problems: application to incompressible fluid flow. *J. Sci. Comp.*, 5:263–292, 1990.

[124] M. Marchioro, M. Tanksley, and A. Prosperetti. Mixture pressure and stress in disperse two-phase flow. *Intl. J. Multiphase Flow*, 25:1395–1429, 1999.

[125] M. Marchioro, M. Tanksley, and A. Prosperetti. Flow of spatially non-uniform suspensions. part i: Phenomenology. *Intl. J. Multiphase Flow*, 26:783–831, 2000.

[126] M. Marchioro, M. Tanksley, W. Wang, and A. Prosperetti. Flow of spatially non-uniform suspensions. part ii: Systematic derivation of closure relations. *Intl. J. Multiphase Flow*, 27:237–276, 2001.

[127] T. Menzel, T. Weide, O. Staudacher, O. wein, and U. Onken. Reynolds shear stress modeling of bubble column reactors. *Industrial and Engineering Chemistry Research*, 29:988–994, 1990.

[128] P.D. Minev and C.R. Ethier. A characteristic/finite element algorithm for the 3-d navier-stokes equations using unstructered grids. *Comput. Methods Appl. Mech. Engrg.*, 178:39–50, 1999.

[129] P.D. Minev, U. Lange, and K. Nandakumar. A comparative study of two-phase flow models relevant to bubble column dynamics. *J.Fluid Mech*, 394:73–96, 1999b.

[130] S.J. Mosso, B.K Swartz, D.B. Kothe, and R.C. Ferrell. A parallel volume tracking algorithm for unstructered meshes. In P. Schiano, editor, *Parallel Computational Fluid Dynamics '96*. Italy, 1976.

[131] R.F. Mudde, D.J. Lee, J. Reese, and L.-S. Fan. Role of coherent structures on reynolds stresses in a 2-d bubble column. *AIChE Journal*, 43(4):913–926, 1997.

[132] R.F. Mudde and O. Simonin. Two and three dimensional simulation of a bubble plume using a two fluid model. *Chemical Engineering Science*, 54:5061–5069, 1999.

[133] R.I. Nigmatulin. Spacial averaging in the mechanics of heterogeneous and dispersed systems. *Intl J.Muliphase Flow*, 5:353–385, 1979.

[134] W.F. Noh and P. Woodward. Slic (simple line interphase calculations. *Lecture Notes in Physics*, 59:330–340, 1976.

[135] A. Nottenkamper, R. ans Stieff and P.M. Weinspach. Experimental investigation of hydrodynamics of bubble columns. *German Chemical Engineering*, 6:147–155, 1983.

[136] S. Osher and J.A. Sethian. Fronts propagating with curvature-dependent speed: Algorithms based on hamilton-jacobi formulations. *J. Comput. Phys.*, 79(1):12, 1988.

[137] Y. Pan, M.P. Dudukovic, and M. Chang. Numerical investigations of gas-driven flow in two-dimensional bubble columns. *AIChE Journal*, 46(3):434–439, 2000.

[138] J.-W. Park, D.A. Drew, and R.T. Lahey Jr. The analysis of void wave propagation in adiabatic monodispersed bubbly two-phase flows using an ensemble-averaged two-fluid model. *Intl. J. Multiphase Flow*, 24:1205–1244, 1998.

[139] C. Pauchon and S. Banerjee. Interphase momentum interaction effects in the averaged multifield model. part i: Void propagation in bubbly flows. *Int. J. Multiphase Flow*, 12(4):559–573, 1988.

[140] C. Pauchon and S. Banerjee. Interphase momentum interaction effects in the averaged multifield model. part ii: Kinematic waves and interfacial drag in bubbly flows. *Int. J. Multiphase Flow*, 14(3):253–264, 1988.

[141] D. Pfleger and S. Becker. Modelling and simulation of the dynamic flow behaviour in a bubble column. *Chemical Engineering Science*, 56:1737–1747, 2001.

[142] J.E. Pilliod Jr. and E.G. Puckett. Second-order volume-of-fluid algorithms for tracking material interphases. *J. Comput. Physics*, 1998.

[143] O. Pironneau. On the transport-diffusion algorithm and its application to the navier-stokes equations. *Num. Math.*, 38:309–332, 1982.

[144] A. Prosperetti and A.V. Jones. Pressure forces in disperse two-phase flow. *Intl J. Multiphase Flow*, 10(4):425–440, 1984.

[145] V.V. Ranade. Flow in bubble columns: Some numerical experiments. *Chemical Engineering Science*, 47(8):1857–1869, 1992.

[146] V.V. Ranade. Modelling of turbulent flow in a bubble column reactor. *Chemical Engineering research and Design*, 75:14–23, 1997.

[147] J. Reese, R.C. Chen, J.-W. Tzeng, and L.-S. Fan. Characterization of the macroscopic flow structure in gas-liquid and gas-liquid-solid fluidization systems using particle image velocimetry. *Int. Video J Engng Res.*, 3:17, 1993.

[148] J. Reese and L.-S. Fan. Transient flow structure in the entrance region of a bubble column using particle image velocimetry. *Chemical Engineering Science*, 49(24B):5623–5636, 1994.

[149] N. Reinecke and D. Mewes. Recent development and industtrial/research applications of capacitance tomography. *Measurements in Science and Technology*, 7:233–246, 1996.

[150] Rensen and Roig. Experimental study of the unsteady structure of a combined bubble plume. *International Journal of Multiphase Flow*, 27:1431–1449, 2001.

[151] R.G. Rice and N.W. Geary. Predictions of liquid circulation in viscous bubble columns. *AIChE Journal*, 36(9):1339–1348, 1990.

[152] G.R. Richter. An optimal-order error estimate for the discontinuous galerkin method. *Math. Comp.*, 50:75–88, 1988.

[153] G.R. Richter. The discontinuous galerkin method with diffusion. *Math. Comp.*, 58:631–643, 1992.

[154] W.J. Rider and D.B. Kothe. Reconstructing volume tracking. *Journal of Computational Physics*, 141:112–152, 1998.

[155] K. Rietema. Science and technology of dispersed two-phase systems-i and ii. *Chemical Engineering Science*, 37:1125–1150, 1982.

[156] K. Rietema and S.P.P. Ottengraf. Laminar liquid circulation and bubble street formation in a gas-liquid system. *Trans. Int. Chem. Eng.*, 48:54–62, 1970.

[157] J.E. Romate. Approximate riemann solvers for a hyperbolic two-phase flow model. In M. Feistauer, R. Rannacher, and K. Kozel, editors, *Numerical Modelling in Continuum Mechanics*, Proc. 3rd Summer Conference, Prague, 8-11 September 1997.

[158] P. Romstedt. A split-matrix method for the numerical solution of two-phase flow equations. *Nuclear Sci. Eng.*, 104:1–9, 1990.

[159] M. Rudman. Volume-tracking methods for interfacial flow calculations. *International Journal for Numerical Methods in Fluids*, 24:671–691, 1997.

[160] L. Sainsaulieu. Finite volume approximation of two-phase fluid flows based on an approximate roe-type riemann solver. *J. Comput. Phys.*, 121:1–28, 1995.

[161] J. Sanyal, S. Vasquez, S. Roy, and M.P. Dudukovic. Numerical simulation of gas-liquid dynamics in cylindrical bubble column reactors. *Chemical Engineering Science*, 54:5071–5083, 1999.

[162] Y. Sato and K. Sekoguchi. Liquid velocity distribution in a two-phase bubble case. *International Journal of Multiphase Flow*, 2:79, 1975.

[163] R. Saurel and R. Abgrall. A method for compressible multiphase flows with interfaces. In *Proc. ICMF'98, Third international conference on multi-phase flow*, Lion, Francd, 8-12 June 1998.

[164] M.P. Schwarz and W.J. Turner. Applicability of the standard $k-\epsilon$ turbulence model to gar stirred baths. *Applied Mathematical Modelling*, 12:273–279, 1988.

[165] Y.T. Shah, B.G. Kelkar, S.P. Godbole, and W.D. Deckwer. Design parameters estimation for bubble column reactors. *AIChE Journal*, 28:353, 1982.

[166] P.J. Shopov, P.D. Minev, and I.B. Bazhlekov. Numerical method for unsteady viscous hydrodynamical problem with free boundaries. *International Journal for Numerical Methods in Fluids*, 14:681–705, 1992.

[167] C. Shu and S. Osher. Efficient implementation of essentially non-oscillatory shock capturing schemes. *J. Comput. Phys.*, 77:439–471, 1988.

[168] O. Simonin and P.L. Viollet. On the computation of turbulent two-phase flows in eulerian formulation, turbulent two-phase system. In *Euromech 234*, Toulouse, France, 1988.

[169] A. Sokolichin and G. Eigenberger. Gas-liquid flow in bubble columns and loop reactors: Part-i. detailed modelling and numerical simualtion. *Chemical Engineering Science*, 49:5735–5746, 1994.

[170] A. Sokolichin and G. Eigenberger. Applicability of the standard turbulence model to the dynamic simulation of bubble columns: Part-i. detailed numerical simulations. *Chemical Engineering Science*, 54:2273–2284, 1999.

[171] A. Sokolichin, G. Eigenberger, A. Lapin, and A. Lübbert. Dynamic numerical simualtion of gas-liquid two-phase flows euler/euler versus euler/lagrange. *Chemical Engineering Science*, 52:611–626, 1997.

[172] H. Städtke, G. Franchello, and B. Worth. Numerical simulation of multi-dimensional two-phase flow based on flux vector splitting. *Nucl. Eng. Design*, 177:199–213, 1997.

[173] H. Städtke and R. Holtbecker. Hyperbolic model for inhomogeneous two-phase flow. In *Proc. Int. Conf. On Multiphase Flows*, University of Tsukuba, Japan, September 24-27 1991.

[174] H.B. Stewart and B. Wendroff. Two-Phase Flow:Models and Methods. *Journal of Computational Physics*, 56:369–409, 1984.

[175] Stuhmiller.J.H. The influence of interfacial pressure forces on the character of two-phase flow model equations. *Int.J.Multiphase Flow*, 3:551–560, 1977.

[176] E. Süli. Convergence and nonlinear stability of the lagrange-galerkin method for the navier-stokes equations. *Numer. Math.*, 53:459–483, 1988.

[177] M. Sussman, A. Almgren, J. Bell, P. Colella, L. Howell, and M. Welcome. An adaptive level set approach for incompressible two-phase flows. *J. Comput. Physics*, 148:81–124, 1999.

[178] M. Sussman and E.G. Puckett. A coupled level set and volume-of-fluid method for computing 3d and axisymmetric incompressible two-phase flows. *J. Comput. Physics*, 162:301–337, 2000.

[179] M. Sussman and P. Smereka. Axisymmetric free boundary problems. *J. Fluid Mech.*, 341:269, 1997.

[180] M. Sussman, P. Smereka, and S. Osher. A level set approach for computing solutions to incompressible two-phase flow. *J. Comput. Physics*, 114:146, 1994.

[181] H.F. Svendsen, H.A. Jakobsen, and R. Torvik. Local flow structures in internal loop and bubble column reactors. *Chemical Engineering Science*, 47:3297–3304, 1992.

[182] S.S. Thakre, D. Phanikumar, A.S. Khare, and J.B. Joshi. Cfd modeling of flow, macromixing and axial dispersion in a bubble column. *Canadian Journal of Chemical Engineering*, 77:826–837, 1999.

[183] I. Tiselj and S. Petelin. Modelling of two-phase flow with second-order accurate schemes. *J. Comput. Phys.*, 136:503–521, 1997.

[184] E.F. Toro. Riemann-problem based techniques for computing reactive two-phase flows. In A. Dervieux and B. Larrouturou, editors, *Numerical combustion*, volume 351 of *472*. Springer-Verlag, 1989.

[185] R. Torvik and H.F. Svendsen. Modelling of slurry reactors: a fundamental approach. *Chemical Engineering Science*, 45:2325–2332, 1990.

[186] I. Toumi. A weak formulation of roe's approximate riemann solver. *J. Comput. Phys.*, 102:360–373, 1992.

[187] I. Toumi. An upwind numerical method for two-fluid two-phase flow models. *Nuclear Sci. Eng.*, 123:147–168, 1996.

[188] J.-W. Tzeng, R.C. Chen, and L.-S. Fan. Visualization of flow characteristics in a 2-d bubble column and three-phase fluidized bed. *AIChE Journal*, 39(5):733–744, 1993.

[189] K. Ueyama and T. Miyauchi. Properties of recalculating turbulent two-phase flow in gas bubble columns. *AIChE Journal*, 25:258–265, 1979.

[190] S.O. Unverdi and G. Tryggvason. A front-tracking method for viscous, incompressible multifluid flow. *J. Comput. Physics*, 100:25–37, 1992.

[191] B. van Leer. On teh relation between the upwind-differencing schemes of gudunov, engquist-osher, and roe. *SIAM J. Sci. Comp.*, 5:1–20, 1984.

[192] L. van Wijngaarden. Hydrodynamic interaction between gas bubbles in liquid. *J. Fluid Mech.*, 77:27–44, 1976.

[193] E. Varoglu and W.D.L. Finn. Finite elements incorporating characteristics for one-dimensional diffusion-convection equation. *J. Comput. Phys.*, 34:371–389, 1980.

[194] G.B. Wallis. *One-dimensional Two-Phase Flow.* New York: McGraw-Hill, 1969.

[195] G.B. Wallis. The averaged bernoulli equation and macroscopic equations of motion for the potential motion of a two-phase dispersion. *Intl. J. Multiphase Flow*, 17:683–695, 1991.

[196] J.F. Walter and H.W. Blanch. Liquid circulation patterns and their effect on gas hold-up and axial mixing in bubble columns. *Chemical Engineering Communication*, 19:243, 1983.

[197] H. Wang, H.K. Dahle, M.S. Espedal, R.E. Ewing, R.C. Sharpley, and S. Man. An ellam scheme for advection-diffusion equation in two-dimensions. *SIAM J. Sci. Comput.*, 20:2160–2194, 1999.

[198] H. Wang, D. Liang, R.E. Ewing, S.L. Lyons, and G. Qin. An approximation to miscible fluid flows in porous media with point sources and sinks by an eulerian-lagrangian localized adjoint method and mixed finite element methods. *SIAM Journal on Scientific Computing*, 22(2):561–581, 1999.

[199] S.K. Wang, S.J. Lee, O.C. Jones Jr., and R.T. Laher Jr. 3-d turbulence structure and phase distribution measurements in bubbly two-phase flows. *Intl. J. Multiphase Flow*, 13:327–343, 1987.

[200] W. Wang and A. Prosperetti. Flow of spatially non-uniform suspensions. part iii: Closure relations for porous media and spinning particles. *Intl. J. Multiphase Flow*, 27:1627–1653, 2001.

[201] W. Warsito and L.-S. Fan. Measurement of real-time structures in gas-liquid and gas-liquid-solid flow systems using electrical capacitance tomography (ect). *Chemical Engineering Science*, 56:6455–6462, 2001.

[202] C.G. Xie, S.M. Huang, B.S. Hoyle, R. Thorn, C. Lean, D. Snowden, and M.S. Beck. Electrical capacitance tomography for flow imaging system model development of image

reconstruction algorithms and design of primary sensor. *IEE Proceedings G*, 139:89–98, 1992.

[203] Y.B. Yang, N. Devanathan, and M.P. Dudukovic. Liquid backmixing in bubble columns via computer-automated radioactive particle tracking (carpt). *Exp. Fluids*, 16:1–9, 1993.

[204] B.P. Yao, C. Zheng, H.E. Gasche, and H. Hofmann. Bubble behaviour and flow structure of bubble columns. *Chemical Engineering Processes*, 29:65–75, 1991.

[205] D.L. Youngs. Time-dependant multi-material flow with large fluid distortion. In K.W. Morton and M.J. Baines, editors, *Numerical Methods for Fluid Dynamics*, page 273. New York: Academic Press, 1982.

[206] Y.H. Yu and S.D. Kim. Bubble properties and local liquid velocity in the radial direction of co-current gas-liquid flow. *Chemical Engineering Science*, 46:313–320, 1991.

[207] P. Zehner. Bubble columns. *Ulmann's encyclopedia of industrial chemistry*, 2000.

[208] D.Z. Zhang and A. Prosperetti. Averaged equations for inviscid disperse two-phase flow. *J.Fluid Mech.*, 267:185–219, 1994.

[209] D.Z. Zhang and A. Prosperetti. Momentum and energy equations for disperse two-phase flows and their closure for dilute suspensions. *Int. J. Multiphase Flow*, 23:425–453, 1997.

[210] Q. Zhou and M. A. Leschziner. An improved particle-locating algorithm for eulerian-lagrangian computations of two-phase flows in general coordinates. *International Journal of Multiphase Flow*, 25:813–825, 1999.